Dynamics and Regulation of Microtubule Minus Ends

By

Claire Elizabeth Strothman

Dissertation

Submitted by the Faculty of

the Graduate School of Vanderbilt University

in partial fulfillment of the requirements

for the degree of

DOCTOR OF PHILOSOPHY

in

Cell and Developmental Biology

June 30, 2021

Nashville TN

Approved:

Matthew J. Tyska, Ph.D., Chair

Lauren P. Jackson, Ph.D.

David M. Miller III, Ph.D.

Matthew J. Lang, Ph.D.

Marija Zanic, Ph.D.

Acknowledgements

The work herein described would not have been possible without the support, feedback, and encouragement from my mentors, family, and friends. To the following I offer my sincere thanks.

First, I would like to thank my mentor Dr. Marija Zanic for supporting me throughout my graduate experience and for teaching me to become a much better scientist. I am grateful for having an environment where I was encouraged and inspired to succeed, especially as a woman in science. Thank you to the members of the Ohi lab with whom we shared many lab meetings, scientific collaborations, and celebrations: Dr. Ryoma Ohi, Dr. Stephen Norris, Dr. Jennifer Landino, and Dr. Megan Dumas. Thank you to my committee members, Dr. Matthew Tyska, Dr. Matthew Lang, Dr. Lauren Jackson, and Dr. David Miller for many helpful insights and advice. I acknowledge our collaborators, Dr. David Miller and Sierra Palumbos, for their crucial feedback and discussions related to the VAB-8 project. I also extend many thanks to the other graduate students, especially in Cell and Developmental Biology, who have helped and supported me on so many occasions. Thank you to the Microtubules and Motors club, organized by Dr. Irina Kaverina, for many thoughtful discussions.

I would like to thank my first research lab where I developed a passion for scientific research as an undergraduate. Thank you in particular to my mentors Dr. Qi Zhang, Dr. Claire Delbove, and Dr. Kristina Kitko for their guidance and patience.

Thank you to my lab members, past and present, who have helped shape my research, trained me to become a better scientist, celebrated the wins, and supported me in difficult times. Thank you to my fellow Zanic lab graduate students for always bringing levity and humor to our everyday lab environment.

Thank you to the Cell and Developmental Biology Department, in particular the administrative staff, whose support has been invaluable. I am so grateful to have joined the CDB department, which has such a welcoming and collaborative environment. The BRET office has also been a great resource during my time- thank you especially to Carolyn Berry and Dr. Beth Bowman.

I acknowledge the support I received from the Cellular, Biochemical, and Molecular sciences Training grant. Thank you to the Nikon Center of Excellence for access to cutting edge microscopes and resources.

Lastly, I would like to thank my family, especially my parents, for doing everything they could to ensure my success and support me, no matter what. This journey would not have been possible without their constant encouragement. Thank you to my closest friends for their support throughout all the highs and lows, for always being available for happy hours (even long-distance), and for always encouraging me to live my best life. Finally, I would like to thank my dog, Sheila, for being my steadfast, loyal companion on this journey. While my family and friends have been far away, Sheila has been an ever-present source of support, especially during the immense difficulty of the COVID-19 pandemic.

Table of Contents

Appendix

List of Figures

Figure **Page**

List of Abbreviations

MT	microtubule
MTOC	microtubule organizing center
MTBD	microtubule-binding domain
γ-TuRC	γ-tubulin ring complex
GTP	guanosine triphosphate
GDP	guanosine diphosphate
ATP	adenosine triphosphate
GMPCPP	guanosine-5'-[(α,β)-methyleno]triphosphate
AMPPNP	adenylyl imidodiphosphate
GFP-	green fluorescent protein
PTM	post-translational modification
MAP	microtubule-associated protein
MCAK	mitotic centromere-associated kinesin
HSET	human spleen, embryonic tissue, and testes protein
NLS	nuclear localization sequence
TIRF	total internal reflection fluorescence
TMR	tetra-methyl rhodamine
CDF	cumulative distribution function
SD	standard deviation
SEM	standard error of the mean

Chapter 1

Introduction

1.1 Introduction

Microtubules are part of the cytoskeletal system in cells, as they are one of several different networks of polymers that perform essential cellular roles. They perform an astonishing array of critical functions in many eukaryotic organisms, ranging from unicellular algae (*C. reinhardtii*) to humans (*H. sapiens*), and countless species in between. Cells that contain microtubules cannot survive without them, as they serve as the intracellular highways directing transport within the cell, the rigid scaffolding defining the very architecture of the cell, and the machinery that drives the division of cells, and therefore the propagation of life itself. To carry out these crucial, yet diverse, set of functions, microtubules display certain fascinating and unique properties that still remain not fully understood.

1.2 Cellular microtubule organization

1.2.1 Microtubule structure

Microtubules are self-assembling polymers of α/β tubulin protein heterodimers that organize into hollow filamentous tubes, consisting typically of thirteen individual protofilament strands, offset in a three-start helix (Figure 1.1) (Borisy and Taylor, 1967a; b; Weisenberg et al., 1968; Mandelkow et al., 1986; Nogales et al., 1999). This creates an overall asymmetry within the structure and the formation of a seam at which the lateral tubulin interfaces differ from that of the rest of the polymer. The tubulin dimers within each protofilament strand bind head-to-tail, such that the microtubule itself is structurally polar (Fan et al., 1996; Nogales et al., 1999). The

α-tubulin side of the dimer is exposed at the microtubule minus end, and the β-side is exposed at the plus end of the microtubule (Figure 1.1) (Fan et al., 1996; Nogales et al., 1999). This biochemical and structural polarity is the fundamental difference between the two microtubule ends. Microtubules stochastically assemble and dissemble at the ends in a process called dynamic instability (Mitchison and Kirschner, 1984; Walker, 1988). This dynamic behavior allows for microtubules to continuously build and rebuild the microtubule network in the cell, to maintain the cellular structure and intracellular tracks. Microtubule dynamics can be regulated in the cell to dramatically change the microtubule architecture, such as during the processes of cell differentiation and cell division.

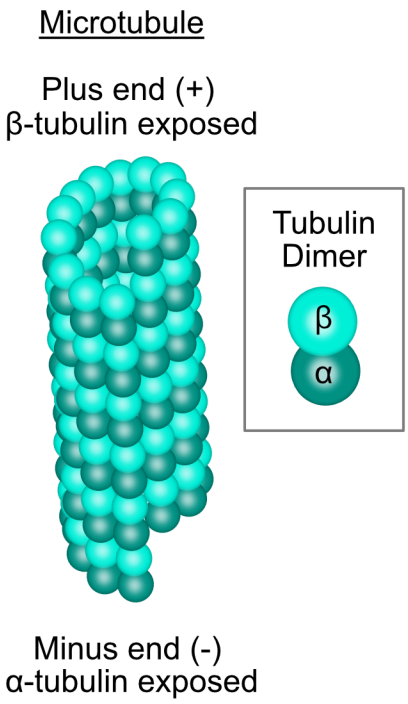

Figure 1.1. Schematic of a microtubule structure. The orientation of the α/β tubulin heterodimer is indicated within the microtubule, giving rise to α-tubulin being exposed at the

minus end, and the β-tubulin being exposed at the plus end. There is a 3-start pitch and 13 protofilaments comprising the hollow polymer structure.

1.2.2 Centrosomal microtubule arrays

Microtubule arrays in cells encompass a variety of different organizations, often dependent on the cell type. Many cells, like mesenchymal cell types, contain centrosomal microtubule arrays in which microtubules emanate radially from the center of the cell to cortex. In a centrosomal microtubule array, many minus ends are anchored at the centrosome through the gamma-tubulin ring complex (γ-TuRC), as well as additional regulatory factors (Petry and Vale, 2015; Martin and Akhmanova, 2018). The γ-TuRC is one of the primary mechanisms for microtubule nucleation in cells, as it serves as a template for α/β tubulin dimers to bind to and initiate the process of self-assembly (Moritz et al., 1995, 2000; Kollman et al., 2010, 2011). It lowers the activation energy for de novo nucleation of microtubules, which is energetically unfavorable (Thawani et al., 2020). In this process, the plus end grows outward from the site of nucleation and is free to grow and shrink while the minus end is the anchored point binding to the γ-TuRC nucleation site, and is reasonably thought to be excluded from dynamics (Wiese and Zheng, 2000). Overall, in these types of microtubule arrays, (i) minus ends are thought to be mostly anchored to organelles and non-dynamic, (ii) any subpopulation of free minus ends is likely obscured by the high microtubule density towards the cell center, and (iii) the plus ends, in contrast, can be clearly visualized towards the flatter periphery of the cell and exhibit robust dynamics (Akhmanova and Hoogenraad, 2015). These observations establish some fundamental reasoning to explain why research on minus ends is severely lacking in comparison to microtubule plus-end focused research.

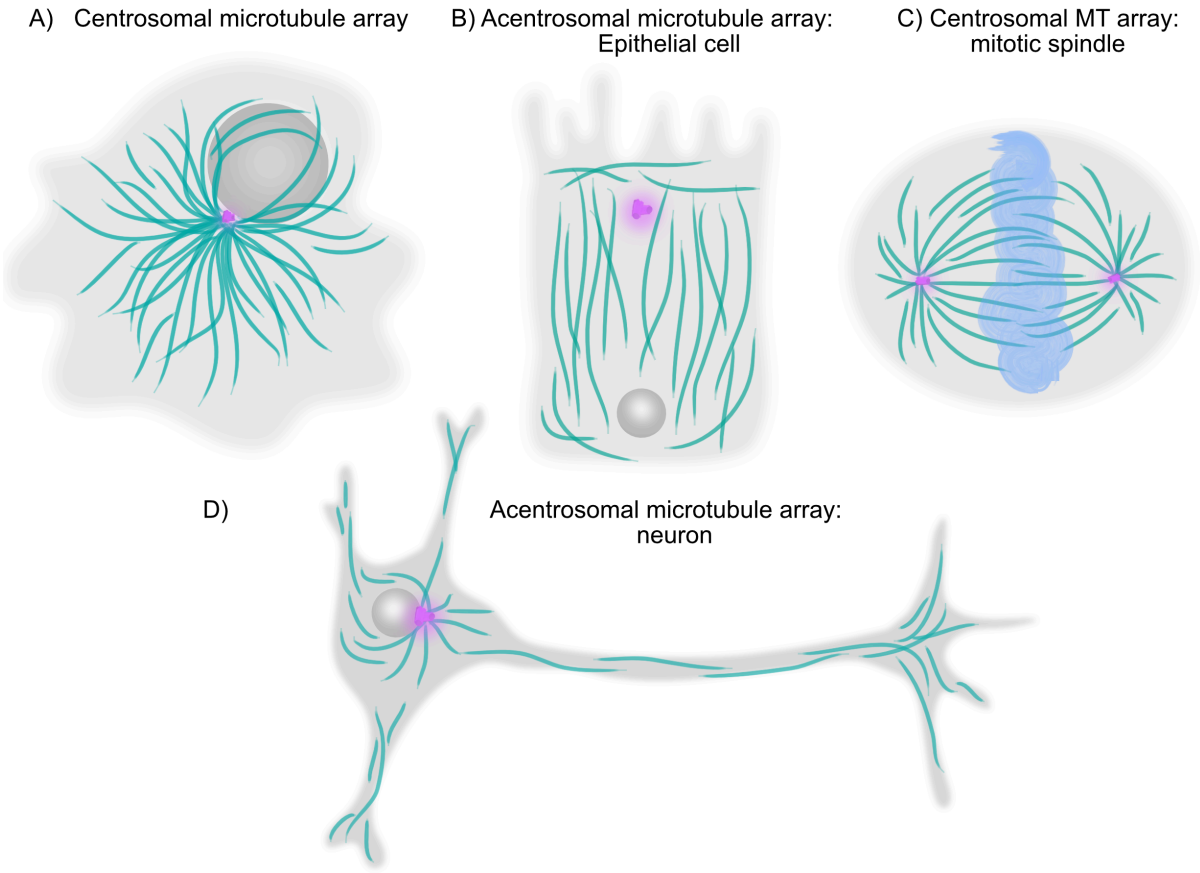

Figure 1.2. Examples of different microtubule arrays in different cell types. A) A radial centrosomal array of microtubules, where minus ends are oriented towards the centrosome. B) An epithelial cell with an acentrosomal microtubule array in which many microtubules are parallel such that minus ends are oriented towards the apical surface of the cell. C) A mitotic cell in which the mitotic spindle is built from microtubules radiating from two centrosomal arrays. Minus ends are oriented towards the two spindle poles, but there are also minus ends distributed throughout the spindle midzone. D) A neuron in which there are centrosomal microtubules, but the majority of the microtubule organization along the axon and dendrites is non-centrosomal, consisting of parallel and anti-parallel arrays of microtubules, respectively.

1.2.3 Acentrosomal microtubule arrays

While centrosomes may be the primary microtubule organizing center (MTOC) in many cell types, there are other important sites of microtubule nucleation and assembly, such as that at

the Golgi apparatus (Efimov et al., 2007; Zhu and Kaverina, 2013; Rios, 2014; Martin and Akhmanova, 2018). This non-centrosomal microtubule array, in which microtubules emanate from γ-TURCs at the Golgi, is shaped differently and positioned differently than the centrosome, such that this may give the cell more asymmetry in the overall microtubule network (Meiring et al., 2020). Mesenchymal cells with both centrosomal and acentrosomal microtubule arrays may benefit from the asymmetry of the overall network to have increased polarity of the cell and a denser microtubule network, both of which may be useful for cell migration (Meiring et al., 2020). Further, differentiating cell types may completely disassemble the centrosomal microtubule array in favor of non-centrosomal arrays, which may or may not include clear organization from other MTOCs. One practical advantage of this transition from a centrosomal to a non-centrosomal array is decreasing the likelihood of microtubule disarray if there were an increase in centrosome number, which is a common feature in cancerous cells (Meiring et al., 2020).

Epithelial cells and neurons represent two examples of cell types with distinct acentrosomal microtubule arrays that may also be highly polarized (Figure 1.2). Epithelial cells have parallel apico-basal microtubules, in which minus ends are pointed towards the apical surface, and plus ends towards the basal side. Neurons contain bundles of parallel plus-end-out microtubules along the axon and antiparallel microtubules of mixed polarity throughout dendrites, in which active microtubule minus-end growth has been observed (Kapitein and Hoogenraad, 2015; Feng et al., 2019). In mitosis, the dense network of microtubules comprising the spindle consists of both centrosomal and acentrosomal microtubules, with many free minus ends distributed along the length of the spindle (Figure 1.2) (O'Toole et al., 2003; Redemann et al., 2017). In cells with centrosomal microtubule arrays, free minus ends that are generated tend

to depolymerize; however in cells with non-centrosomal microtubule arrays, free minus ends tend to be more stable (Dammermann et al., 2003).

During the re-organization of a microtubule architecture in such cellular processes as mitosis or differentiation, free minus ends can be generated in a number of ways (Dammermann et al., 2003). First, a microtubule can simply undergo mechanical breakage from some type of exerted force (Odde et al., 1999; Waterman-Storer and Salmon, 1997). Additionally, the microtubule could be severed by members of a class of microtubule-associated severing proteins, which is one mechanism by which microtubules are released from microtubule-organizing centers, such as the centrosome (Keating et al., 1997; Ahmad et al., 2000; Nakamura et al., 2010). Lastly, cytoplasmic assembly could occur (Vorobjev et al., 1997; Yvon and Wadsworth, 1997); however, this process is likely due to templated nucleation through γ-TURCs, so these minus ends are not anchored to an organelle, but they are presumably capped (Dammermann et al., 2003; Akhmanova and Steinmetz, 2015).

Though the dynamics of plus ends in the cell are more robust and easily observed, the dynamics of minus ends in cells have important roles in maintaining or re-organizing the microtubule architecture. Depolymerization of free minus ends can significantly contribute to microtubule turnover (Vorobjev et al., 1999; Rodionov et al., 1999). In mitosis, a phenomenon called poleward flux has been observed whereby net microtubule assembly occurs at the plus ends, and net disassembly occurs at the minus ends near the poles (Rogers et al., 2005; Kwok and Kapoor, 2007). While this process is still not entirely well understood, it does appear that the net dynamics of both microtubule ends must be coordinated in order to achieve this overall microtubule turnover effect. Finally, recent studies are discovering that minus-end growth in cells is a mechanism by which microtubules can be organized in microtubule arrays (Feng et al.,

2019). Due to many challenges and limitations, there have not been nearly as many studies into the role of microtubule minus-end dynamics in cells compared to those focusing on plus ends, but it is clear from what we do know that minus-end dynamics and regulation do occur in cells and play important roles in the regulation of microtubule networks (Akhmanova and Hoogenraad, 2015).

1.3 Microtubule dynamic instability

1.3.1 Defining microtubule dynamic instability

Microtubules undergo dynamic instability in cells, and this process is thought to be regulated by a number of factors, including many microtubule-associated proteins. Although naturally, many factors are involved in cellular microtubule dynamics, it can be reconstituted *in vitro* with tubulin alone. This allows for the study of the fundamental properties of microtubule dynamic instability, as well the individual effects of factors that may modulate the process.

Dynamic instability is the unique behavior of microtubules in which they undergo phases of growth and shrinkage at the ends, and stochastically transition back and forth between these two states. The transition from growth to shrinkage is called 'catastrophe' and the converse transition is called 'rescue.' The term 'dynamic instability' was coined by Mitchison and Kirshner in a 1984 milestone study that reconstituted and characterized microtubule dynamics *in vitro* with purified tubulin, and defined the parameters of growth, shrinkage, catastrophe and rescue. Other work following this landmark study examined more closely individual behavior of microtubules in an *in vitro* reconstitution system using purified tubulin, and found that both microtubule plus and minus ends exhibited dynamic instability, and that each end had distinct dynamic properties (Horio and Hotani, 1986; Walker et al., 1988). Specifically, plus ends tend to

grow faster than minus ends in a given condition, and also undergo catastrophe more frequently, giving plus ends an overall greater "dynamicity" than minus ends.

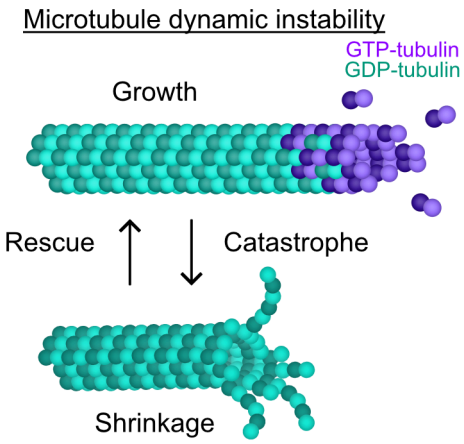

Figure 1.3. Schematic of microtubule dynamic instability. Dynamic instability is defined by phases of growth and shrinkage, which occur through transitions of catastrophe and rescue. GTP-tubulin adds to the growing microtubule ends, before hydrolyzing into GDP-tubulin. The region of GTP-tubulin at the growing microtubule end is called the GTP-cap.

1.3.2 GTP hydrolysis and the GTP-cap

One feature of microtubule dynamics that is thought to power the process itself, is that of GTP-hydrolysis (Figure 1.3). Tubulin dimers are GTPases, meaning that they hold the ability to hydrolyze GTP (guanosine triphosphate), as a source of energy to power the dynamic self-assembly process to form microtubules. Both α- and β- tubulin contain a GTP-binding site; however, the GTP-binding site of the α-tubulin is buried within the interface of the tubulin dimers, and is non-exchangeable (the N-site), while the GTP-binding site at the β-tubulin dimer is active and exchangeable (the E-site) (Nogales et al., 1998). During microtubule growth, GTP-

tubulin incorporates into the microtubule end, and after a brief lag, the GTP hydrolyzes to GDP (Nogales et al., 1999). The GTP-tubulin at the very end of the growing microtubule is thought to be in an energetically favorable conformation, and therefore forms a stabilizing GTP- cap that favors continues microtubule growth (Alushin et al., 2014). The process of GTP to GDP hydrolysis in the tubulin dimer induces a conformational change of the tubulin such that it is no longer in an energetically favorable conformation (Alushin et al., 2014; Zhang et al., 2018). If the GTP-cap is lost at the end of the growing microtubule, this is thought to induce catastrophe, since the strained GDP-tubulin favors being released from the microtubule polymer during microtubule shrinkage (Carlier and Pantaloni, 1981; Nogales et al., 1998; Zhang et al., 2015; Duellberg et al., 2016a). If the GTP-tubulin did not hydrolyze, the microtubule lattice would be stable, and continue growth as long as there were available tubulin subunits. Indeed, it was shown that microtubules grown with GMPCPP, a non-hydrolysable GTP-analog, do not undergo dynamic instability (Hyman et al., 1992). Further evidence for the GTP-cap comes from observations that severing the microtubule lattice and creating two new microtubule ends results in rapid depolymerization of the newly formed plus end (Walker et al., 1989; Tran et al., 1997). Tubulin dilution experiments in which dynamic microtubules were first grown in different tubulin concentrations, and soluble tubulin was subsequently rapidly removed from solution through buffer exchange, showed that microtubules underwent catastrophe within several seconds of the dilution (Walker et al., 1991; Voter et al., 1991). This suggested that the removal of a small stabilizing GTP-cap at the growing end results in a brief lag between the tubulin removal and catastrophe. This fine balance of stability of the tubulin within the microtubule lattice based on the nucleotide state powers dynamic instability. Interestingly, this process has been studied more extensively at the plus end than at the minus end, so the degree to which

certain principles developed from observations of the plus end apply to the minus end is not known.

1.4 Microtubule regulation in cells

The organization, reorganization, and maintenance of the many diverse microtubule architectures are highly regulated by other cellular factors. At the tubulin level, the microtubule network can be auto-regulated by the levels of soluble tubulin in the cell (Ohi et al., 2021). Microtubule depolymerizing agents applied to cells increase the amounts of soluble tubulin, and it has been observed that tubulin mRNAs are degraded, and tubulin protein synthesis decreases (Cleveland et al., 1981; Ben-Ze'ev et al., 1979). Treatment with the microtubule stabilizing drug Taxol, on the other hand, elicits the opposite response, where tubulin mRNA levels and protein synthesis are increased (Cleveland et al., 1981; Cleveland, 1989). This suggests that the cell is capable of sensing the balance between microtubule polymer and soluble tubulin within the cell, and adjusts the output of newly synthesized tubulin as a result (Ohi et al., 2021).

Another system of regulation of microtubules is that of post-translational modifications (PTMs) (Song and Brady, 2015; Magiera and Janke, 2014). As microtubules exist longer in the cell, they are subject to accumulate more PTMs over time, including acetylation, polyglutamylation, phosphorylation, and others (Kapitein and Hoogenraad, 2015). It is thought that these PTMs may serve several different functions, including stabilizing the microtubule itself, as well as altering the binding affinity for certain microtubule-associated proteins (Song and Brady, 2015; Magiera and Janke, 2014; Kapitein and Hoogenraad, 2015).

Finally, microtubule associated proteins (MAPs) are a major subtype of regulator of microtubule dynamics and organization. MAPs are incredibly functionally diverse: they may act

as spatial regulators of microtubules, directly impact microtubule dynamics at the tips by stabilizing or destabilizing them, anchor microtubules to organelles or the cell membrane, sever microtubules to change the microtubule organization and potentially amplify the network, and even build dynamic microtubule structures such as the mitotic spindle. Within the cell, the microtubule network and its regulation by other cellular factors is an incredibly complex system that we still do not fully understand as a whole, especially across diverse cell types.

1.5 Microtubule-associated proteins

1.5.1 Categories of MAPs

Microtubule-associated proteins (MAPs) represent one major regulatory factor for microtubules, in terms of both cellular organization as well as regulation of dynamics. MAPs may be classified into several sub-categories: (i) motile MAPs (ii) enzymatic destabilizers (iii) nucleation factors (iv) end-binding proteins and (v) structural MAPs (Bodakuntla et al., 2019). Motile MAPs include microtubule motor proteins kinesin and dynein, which can execute a vast array of functions in the cell. The remaining categories include the proteins that are more synonymous with the idea of MAPs and their roles in regulation of key microtubule processes, often at the level of the individual microtubule. Severing enzymes such as katanin, spastin, and fidegetin comprise a class of enzymatic destabilizers that remove tubulin dimers along the lattice that eventually form breaks in the microtubule (McNally and Vale, 1993; Hazan et al., 1999; Mukherjee et al., 2012). These are known to play important roles in regulating the microtubule network in processes such as neuronal development and cell division (Hazan et al., 1999; Ahmad et al., 2000; Zhang et al., 2007; Mukherjee et al., 2012; Tao et al., 2016; Jiang et al., 2017). Nucleation factors such as γ-TuRC and TPX2 help control the spatial organization of

microtubules by controlling where the microtubules originate in the cell (Alfaro-Aco et al., 2017; King and Petry, 2020). There are dozens of proteins that be classified as end-binding proteins, and they may recognize either one end specifically, or both ends. One of the most widely-known end binding proteins is EB1, which recognizes both microtubule ends during growth, and recognizes the nucleotide state of the tip (Bieling et al., 2007; Zanic et al., 2009; Zhang et al., 2015, 2018). Another example is XMAP215, which localizes to microtubule plus ends, where it increases the rate of polymerization (Brouhard et al., 2008; Zanic et al., 2013). Generally, many MAPs that affect microtubule dynamics target microtubule ends. Structural MAPs represent a broader category which encompasses MAPs that bind to the microtubule lattice and often stabilize it, such as tau, but also can exert other functions such as affecting the way in which other factors interact with the microtubule, such as other proteins or components within the cell (Bodakuntla et al., 2019; Siahaan et al., 2019; Best et al., 2019; Tan et al., 2019; Monroy et al., 2020). Of course, MAPs can be classified in other schemes, and may fit the criteria of multiple categories. Overall, MAPs represent a large group of proteins that interact with and affect microtubules in exceedingly diverse ways, and we are still discovering novel functions and roles of many MAPs.

1.5.2 Kinesins

Microtubule-associated proteins span a range of functions from regulating microtubule dynamics, affecting microtubule organization, and utilizing microtubules for transport. Although some microtubule-associated proteins may only fit into one of these categories, kinesin motor proteins represent a class of proteins in which there are members that collectively accomplish all of these functions. The canonical role of kinesins is to transport cellular components, such as

vesicles, organelles, and mRNA within the cell, and this is indeed a major function of some kinesins, such as kinesin-1, kinesin-2, and kinesin-3 (Hirokawa et al., 2010). Within the mitotic spindle, other kinesins play a key role in crosslinking multiple microtubules together to organize the microtubules in the spindle and generate force, such as kinesin-5 (also known as Eg5) (Wordeman, 2010; Mann and Wadsworth, 2019). Finally, other kinesins have been recognized to affect microtubule dynamics, such as kinesin-13s (MCAK), which act as depolymerases by removing tubulin subunits from the microtubule ends (Wordeman and Mitchison, 1995; Walczak et al., 1996; Desai et al., 1999; Moores et al., 2002; Hunter et al., 2003; Helenius et al., 2006). One subcategory of kinesins is the kinesin-14 family, which are microtubule minus-end directed motors (Hirokawa et al., 2010; Wordeman, 2010). This work utilizes unique properties of human kinesin-14 HSET to understand the mechanisms of dynamics of the minus end, as well as delves further into characterizing it as a novel regulator of microtubule minus-end dynamics and the mechanisms by which it accomplishes this role.

1.5.3 Minus-end directed Kinesin-14 HSET

One of the most compelling rationales for studying the minus-end directed kinesin HSET/KIFC1 (**H**uman **S**pleen, **E**mbryonic Tissue, and **T**estes protein) resides in its role in focusing poles, especially in certain contexts, such as cancer. In cells with supernumerary centrosomes (a common feature of cancer cells), HSET has been shown to be a necessary factor in focusing the multipolar spindle into a pseudo-bipolar one capable of completing mitosis (Kwon et al., 2008). HSET has also been identified as a factor that is overexpressed in certain types of cancer, which can be used as a diagnostic marker of poor prognosis (Liu et al., 2016; Kostecka et al., 2021). HSET enables cell division in otherwise incapable cells, thereby fueling

tumor growth (Kwon et al., 2008; Wu et al., 2013; Pannu et al., 2015; Xiao and Yang, 2016; Fu et al., 2018; She and Yang, 2017; Li et al., 2020; Zhou et al., 2020). Since it is also thought to be a non-essential motor in non-cancerous cells, HSET has become a promising potential chemotherapeutic target and several small molecule inhibitors have been developed for this purpose (Xiao and Yang, 2016; Yukawa et al., 2018; Parvin et al., 2020; Myers and Collins, 2016; Sekino et al., 2019).

In cells, overexpression of HSET results in elongated and tapered mitotic spindles, whereas HSET knockdown produces shortened spindles (Cai et al., 2009; Norris et al., 2018). HSET has been shown to crosslink and slide microtubules within the spindle, and counteract against the outward force of the plus-end directed kinesin-5 motor, Eg5 (Mountain et al., 1999). Acentrosomal spindles without HSET fail to assemble; however, simultaneous depletion of HSET and Eg5 restores spindle organization, suggesting that these two oppositely-directed motors engage in balancing the forces within the spindle (Mountain et al., 1999). Characterization of HSET and Eg5 *in vitro* have shown that HSET can acts as a brake against Eg5's plus-end directed antiparallel sliding of microtubules (Reinemann et al., 2018). In this *in vitro* bundle assay, Eg5 dictates the sliding direction, but HSET dictates the force magnitude and velocity in the sliding, and a high amount of Eg5 is needed to overcome the force regulation of HSET (Reinemann et al., 2018).

The kinesin-14 family of motors are grouped by the shared feature of having an inverse kinesin body plan, such that the motor domain is located at the C-terminus, rather than the N-terminus, as is the case for conventional plus-end directed kinesins. Interestingly, it is the neck linker of these motors that dictates the minus-end directionality (Sablin et al., 1998; Endow and Higuchi, 2000; Henningsen and Schliwa, 1997). HSET is a 74 kDa protein containing two

microtubule-binding domains: one in the N-terminal tail region, and one in the C-terminal motor domain, connected by a central coiled-coil stalk region (Figure 1.4) (Norris et al., 2018). While the microtubule binding domain in the motor domain of HSET is largely conserved among most kinesins, the microtubule-binding domain-containing tail region of HSET has some interesting features. Sequence analysis of this region does not indicate any conserved tubulin binding motif, but rather an electrostatically charged positive region. This positively-charged region is thought to both attract the net negative charge of tubulin, either in soluble or polymer form, as well as function as a nuclear localization sequence (NLS) (Weaver et al., 2015). The tail region of HSET also contains a putative SxIP-like motif, which binds the C-terminal region of the microtubule-associated protein EB1 (Braun et al., 2013). This work characterizes the ways in which HSET regulates microtubules, and the mechanisms by which it does so, but there are many interesting questions that remain in regard to this unique kinesin family member.

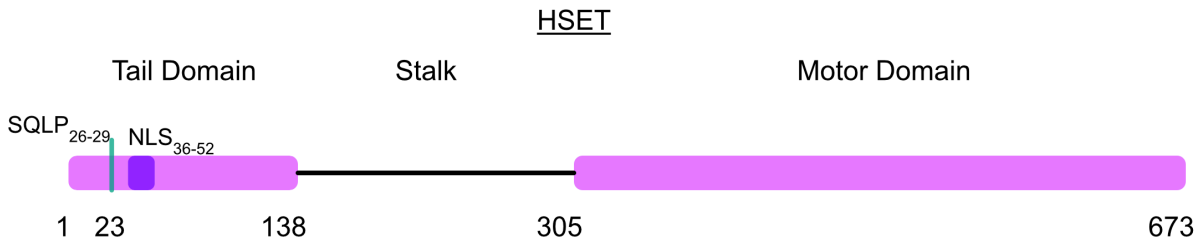

Figure 1.4. Schematic of HSET. HSET contains a C-terminal motor domain enabling its minus-end directed motility, a central coiled-coil stalk for homo-dimerization, and an N-terminal Tail domain containing a nuclear localization sequence (NLS), a SXiP-like motif for binding to EB1, and a tubulin-binding domain (not shown in schematic).

1.6 Summary

While the majority of research exploring the mechanisms of microtubule dynamics has focused on plus ends, there is increasing evidence to support the need to better understand the "dark side" of the microtubule, the minus end (Desai and Mitchison, 1997). Although it consists of the same tubulin as the plus end, it is mechanistically very different, and further exploration of those differences may lead to breakthroughs in our understanding of the basic underpinnings of microtubule dynamics. The rationale of microtubule minus ends not exhibiting dynamics in cells is an oversimplification, and one that is increasingly being challenged by recent findings of minus-end dynamics in cells. Additionally, proteins that specifically regulate minus ends are only being discovered and characterized relatively recently. This work defines key mechanistic differences between plus- and minus-end dynamics, as well as further characterizes the minus-end directed kinesin-14 HSET.

Chapter 2

In vitro reconstitution of microtubule dynamics

2.1 Introduction

Biochemical reconstitution of cytoskeletal components has historically been an invaluable part of the scientific progression of the field. Many breakthroughs and mechanistic insights have been achieved using this method for many decades to better understand the properties of the cytoskeleton and how it is regulated. Before the term 'microtubule' even existed, investigators were interested in understanding the process of cell division. In a landmark study, polarized light microscopy was used to observe birefringent spindle fibers in the diving cell (Inoué and Sato, 1967). These spindle fibers were observed to polymerize and depolymerize during mitosis, and this equilibrium could be shifted with different treatments, such as colchicine, a microtubule-destabilizing agent (Inoué and Sato, 1967). Tubulin protein was then identified as the protein building block, and first isolated using colchicine (Borisy and Taylor, 1967a; b). Not long after, the conditions for efficient microtubule self-assembly *in vitro* were identified by Weisenberg et al. (1968) who reported the necessity of GTP, Mg^{2+} ions, and a calcium chelator such as EGTA in order to achieve microtubule polymerization *in vitro* (Weisenberg et al., 1968). It was hypothesized at this point that microtubules polymerized in an actin-like treadmilling fashion, where one end polymerized, the other end depolymerized, and the net length stayed relatively constant. A huge milestone was reached in the field when Mitchison and Kirschner combined biochemical reconstitution with microscopy to discover the property of microtubule dynamic instability, in which microtubules were both growing and shrinking (Mitchison and Kirschner, 1984). Further studies directly observed and quantified

dynamic instability using time lapse imaging (Horio and Hotani, 1986; Walker, 1988). Since then, *in vitro* reconstitution has played an essential role in elucidating the mechanistic properties of microtubules themselves, as well as how they are regulated by microtubule-associated proteins. To date, *in vitro* reconstitution of microtubules and MAPs remains a critical approach to understanding biological processes, and only increases in sophistication with the development of new technology and techniques.

In this *in vitro* system, we use purified proteins to reconstitute microtubules as well as their associated regulatory proteins. This approach has many advantages in answering certain fundamental questions about microtubule dynamics and their regulation at the individual microtubule level, compared to other methods using cells, cellular extracts, or even whole organisms. In this work, we are interested in addressing fundamental mechanistic questions about microtubule dynamics that cannot easily be answered in cells- there are countless regulatory components that are always affecting microtubules, and it is difficult, if not impossible, to disentangle the fundamental nature of microtubule dynamics from the roles that other regulatory proteins or conditions in the cells have on them. For example, estimating precise kinetic rates of tubulin association and disassociation of a dynamic microtubule end is not something that can confidently be measured in cells, given such a wide range of cellular conditions for microtubules. Further, when we measure the impact of regulatory proteins on microtubule dynamics, we can more confidently make conclusions about the autonomous effects of a given protein. The *in vitro* system allows us to more easily and confidently claim mechanistic insight into the fundamental behavior and regulation of microtubules. In this chapter, this *in vitro* reconstitution approach is described, which forms the basis for the work

herein described. Further methodological details, or modifications for specific experiments are detailed within each respective subsequent chapter.

2.2 Protein purification

To obtain purified protein, we can use several different approaches, depending on the protein. The most essential protein for this work is tubulin, the building block of microtubules. To achieve a high yield of purified tubulin, we extract it from the brain tissue of *B. taurus* or *S. scrofa*, since neurons are highly enriched with dense microtubule networks (Castoldi and Popov, 2003; Gell et al., 2011). The methodological workflow is as follows: First, the fresh brain tissue is cleaned of any unwanted debris, such as membranes or bone fragments, and homogenized. The homogenized tissue is clarified to remove the insoluble cellular components, leaving the soluble fraction. While several different purification schemes at this point are possible, we either use a phosphocellulose column or a high molarity buffer purification method. For the bovine tubulin used in this work, it was purified with the high molarity buffer method, and the porcine tubulin was purified with a phosphocellulose column. We take our clarified tissue sample and use microtubule-compatible buffers to put the sample through iterative rounds of temperature-sensitive microtubule polymerization and depolymerization and ultracentrifugation to isolate the competent tubulin. The high molarity conditions are permissive to microtubule dynamicity but help to rid the sample of unwanted microtubule-associated proteins by decreasing the binding affinity. Once we obtain our final purified tubulin sample, we covalently label it with fluorescent dyes (Alexa Fluor-488, Cy5, Alexa Fluor 647, Invitrogen) for visualization with fluorescent microscopy (Hyman et al., 1991).

Other proteins, such as MAPs, may be purified from more standard biochemical protein expression and purification protocols. The two major systems that we use for this are *E. Coli* bacterial cells and *S. frugiperda* (Sf9) insect cells. Using *E. Coli* for protein expression and purification is faster and simpler than the Sf9 insect cell system, but it is limited to proteins that are smaller, less complex, and require less folding, like EB1 (Zanic et al., 2009). More complex proteins, such as kinesin motors, typically are better expressed in insect cells due to the lack of important chaperone proteins and premature translation truncation in bacteria (Schmidt, 2004; Kurland and Gallant, 1996; Korten et al., 2016).

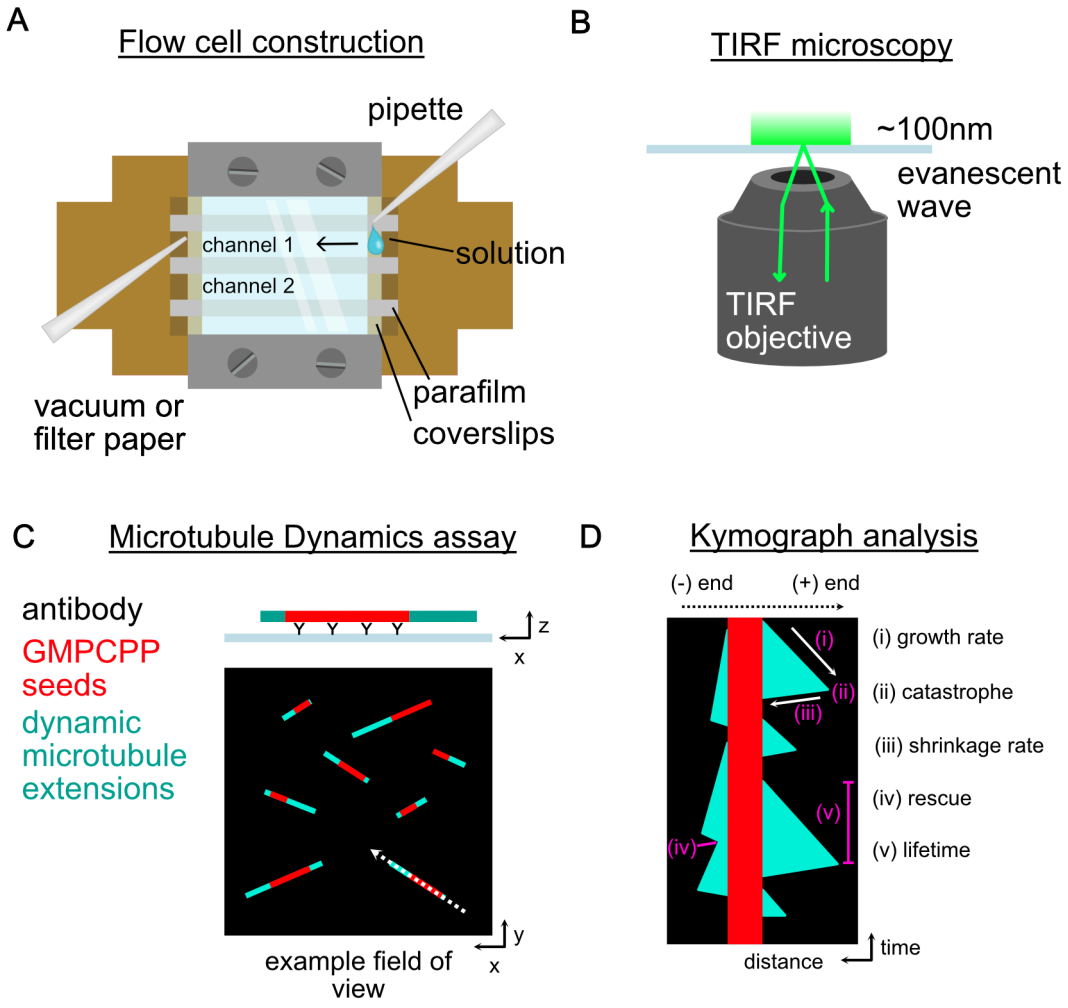

Figure 2.1 Schematics related to *in vitro* reconstitution of microtubule dynamics. (A) Schematic of a flow cell, showing the custom brass adaptor, and coverslips with strips of parafilm creating two separate channels. Reaction mix is added to one side of the channel, and drawn through with a vacuum or filter paper, once the channel is properly hydrated. (B) Schematic indicating the light path in a TIRF microscopy set-up. The light travels through the objective and is set at a critical angle, such that it reflects off the coverslip back down into the objective. An evanescent wave field is created with an approximate depth of 100nm, illuminating only the fluorescent sample in that region, and no further, limiting the background signal. (C) Schematic illustrating how microtubules are bound to the coverslip: stabilized GMPCPP seeds are bound through antibody attachment, and dynamic tubulin extensions are grown off the seeds from the addition of soluble tubulin, GTP, and other buffer components. A schematic example of an image from the microscopic field of view of the dynamics assay is also shown. (D) A schematic example of a kymograph, created by drawing a line through a microtubule from a time lapse, and plotting each frame of the microtubule over time to create a time-distance plot of the region. The red portion is the static seed over time, and dynamic extensions grow and shrink at both ends over time, creating triangular events. Growth rate is calculated from the slope of the

growth event, and shrinkage rate from the slope of the shrinkage event. Catastrophe frequency is calculated from counting the number of catastrophes (the transition from growth to shrinkage) over time. Rescue marks the transition from shrinkage to growth, where the shrinkage event does not terminate at the seed, but rather switches on an existing extension. Lifetime is a similar, but inverse, measurement to catastrophe, where the time spent in growth is measured.

2.3 Microtubule dynamics assay

The basic assay presented in this work is the microtubule dynamics assay, in which fluorescently labeled dynamic microtubules are grown off of a stable microtubule template. This is the starting point for a large portion of the work presented here, which sometimes has additions or modifications, depending on the question, but the basic experimental principles are nearly the same. First, to eliminate background signal from debris, we clean glass coverslips with piranha solution (30/70% v/v hydrogen peroxide and sulfuric acid) to obliterate any organic matter on the glass, and then coat then with a hydrophobic silane surface to repel any further debris. We construct flow cells in custom brass coverslip holders by assembling together 18 × 18-mm and 22 × 22-mm coverslips separated by parafilm, briefly melted to create channels 0.1 mm thick, 2–3 mm wide, and 18 mm long. Glass coverslips were cleaned in piranha solution (3:7 H_2O_2/H_2SO_4 by volume) before silanization with a 0.05% solution of dichlorodimethylsilane in trichloroethylene, as previously described (Gell et al., 2010). We passivate the coverslip surface with an antibody for microtubule seed attachment, most often anti-rhodamine in a 1:50 dilution, for 5 minutes before passivating with Pluronic F127 for 30 minutes to block non-specific protein binding to the surface. Washes in between steps are done with BRB80 (80 mM Pipes/KOH, pH 6.8, 1 mM $MgCl_2$, and 1 mM EGTA). To serve as nucleation templates in our dynamic assay, we grow GMPCPP-stabilized microtubule seeds labeled with rhodamine in a 1:3 ratio of rhodamine-labeled to unlabeled tubulin at 37°C for 1 h, before diluting them and spinning them down at 20

pounds per square inch (126,000 × *g*) for 5 min (Gell et al., 2011). The pellet of concentrated seeds is re-suspended in 100 µl BRB80 and diluted 5–20 times for use in experiments. These are added into the flow cells to serve as templated nucleation sites off of which dynamic extensions will grow at both microtubule ends. The addition of a reaction mix containing BRB80, purified soluble tubulin with a fluorescent dye (labeling ratio between 5-10% of the tubulin concentration), 1 mM GTP, and anti-fade solution: 40 mM D-glucose, 40 µg/ml glucose oxidase, 16 µg/ml catalase, 0.08 mg/ml casein, 10 mM dithiothreitol (DTT), and 50 mM KCl. is the final step to constitute a dynamics assay (Zanic, 2016). This assay can be modified to include different buffer conditions, nucleotides, concentration of soluble tubulin, or the addition of microtubule-associated proteins in order to use them as a tool for understand certain mechanistic insights, or to understand their effect on microtubule dynamics themselves. Specific methods pertaining to individual experiments are described in the respective chapters.

2.4 TIRF microscopy

In combination with biochemical *in vitro* reconstitution, we use total internal reflection fluorescence (TIRF) microscopy to image the conditions we wish to measure. TIRF microscopy relies on the principle of setting the direction of a fluorescent light path to a critical angle at which the light beam directed out of a microscope objective is bent back into the objective itself, rather than through the sample. An evanescent wave is thus created at the interface of the objective and the coverslip containing the sample, which is enough to illuminate approximately 100nm of depth into the sample. Using this approach on cellular samples is useful for specifically imaging the cell membranes without capturing any additional fluorescent signal from within the cell. For our *in vitro* reconstitution approach, this microscopic method is essential for

achieving high-quality imaging. Microtubules are approximately 25nm in diameter, which is well within the 100nm imaging depth. By using TIRF microscopy as opposed to other fluorescent microscopy approaches, we eliminate a great deal of background signal by shortening the z-range, which increases our signal-to-noise ratio of the fluorescent microtubules on the coverslip in the presence of the fluorescent soluble tubulin in solution. For the work herein, unless otherwise specified, imaging was performed as previously described (Lawrence et al., 2018) using a Nikon Eclipse Ti microscope with a 100×/1.49 NA TIRF objective and Andor iXon Ultra EM-CCD (electron-multiplying charge-coupled device) and NEO sCMOS (scientific complementary metal-oxide semiconductor) cameras; 488-nm, 561-nm, and 640-nm solid-state lasers (Nikon Lu-NA); Finger Lakes Instruments HS-625 high-speed emission filter wheel; and standard filter sets. An objective heater was used to maintain the sample at 35°C. Images were acquired using NIS-Elements (Nikon). Dynamics movies were imaged for 30 minutes at 0.2 FPS unless otherwise indicated.

2.5 Microtubule dynamics analysis

Microtubule dynamics were analyzed by creating kymographs of dynamic microtubules in FIJI (Schindelin et al., 2012) using a custom-made plug-in. For a given time lapse movie of microtubule dynamics, lines were drawn in FIJI with a linewidth of 5 pixels over microtubules in the maximum projected intensity image of the movie. If movies exhibited any stage drift, an Image Stabilizer (Image J) plug-in was used. Polarity of microtubules was determined by comparison of growth rates at each end of the microtubule: faster growing ends were categorized as plus ends, and slower ones were categorized as minus ends. Microtubule dynamics parameters were determined as previously described (Zanic, 2016). Briefly, growth rates were determined

by calculating the difference in distance over time between the start and end of a growth event. Catastrophe frequency was determined as a ratio of the total number of catastrophes observed over the total time microtubules spent in growth for a given movie. Microtubule lifetimes were defined for individual growth events as the total time from the onset of microtubule growth until the onset of catastrophe. Only fully observable lifetime events with a clearly defined start and end were included in any lifetime analysis. Shrinkage rate was determined by calculating the difference in distance over time between the start and end of the shrinkage event. I used a custom MATLAB script to calculate these parameters from a manual input of indicating the coordinates of microtubule growth and shrinkage events on the kymographs.

Chapter 3

Microtubule minus-end stability is dictated by the tubulin off-rate

Adapted from:

Strothman, C., V. Farmer, G. Arpağ, N. Rodgers, M. Podolski, S. Norris, R. Ohi, and M. Zanic. 2019. Microtubule minus-end stability is dictated by the tubulin off-rate. *J. Cell Biol.* 218:2841–2853. doi:10.1083/jcb.201905019.

3.1. Introduction

Microtubules undergo a unique behavior termed dynamic instability, in which microtubule ends stochastically transitions between phases of growth and shrinkage, independent of one another. Early *in vitro* reconstitution studies demonstrated that, although both microtubule ends exhibited dynamic instability, minus ends had distinctly slower growth rates and less frequent transitions from growth to shrinkage, termed "catastrophe"(Bergen and Borisy, 1980; Mitchison and Kirschner, 1984; Horio and Hotani, 1986; Walker et al., 1988). Microtubules grow by addition of GTP-bound tubulin subunits, and incorporation of tubulin dimers into the polymer triggers GTP-hydrolysis in the β-tubulin subunit after a brief delay, resulting in a 'cap' of GTP-tubulin at growing microtubule ends. The process of GTP-hydrolysis induces structural changes in the microtubule lattice, ultimately resulting in catastrophe if the cap is lost (Carlier and Pantaloni, 1981; Nogales et al., 1998; Walker et al., 1991; Voter et al., 1991; Zhang et al., 2015; Duellberg et al., 2016a). Over the last few decades, a myriad of analytical and computational models of microtubule catastrophe have emerged. They range from complex

descriptions involving dozens of parameters, most of which are still not experimentally tractable, to simpler ones, employing kinetic rates of tubulin addition, removal, and hydrolysis, aiming to capture the key features of microtubule dynamics (Bowne-Anderson et al., 2013). Our models of microtubule dynamics are almost exclusively based on the plus-end behavior. For example, it is thought that the size of the GTP-cap plays an essential role in plus-end stability (Duellberg et al., 2016a). Furthermore, it has been shown that plus-end catastrophe is not a single-step random process, rather, the probability of catastrophe increases over time, such that microtubule plus-ends effectively age (Odde et al., 1995; Gardner et al., 2011b). To what extent our understanding of the plus-end dynamics applies to the minus ends remains unknown. In this study, we use biochemical *in vitro* reconstitution with purified protein components and total internal reflection fluorescence (TIRF) microscopy to directly interrogate minus-end dynamics. In particular, we focus on determining the kinetic rates of tubulin assembly and the size of the stabilizing cap at minus ends in the absence of additional regulators.

3.2. Results

3.2.1. Microtubule minus ends undergo catastrophe less frequently than plus ends, when controlling for the growth rate

To investigate the relationship between microtubule growth and catastrophe at minus ends, we used an established *in vitro* microtubule dynamics assay (Gell et al., 2011; Zanic, 2016). We grew dynamic microtubule extensions from GMPCPP-stabilized microtubule 'seeds' over a range of tubulin concentrations (4 to 13 μM) and imaged them using TIRF microscopy. The two microtubule ends were differentiated based on their relative growth rates (Figure 3.1A). We determined the tubulin on-rate at each end using a linear regression of the growth rate as a

function of tubulin concentration (Figure 3.1B, see Methods). We found the minus-end tubulin on-rate to be nearly 4 times smaller than that of the plus-end (0.88 ± 0.04 μM^{-1} s^{-1} vs. 3.3 ± 0.02 μM^{-1} s^{-1},SE, respectively), consistent with previous reports (Bergen and Borisy, 1980; Mitchison and Kirschner, 1984; Walker et al., 1988; O'Brien et al., 1990; Trinczek et al., 1993).

Measurements of catastrophe frequency revealed an eight-fold decrease over the range of 4 to 13 μM tubulin at the plus end (0.45 ± 0.05 min^{-1} to 0.057 ± 0.008 min^{-1}, SE), consistent with previous reports (Walker et al., 1988; Drechsel et al., 1992; Gardner et al., 2011b) (Figure 3.1C). Minus ends were relatively stable in all of our experimental conditions and displayed only a two-fold decrease in catastrophe frequency over the same range of tubulin concentrations (4 μM to 13 μM tubulin: 0.22 ± 0.06 min^{-1} to 0.13 ± 0.01 min^{-1}, SE) (Figure 3.1C). Both ends exhibited a trend in which increasing growth rates were accompanied by a decrease in catastrophe frequency (Figure 3.1D). However, comparison of plus and minus ends growing at similar growth rates (~7 nm s^{-1}), achieved using different tubulin concentrations, revealed nearly a four-fold lower catastrophe frequency at the minus end (Figure 3.1D, shaded region). The finding that minus ends undergo catastrophe less frequently than plus ends when controlled for the growth rate emphasizes key differences in the dynamics of the two ends.

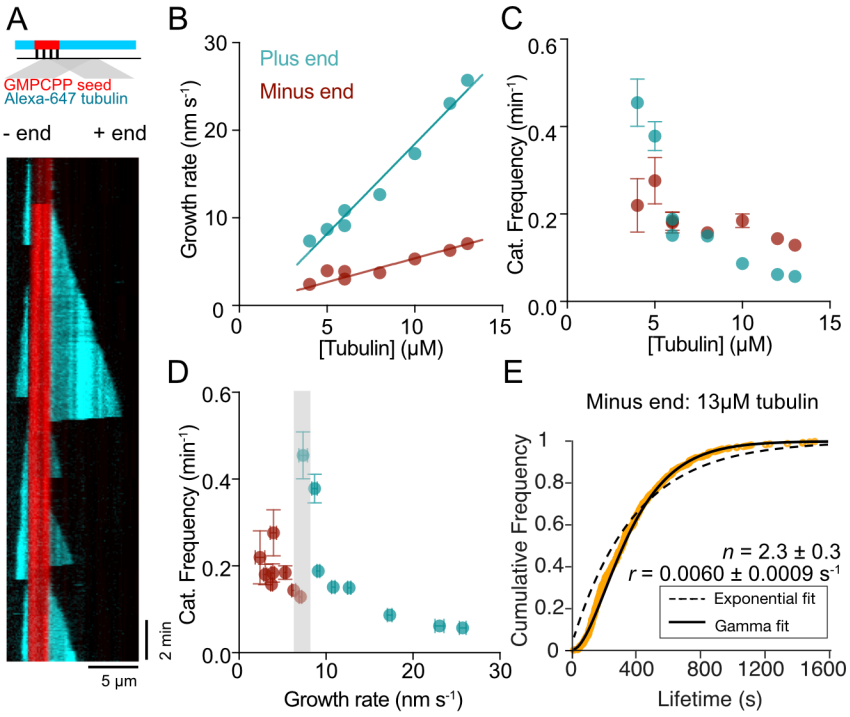

Figure 3.1. Minus ends have distinct dynamics and undergo aging during growth. (A) (Top) Schematic showing experimental set-up. (Bottom) Representative kymograph showing characteristic differences between the two microtubule ends (8 µM tubulin). (B) Microtubule growth rates as a function of tubulin concentration. Error bars represent SE of each independent experiment per condition. Any error bars that are not visible are smaller than the size of the data point. (C) Microtubule frequency of catastrophe as a function of tubulin concentration. Error bars represent counting error. (D) Microtubule frequency of catastrophe replotted as a function of corresponding growth rate, data from panels B and C. Shaded area indicates matching growth rates of plus and minus ends. (E) Cumulative distribution of lifetimes of minus ends (13 µM tubulin). Lifetimes were pooled from 2 independent experiments (N = 417). Dashed line represents exponential fit, and solid line represents gamma fit. See Methods for experimental details.

3.2.2. Minus-end catastrophe is not a single-step random process

One potential difference in the catastrophe mechanism at the two ends may be due to distinct aging processes, as suggested by earlier studies (Odde et al., 1995). To further explore

this possibility, we measured the microtubule lifetime distributions at both ends with increased spatiotemporal resolution and larger sample sizes (N = 417-1206 lifetimes per condition) compared to the previous study (Odde et al., 1995). We found that distributions of minus end lifetimes were well fit by a gamma function (see Methods) at both low (6 μM) and high (13 μM) tubulin concentrations (Figure 3.1E, Figure 3.2A). None of the distributions, at either the plus or minus end, were well fit by a single-exponential function, as evidenced by the gamma function step parameters distinct from 1 (Figure 3.1E, Figure 3.2). At 13 μM tubulin, minus-end lifetimes had a step parameter of 2.3 ± 0.3, 95% CI. Furthermore, the comparison of gamma fit parameters at plus and minus ends growing with 6 μM tubulin revealed similar step parameters (minus: 2.0 ± 0.2 vs. plus: 1.7 ± 0.1, 95% CI) (Figure 3.2B*).* We conclude that similar to plus ends, minus ends also undergo aging, and that a distinct aging mechanism at the minus end is not the cause of the observed differences in dynamics between the two ends.

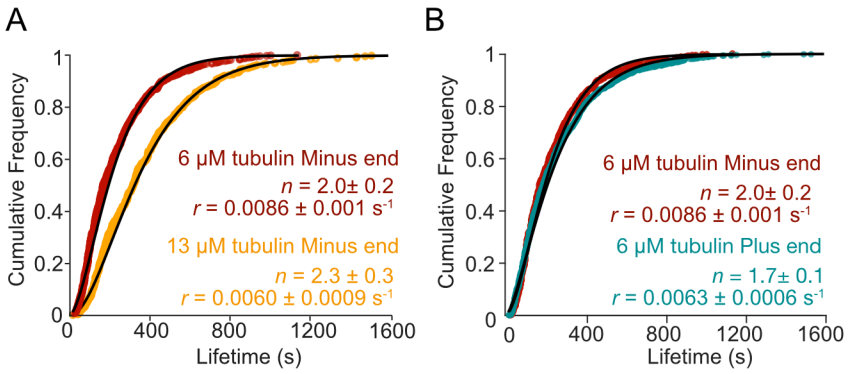

Figure 3.2. Minus-end catastrophe is not a single-step process. (A) Minus-end lifetimes grown at 13 μM tubulin (gold; data from Fig. 1 E), replotted along with CDF of lifetimes of minus ends grown at 6 μM tubulin (red; N= 705). Data from two independent experiments. Solid lines represent best gamma fits. (B)Minus-end lifetimes grown at 6 μM tubulin (red), re-plotted along with CDF of lifetimes of plus ends grown with 6 μM tubulin (teal; N= 1,206). Data from two independent experiments. Solid lines represent best gamma fits. *n* and *r* rate parameters represent gamma distribution step and rate parameters, respectively.

3.2.3 Microtubule minus ends have small cap sizes, set by slow growth rate

Next, we considered whether distinct dynamics at the two ends could be explained by the relative size of their stabilizing caps. The size of the GTP-cap is set by the difference in the microtubule growth rate and the GTP-hydrolysis rate (see Methods), and can be inferred by localization of EB-family proteins, which recognize the nucleotide state of tubulin and display a 'comet'-like localization at growing microtubule ends (Zanic et al., 2009; Maurer et al., 2012; Seetapun et al., 2012; Zhang et al., 2015). Previous studies of microtubule plus ends found that the EB comet size increased with the increasing tubulin concentration, correlating with the increase in microtubule growth rate (Bieling et al., 2007). Additionally, increase in growth rate (achieved by increasing tubulin concentration) is typically accompanied by suppression of catastrophe frequency (Walker et al., 1988; Drechsel et al., 1992; Gardner et al., 2011b), presumably due to the larger size of the stabilizing nucleotide cap (Duellberg et al., 2016a; Rickman et al., 2017). We thus wondered whether the enhanced stability of microtubule minus ends is a result of inherently larger stabilizing nucleotide caps at minus ends.

To compare the size of the GTP-cap at plus and minus ends, we analyzed localization of EB1-GFP at growing microtubule ends (Figure 3.3). A direct comparison of EB1 comets at ends of microtubules grown with 40 μM tubulin revealed that slower-growing minus ends have on average shorter EB1 comet decay lengths (minus end: 272 ± 10 nm, 95% CI, N ≥ 865 linescans; plus end: 383 ± 20 nm, 95% CI, N ≥ 587 linescans), (Figure 3.3B, closed circles). To investigate whether the growth rate alone sets the size of the EB1 comets at both ends, we then used 20 μM tubulin to obtain slow plus-end growth rates to match those measured at the minus ends at 40 μM tubulin (Figure 3.3B, open circles). We found that in 20 μM tubulin, plus ends grew at the same

rate (35 ± 3 nm s^{-1}, SE, N = 59) as minus ends in 40 μM tubulin (34 ± 5 nm s^{-1}, SE, N = 29), and that the corresponding average comet lengths were matched in these conditions (plus end at 20 μM tubulin: 276 ± 28 nm 95% CI, N ≥ 1220 linescans; minus end at 40 μM tubulin: 272 ± 10 nm 95% CI, N ≥ 865 linescans). Our results demonstrate that average EB1 comet size is set by the average growth rate, irrespective of the microtubule end. Importantly, even in the presence of EB1, minus ends exhibited lower frequency of catastrophe as a function of growth rate than plus ends over a range of tubulin concentrations (Figure 3.4A). In other words, when plus and minus ends are growing at the same growth rates (in different tubulin concentrations), their cap sizes are equivalent, yet minus ends have longer lifetimes. We thus conclude that the average size of EB1 comets alone does not define microtubule lifetime.

To measure minus end cap size in the absence of EB1, we performed tubulin dilution experiments. Here, we grew dynamic microtubules in the presence of 6, 12, or 18 μM tubulin in a microfluidic device and, while imaging, rapidly exchanged solutions to wash out soluble tubulin with sub-second resolution (Figure 3.4B). Consistent with previous reports (Voter et al., 1991; Walker et al., 1991; Duellberg et al., 2016a; Ti et al., 2016), we observed a characteristic delay between tubulin washout and the onset of microtubule catastrophe, which we interpreted as the time during which the stabilizing cap is lost. We found that, in all investigated conditions, minus ends displayed lower average delay times than plus ends (average across conditions: minus end: 4.7 ± 0.3 s, SE, N = 160; plus end: 8.6 ± 0.3 s, SE, N = 271) (Figure 3.3C-D). Delay times increased with instantaneous growth rate determined prior to dilution (Figure 3.4C), consistent with the idea that faster growth rates result in larger stabilizing caps. Similar to a recent finding for microtubule plus ends (Duellberg et al., 2016a), we observed slight

depolymerization of both microtubule ends during the delay period, distinct from the fast microtubule depolymerization that follows catastrophe. We found that the shrinkage length prior to catastrophe scaled with the average growth rate prior to washout, with minus end shrinkage lengths smaller than those observed at plus ends (Figure 3.4D). Based on these results, we conclude that growing minus ends have smaller stabilizing nucleotide caps than plus ends, corresponding to their slower growth rates. Therefore, the increased stability of minus ends cannot be explained by the relative size of their stabilizing caps.

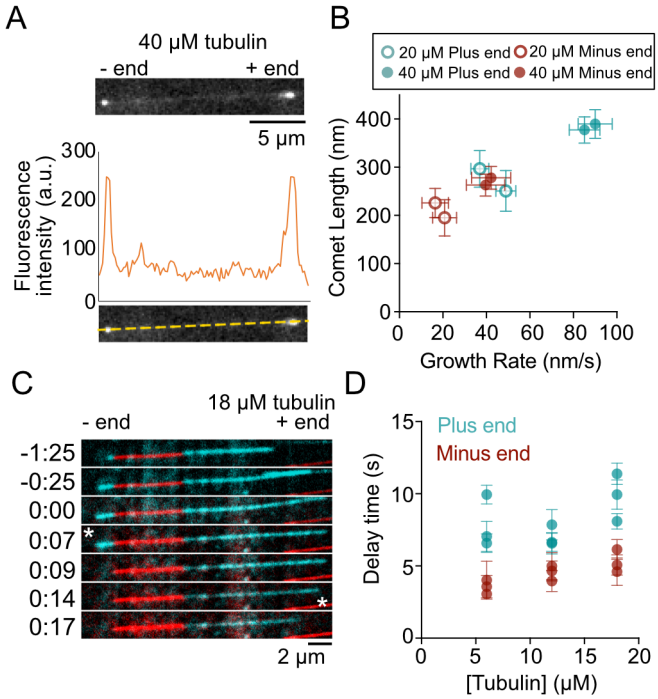

Figure 3.3. Minus end cap size is small and scales with growth rate. (A) Representative image of EB1-GFP at both growing ends of a single microtubule (40 µM tubulin). A line scan was drawn along this microtubule to generate intensity values along the microtubule, showing two distinct peaks at either end. (B) Average EB1 comet length as a function of average growth rate of plus and minus ends in 20 or 40 µM tubulin with 200 nM EB1-GFP. Two independent repeats were done for each condition. Comet length error bars are 95% CI from the fit. Growth rate is weighted average of individual growth events and error is weighted SD. Weights are determined as the inverse of 95% CI of the linear fit to individual growth events. (C)

Representative time lapse of a microtubule pregrown with 18 μM tubulin undergoing tubulin washout. 0:00 timepoint indicates time of washout; asterisks indicate time of catastrophe for each end. (D) Mean delay times for each end are shown from three independent repeats of each tubulin concentration.

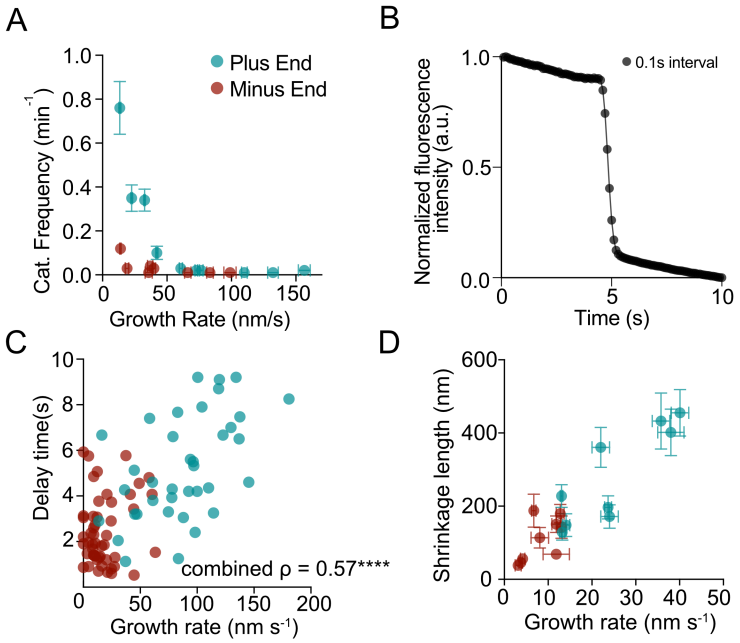

Figure 3.4. Minus ends have similar cap sizes, but longer lifetimes, than plus ends at a given growth rate. (A) Catastrophe frequency as a function of growth rate for a range of tubulin concentrations with 200 nM EB1-GFP. Concentrations of 20, 30, 40, 50, and 60 μM tubulin were used for both ends, and 12 μM tubulin was additionally used for plus-end measurements. Catastrophe frequency error is counting error, and growth rate error is SEM.(B) Representative fluorescence intensity profile of background fluorescence of Alexa Fluor 647–labeled tubulin in solution during microfluidic washout. (C) Delay time as a function of instantaneous growth rate at plus and minus ends grown in 20 μM tubulin. Corresponding delay times after dilution per microtubule are shown. All points shown from three independent repeats. Spearman's rho test = 0.57; ****, P≤0.0001. (D)Average shrinkage length during delay time from Fig. 3.3, C and D, plotted against the average growth rate per condition taken from the microtubule population (separated by plus and minus end).

3.2.4 GMPCPP-tubulin off-rate at minus ends is significantly lower than that at plus ends

While our results showed that the size of the GTP-cap alone is not the determinant of minus-end lifetime, we wondered whether any potential differences in the off-rate of GTP-tubulin incorporated into growing microtubule ends may play a significant role in setting the microtubule catastrophe frequency (Bowne-Anderson et al., 2013). Based on a classic model of biological polymers (Oosawa, 1970), the 1st order GTP-tubulin off-rate (k^T_{off}) can be determined from the y-intercept of the linear regression for microtubule growth rate as a function of tubulin concentration (Figure 3.1B). Notably, in this representation, the k^T_{off} is so small that it has essentially no effect on the microtubule growth rate at tubulin concentrations needed for robust microtubule elongation, and can therefore not be precisely determined (Gardner et al., 2011a).

An alternative approach to determine the k^T_{off} is to measure the depolymerization rate of microtubules grown with GMPCPP, a slowly-hydrolysable GTP analog (Hyman et al., 1992). The GMPCPP microtubule lattice structure was recently validated as a faithful structural mimic of GTP-microtubule lattice (Zhang et al., 2018), however, a direct comparison of GMPCPP-microtubule plus- and minus-end depolymerization rates has not been reported previously. To measure the GMPCPP-microtubule depolymerization rate at both ends, we polarity-marked microtubules with Cy5-labeled GMPCPP-tubulin, so that faster-growing plus ends had larger stretches of Cy5-tubulin (Figure 3.5A, see Methods). By observing GMPCPP-microtubule depolymerization over 15 hours, we determined that the minus end had significantly lower tubulin off-rate at 0.05 ± 0.004 s^{-1}(SE, N = 56), when compared to the plus end off-rate: 0.14 ± 0.006 s^{-1}(SE, N = 72) (Figure 3.5B). Given this significant difference in the tubulin off-rate at the two ends, we hypothesize that although the absolute size of the GTP-cap is smaller, the minus-

end GTP-cap may be more stable. Thus, we conclude that the difference in the tubulin off-rate may be the primary determinant of minus-end lifetime.

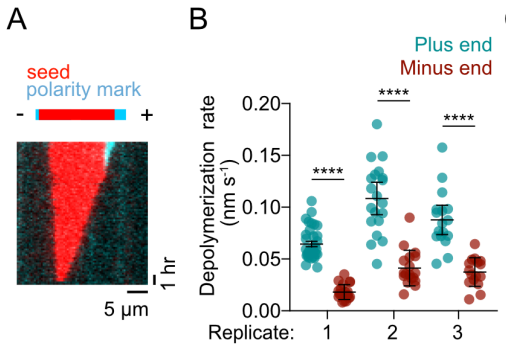

Figure 3.5. Minus ends have a lower tubulin off-rate. (A) Representative kymograph of a polarity-marked GMPCPP-seed depolymerization experiment. Plus and minus end denoted on kymograph. (B) Depolymerization rates of polarity marked GMPCPP microtubules from three independent experiments. Mean and SE plotted for each group (N ≥16). ****p-value ≤ 0.0001 using unpaired t-tests.

3.3. Discussion

Microtubule catastrophe occurs via the loss of a protective cap of GTP-tubulin, the size of which is widely considered to be the determinant of microtubule plus-end stability. The interplay between the growth rate and the GTP hydrolysis rate, which set the size of the GTP-cap, show that for the plus end, typically, larger GTP sizes correlate with increased stability. At the most fundamental level, increasing tubulin concentration in *in vitro* dynamics assays increases average growth rate, decreases the frequency of catastrophe, and increases the average EB-comet size of plus ends (Bieling et al., 2007; Walker et al., 1988; Drechsel et al., 1992;

Gardner et al., 2011b; Duellberg et al., 2016a). Indeed, modulation of the GTP cap size set through changes in the GTP hydrolysis rate from certain tubulin isotypes, or regulation through microtubule associated proteins has been shown to be a mechanism for regulating plus-end stability (Chaaban et al., 2018; Maurer et al., 2014; Zhang et al., 2017, 2018). Structural studies have proposed that the binding of a new terminal tubulin dimer completes the GTP-pocket of the previously exposed β-tubulin subunit, triggering the GTP-hydrolysis in the penultimate dimer at the growing microtubule plus end (Nogales et al., 1998, 1999; Alushin et al., 2014). However, the minus end only exposes α-tubulin subunits, thus, it is not clear whether the minus end may have a differing mechanism or rate of GTP-hydrolysis. What is clear, however, from our results is that the average size of the GTP cap is not the primary determinant of stability. Our finding of the lower GTP-tubulin off-rate at minus ends implicates that, although the minus end cap may be small, it is likely more stable than that at the plus end. Given that even a couple of layers of unhydrolyzed tubulin are sufficient to prevent microtubule catastrophe (Drechsel and Kirschner, 1994; Caplow and Shanks, 1996), we conclude that the small, but stable GTP-tubulin cap may be the key to minus end longevity. This idea that the mean GTP cap size is not the primary determinant of microtubule catastrophe is supported by other recent work- XMAP215 is a microtubule polymerase that increases plus end growth rate; however, catastrophe is strongly increased in these conditions, despite the presence of large GTP cap sizes (Farmer et al., 2020).

This work defines the key molecular rates underlying microtubule minus-end dynamics and sets the stage for future studies to investigate other contributing factors to dynamics, such as structural differences and differences in bond energies between the two ends. The relative contribution of these molecular parameters that give rise to fundamentally different dynamics at the two ends may also inform future computational models to describe the mechanisms of

dynamics, such as growth and catastrophe.

3.4. Methods

3.4.1 Protein Purification

Bovine and porcine tubulin was purified and labeled with fluorescent dyes are previously described in Chapter 2. EB1-GFP was expressed in *Escherichia coli* and purified as previously described (Zanic et al., 2009) and stored in 10 mM Bis-Tris, 10 mM TrisHCl, 100 mM KCl, 1mM DTT, 5% glycerol, pH 6.6. Protein concentration was determined using absorbance at λ =280 nm or a Bradford assay (Kielkopf et al., 2020).

3.4.2 Dynamics assays

Tubulin titration was performed as previously described in Chapter 2, and tubulin concentrations are indicated within the figures. For the dynamics experiments to measure the cumulative distribution of lifetimes, experiments used slightly different imaging conditions to detect small microtubule lifetime events. Dynamic microtubules grown with 6 μM or 13 μM tubulin were imaged for 1 hour at 0.3 FPS, using an Optovar increased magnification (1.5×) to achieve a pixel size of 106 nm. Imaging was delayed for 10 min to allow the chamber to reach steady state. For microtubule dynamics assay with EB1-GFP comets, conditions were the same as described above with the following exceptions: 17 mM KCl and 0.01% methylcellulose were used in the imaging reaction. Images were taken at 0.5 FPS. All of the dynamics experiments were imaged using the EM-CCD camera.

3.4.3 Microfluidic device preparation

Y-shaped microfluidic devices were prepared similarly to those previously described by Duellberg et al. (2016), but with two branched inlets instead of three. Silicon molds with negative channel patterns were produced using deep reactive ion etching. A mixture of polydimethylsiloxane (PDMS) and curing agent (Dow Corning; 10:1 wt/wt) was poured over a mold, degassed for 20 min at room temperature, and polymerized for 4 h at 60°C. Holes for the inlet and outlet channels were created in the peeled-off PDMS block using biopsy punchers (Miltex; diameter 1.5 mm). The structured side of the PDMS and a 22 × 22-mm glass coverslip were treated with air plasma (PDC-32G; Harrick Plasma) for 20 s. A small area of 4 × 10 mm, where imaging was to occur, was protected from plasma radiation by a small PDMS block to ensure the integrity of the surface functionalization. Immediately after plasma treatment, the exposed sides were bonded to form the channels, and tubing (Tygon; inner diameter of 0.5 mm) was connected to the PDMS inlets/outlet and Hamilton gas tight syringes (1,000 ml total volume; used for channel preparation only). The microfluidic devices were used for TIRF microscopy experiments immediately after assembly.

3.4.4 Dilution experiments

Fast solution exchange in the micro-channel was achieved by switching the flow from two different inlets that were controlled by independent pumps (OB1 MK3; ElveFlow) and flow sensors (MFS2 and MFS3; ElveFlow) between pumps and inlets. To assemble a sample, short GMPCPP-stabilized, TMR-labeled microtubule seeds were introduced through one inlet and allowed to attach to the functionalized glass surface. To initiate microtubule growth, 6, 12, or 18 µM 20% Alexa Fluor 647–labeled tubulin was introduced through the first inlet at a constantly maintained flow rate of 7 µl/min for 90 s, and then flow was stopped for the remaining growth

period. Imaging buffer was supplemented with 0.05% methylcellulose. After a short period of growth (5–10 min), sub-second tubulin washout was induced using a 50 µl/min flow of a washout reaction containing BRB80 and anti-fade, unchanged from the initial growth reaction besides tubulin. Plus and minus ends were differentiated by average growth rates before washout. Imaging during the growth phase was performed at 0.2 FPS and imaging of the 640-nm channel just before, during, and after washout was performed at 10 FPS for tubulin-only conditions using the CMOS camera (70-nm pixel).

3.4.5 GMPCPP seed depolymerization

GMPCPP depolymerization experiments were done by growing TMR-labeled seeds as described in Chapter 2 Polarity marking was performed by incubating the coverslip-attached GMPCPP seeds with 0.5 µM 7% Cy5-labeled bovine tubulin with 1 mM GMPCPP in the imaging buffer (without GTP) for 15 min. All tubulin was then washed out with BRB80/anti-fade solution (without GTP), and the chambers were sealed with valap (33% wt/wt Vaseline, lanolin, and paraffin wax). Images were taken every 10 min for 15 h on the EM-CCD camera.

3.4.6 Analysis of cumulative distribution function

Cumulative distributions of lifetimes and fits to exponential and gamma distributions were performed as previously described (Gardner et al., 2011b; Zanic, 2016). Specifically, for each condition, all lifetimes were used as input, and the best fit gamma parameters were determined using the gamfit function in the MATLAB Statistics toolbox (MathWorks, Inc.), specified by the gamma probability density function

$$f\ (t|n,\ s)\ =\ \frac{t^{n-1}e^{-t/s}}{s^{n}\Gamma(n)}\ ,$$

where $\Gamma(n)$ is the gamma function, *n* is a "shape" (also known as "step") parameter, and *s* is a "scale" parameter. The function gamfit returns maximum likelihood estimates and CIs for the shape and scale parameters. The reported rate parameter *r* was determined as the inverse of the scale parameter, $r = 1/s$, and the error was propagated from the CIs for the scale parameter.

3.4.7 Tubulin on- and off-rates

GTP-tubulin on- and off-rates were determined from measured growth rates as a function of tubulin concentration by linear regression analysis in MATLAB (MathWorks, Inc.), assuming

$$v_g = \frac{d}{13}\left(k_{on}[Tb] - k_{off}\right),$$

where $d = 8$ nm is the size of a tubulin dimer, k_{on} is the second order GTP-tubulin on-rate constant, and k_{off} is the first order GTP-tubulin off-rate constant. Given the relatively small values and large uncertainties in the y-intercept, this method is deemed not reliable for precise determination of the GTP-tubulin off-rate. For this reason, k_{off} was additionally determined from the depolymerization rate of GMPCPP microtubules, assuming a 14-protofilament microtubule structure, as previously described (Hyman et al., 1992). GMPCPP microtubule depolymerization rates were calculated by placing points at the beginning and end of each shrinkage event and categorized as plus or minus end based on polarity marking.

3.4.8 EB1-comet length analysis

Image analysis was performed by generating kymographs of microtubule growth events. For each tubulin concentration, 20 microtubules for which both plus and minus ends could be analyzed were selected to determine catastrophe frequency, average growth rate, and average EB1-comet length. The characteristic decay length of the EB1 comets was determined using custom MATLAB functions. The microtubule tip location for each time frame was estimated by fitting a line through two manually clicked points at the beginning and end of a growth event on each kymograph. The pixel with the brightest EB1 intensity within ±5 pixels of the estimated tip location was determined for each time frame and assigned as the bona fide microtubule tip location. Average tip intensity (I^{tip}) and its SD (σ^{tip}) of a given growth event were calculated, and any time frames with tip intensity lower than $I^{tip}-\sigma^{tip}$ were excluded. The remaining points were used to fit a linear function to approximate the growth rate. Time frames with fit residuals more than one SD away from the mean residuals were excluded. The remaining points were used to fit a linear function to determine the growth rate of the given event. For each time frame within the given growth event, the microtubule tips were aligned, and an average intensity profile was calculated. The lattice intensity was determined by averaging the intensity values between 20 and 25 pixels away from the tip. This average lattice intensity was subtracted from intensity profiles from each remaining time frame. Manual inspection was performed to remove any growth events in which the tip locations were not successfully determined by the above automated procedures. The remaining growth events were used to determine the average growth rate (v_g) and its SD (σ_{v_g}) weighted with inverse of the 95% CI of the fitting procedure. Individual growth events were further excluded if they were not within $v_g \pm \sigma_{v_g}$. Individual intensity profiles from each individual time frame from the remaining growth episodes were used to generate a super-

averaged intensity profile. The super-averaged intensity profile in the range of 1 pixel in the solution background and 20 pixels along the microtubule lattice was fit to an exponential decay convolved with a Gaussian function, given by

$$\frac{A}{2}\left[e^{\left(\frac{\sigma^2}{2\lambda^2}-\frac{x-x_0}{\lambda}\right)}\right]\left[1+erf\left(\frac{x-x_0}{\sigma\sqrt{2}}-\frac{\sigma}{\lambda\sqrt{2}}\right)\right]+\frac{B}{2}\left[1+erf\left(\frac{x-x_0}{\sigma\sqrt{2}}\right)\right],$$

where A is the intensity value at the tip, B is the difference between average lattice intensity and solution background, σ is the experimentally determined full width at half maximum of the point spread function, x_0 is the offset in the tip position due to convolution, and λ is the comet decay length.

3.4.9 Tubulin dilution image analysis

Delay times, shrinkage length, and instantaneous velocity before washout were determined as previously described (Duellberg et al., 2016a), and outliers were removed using the ROUT method, with Q = 0.1% (GraphPad Prism). For instantaneous growth rate, microtubules were grown for 5–10 min in 20 µM tubulin. Instantaneous growth rate was determined by imaging microtubules at 10 FPS for 8–10 s before washout and measuring the average growth rate during this time. Representative dilution time lapse in Fig. 3.3 C was background-subtracted using an average rolling ball subtraction to visualize microtubule over time despite different background fluorescent intensities.

3.4.10 Comparison of our cap-size measurements with the predictions from the theoretical model of Bowne-Anderson et al. (2013)

A previously developed theoretical model of microtubule catastrophe using a coupled-random GTP hydrolysis mechanism found that, in the regimen of robust microtubule growth $\left(k_{off} \ll k_{on}[Tb]\right)$, the microtubule catastrophe frequency as a function of tubulin concentration may be modeled by

$$f_{cat} \approx \frac{13}{n} k_{off} \frac{h}{h + k_{on}[Tb]},$$

where n is the gamma distribution step parameter, h is the GTP-tubulin hydrolysis rate, and k_{on} and k_{off} are GTP-tubulin on- and off-rates, respectively (Bowne-Anderson et al., 2013). Using our experimentally determined tubulin on-rates (minus: 0.88 ± 0.04 μM^{-1} s^{-1}; plus: 3.34 ± 0.02 μM^{-1} s^{-1}) and off-rates (minus: 0.054 ± 0.004 s^{-1}; plus: 0.144 ± 0.006 s^{-1}) and assuming gamma step parameter $n = 2$ for both ends, the best fit of this theoretical model to our catastrophe frequency as a function of tubulin concentration data yields a hydrolysis rate $h = 0.07 \pm 0.02$ s^{-1} (maximum likelihood estimate with 95% CI) for both ends. The steady-state GTP cap size λ can be modeled as $\lambda = v_g/h$, where GTP-tubulin subunits are added to the cap with the net polymerization rate v_g and removed through the process of GTP hydrolysis with rate h, which is assumed to be independent of tubulin concentration. Under these assumptions, the hydrolysis rate of 0.07 ± 0.02 s^{-1} would correspond to the GTP cap decay size of 290 ± 80 nm for microtubules growing at 20 nm/s, in excellent agreement with both our EB-comet decay length measurements (Fig. 3.2 B) and the shrinkage length before dilution measurements (Fig. 3.3 D).

Chapter 4

Mitotic kinesins HSET and MCAK are antagonistic regulators of GTP-tubulin off-rate

Adapted from:

Strothman, C., V. Farmer, G. Arpağ, N. Rodgers, M. Podolski, S. Norris, R. Ohi, and M. Zanic. 2019. Microtubule minus-end stability is dictated by the tubulin off-rate. *J. Cell Biol.* 218:2841–2853. doi:10.1083/jcb.201905019.

4.1. Introduction

Our previous work that indicated a highly correlated role between the GTP-tubulin off-rate and frequency of catastrophe. Based on this, we were interested in investigating specific regulation of the GTP-tubulin off-rate by other microtubule-associated proteins, and whether we could show that this regulation also correlated with specific regulation of catastrophe. To address, this, we use two human mitotic kinesins, kinesin-13 MCAK and kinesin-14 HSET/KIFC1. MCAK is an extensively studied microtubule depolymerase, which indiscriminately targets and destabilizes either microtubule end (Wordeman and Mitchison, 1995; Walczak et al., 1996; Desai et al., 1999; Moores et al., 2002; Hunter et al., 2003; Helenius et al., 2006; Benoit et al., 2018). HSET is a minus-end directed kinesin identified to have a crucial role in focusing multipolar spindles in dividing cancer cells (Kwon et al., 2008; Wu et al., 2013; Pannu et al., 2015; Xiao and Yang, 2016; Fu et al., 2018). Effects of HSET on microtubule dynamics have not previously been studied; however, given its minus end-directed motor activity (Case et al., 1997; Mountain et al., 1999; Norris et al., 2018; Reinemann et al., 2018) it is a promising candidate for a minus-end specific regulator. Previous work on MCAK leads us to believe that it fits our criteria for increasing catastrophe frequency without affecting other

dynamic parameters, and that its mechanism of destabilization occurs through increasing the GTP-tubulin off-rate at microtubule ends. HSET is a member of the kinesin-14 family of minus-end directed motors, and while HSET's effect on microtubule dynamics has not previously been reported, Kar3, a *S. cerevisiae* member of the kinesin-14 family, was previously shown to act as a microtubule depolymerase (Sproul et al., 2005). We thus wondered whether the H. sapiens kinesin-14 HSET might also modulate the GTP-tubulin off-rate at microtubule ends.

4.2. Results

4.2.1. MCAK and HSET antagonistically regulate GTP-tubulin off-rate

If microtubule catastrophe, but not the microtubule growth rate, is highly sensitive to the GTP-tubulin off-rate, we expect that modulating the GTP-tubulin off-rate would have a specific effect on catastrophe frequency without affecting the mean growth rate (Bowne-Anderson et al., 2013; see Methods). To test this hypothesis, we used two human mitotic kinesin motor proteins, MCAK and HSET. MCAK is a kinesin-13 motor well known for its function as a microtubule depolymerase. MCAK has been shown to robustly depolymerize GMPCPP-stabilized microtubules *in vitro*, directly increasing the tubulin off-rate at both microtubule ends (Desai et al., 1999; Hunter et al., 2003; Helenius et al., 2006). Consistent with previous reports, we found that the addition of 10 nM MCAK resulted in rapid depolymerization of GMPCPP-microtubules at both plus (7.7± 0.2 nm s^{-1}, SE, N = 139) and minus (8.0 ± 0.3 nm s^{-1}, SE, N = 140) ends (Figure 4.1A-B).

When added to GMPCPP-stabilized microtubules, HSET molecules diffused along the microtubule lattice and accumulated at minus ends over time, consistent with previous reports

using the *Drosophila* HSET homolog, Ncd (Fink et al., 2009). However, in the presence of HSET we did not observe any discernible depolymerization at either microtubule end over the course of a 15-minute-long movie, similar to the control (Figure 4.1A-B). It has been shown that the presence of soluble tubulin induces robust minus-end directed processivity of HSET molecules (Norris et al., 2018). We thus tested whether the addition of soluble tubulin to HSET changed its ability to depolymerize microtubules, and again, we observed no depolymerization (Figure 4.2A-B). However, when we combined 10 nM GFP-HSET with 10 nM MCAK, we observed rapid depolymerization at microtubule plus ends only (Figure 4.1A-B). The addition of HSET to MCAK significantly decreased tubulin off-rate at minus ends, inducing a 7-fold reduction in the minus-end depolymerization rate when compared to the MCAK-alone condition (Figure 4.1B). In contrast, HSET only mildly suppressed the plus-end depolymerization rate (1.7-fold), possibly due to the residual localization of HSET all along the microtubule lattice. We conclude that HSET antagonizes the MCAK-induced increase in the GTP-tubulin off-rate at microtubule minus ends.

To further investigate whether HSET directly suppresses tubulin off-rate, we repeated tubulin dilution experiments using microtubules grown with 12 μM tubulin in the presence or absence of 100 nM GFP-HSET during both the growth and washout phases (Figure 4.1C). We found that HSET had no significant effect on plus-end delay times; however, we observed a significant increase in minus-end delay times in the presence of HSET (Figure 4.1D). Individual delay times correlated with the average GFP-HSET fluorescence intensity at the microtubule tip following tubulin washout (Figure 4.1E), indicating that HSET directly stabilized minus ends after washout, consistent with suppressing the GTP-cap removal. We thus conclude that, in

contrast to MCAK, HSET directly suppresses the GTP-tubulin off-rate at microtubule minus ends.

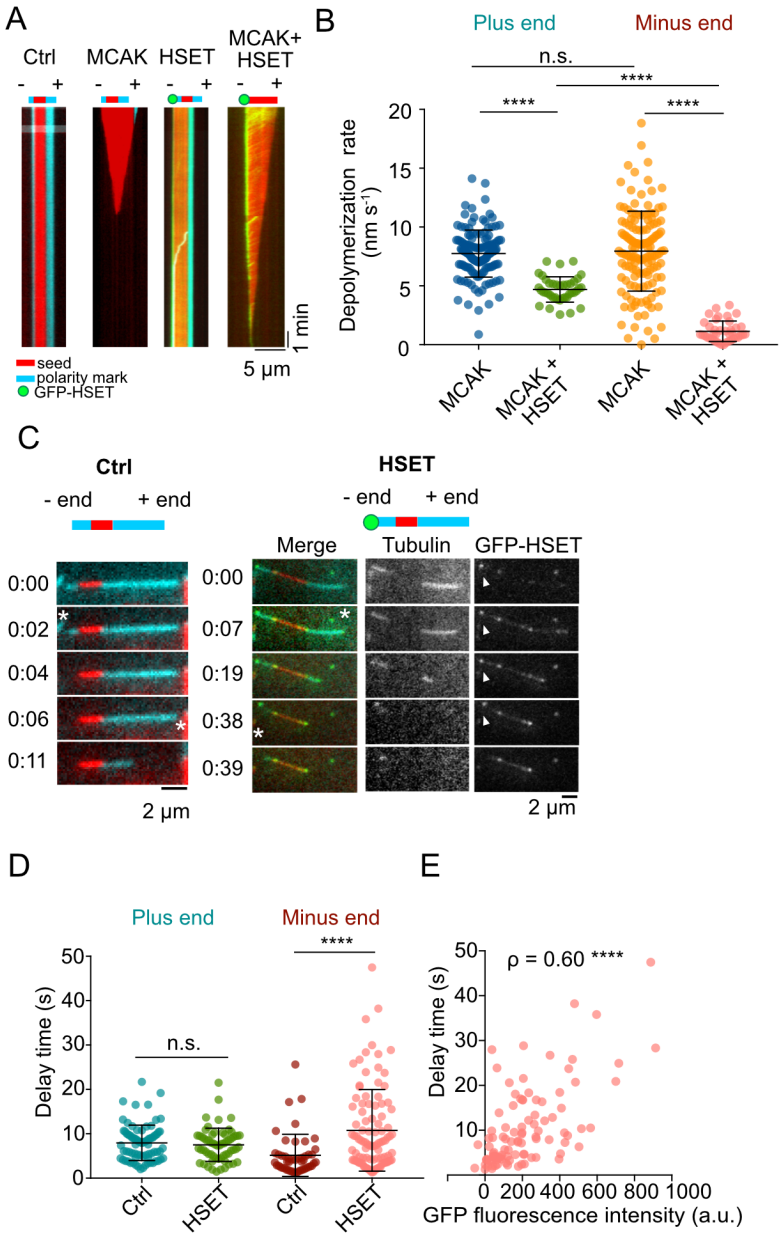

Figure 4.1. MCAK and HSET antagonistically regulate GTP-tubulin off-rate. (A) Representative kymographs of GMPCPP seeds in different conditions: Ctrl, +10 nM GFP-HSET, +10 nM MCAK, or +both 10 nM GFP-HSET and 10 nM MCAK. Seeds are polarity marked with

Alexa Fluor-647 tubulin in Ctrl, HSET, and MCAK conditions, but not with both motors. (B) GMPCPP-microtubule depolymerization rates of MCAK, and MCAK+HSET conditions at the plus and minus end. In the MCAK alone condition, plus and minus ends are differentiated by polarity mark. In the double motor condition, the ends are differentiated by HSET localization. Data represent two independent repeats of each condition. Plus end MCAK (blue): N = 139, MCAK + HSET (green) N = 40, Minus end MCAK (gold) N = 140, MCAK + HSET (pink) N = 40. Mann-Whitney U tests were performed for plus- and minus-end conditions separately. ****p-value ≤ 0.0001. (C) Representative timelapses of dilution experiments in the absence or presence of 100 nM HSET. Asterisks mark time of catastrophe at either end. Arrow in HSET condition indicates GFP-HSET tip localization. Timestamp indicates time after washout (min:s). (D) Delay times per end in the absence or presence of 100 nM HSET. N = 3 independent repeats for the control, and N = 4 independent repeats for +HSET condition. (E) Minus end + HSET delay times as a function of GFP fluorescence intensity (background subtracted, see methods). N = 97 delay times from 4 independent repeats. Spearman rho's test ρ=0.060, ****p ≤ 0.0001.

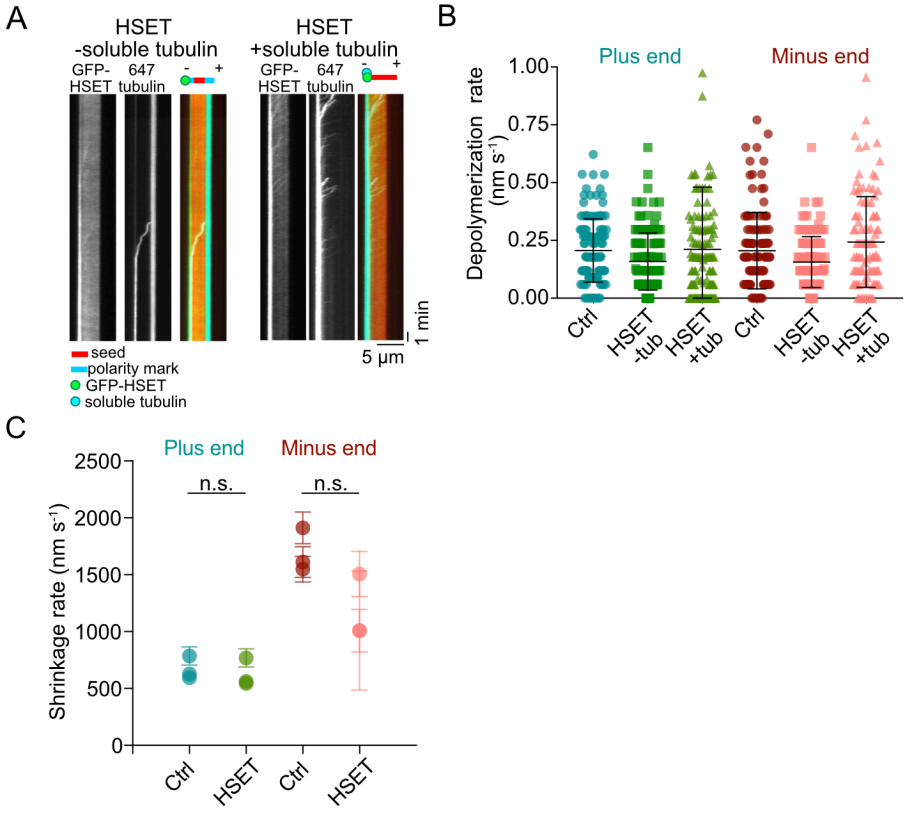

Figure 4.2. HSET does not significantly affect microtubule shrinkage rates. (A) Representative kymographs showing depolymerization of GMPCPP-microtubule seeds in the presence of 10 nM GFP-HSET, either with or without 100 nM soluble tubulin (Alexa Fluor 647

labeled) to activate its processivity. In the absence of soluble tubulin, polarity marking differentiates the two ends. In the presence of soluble tubulin, directionality of GFP-HSET differentiates the two ends. (B) Depolymerization rate of GMPCPP seeds in the absence of other proteins (control) for Fig. 4.1 (A and B), as well as rates of depolymerization of GMPCPP seeds in the presence of 10 nM GFP-HSET, either with or without 100 nM soluble tubulin. Two independent repeats per condition; n≥107 for each condition. (C) Average shrinkage rates from both microtubule ends in a dynamic assay with 10 μM tubulin, with and without 10 nM GFP-HSET. N= 3 in-dependent repeats. Plus-end control: N= 61, 88, 112; plus-end HSET: N= 77, 71, 60. Minus-end control: N= 57, 87, 87; minus-end HSET: N= 19, 18, 4. Error bars are SEM. Unpaired Welch's t-test performed for each end, n.s., P≥0.05.

4.2.2. HSET suppresses minus end catastrophe and protects minus ends against MCAK

Based on our finding that HSET suppressed tubulin off-rate, we predicted that HSET would suppress catastrophe frequency, in contrast to the well-known catastrophe-promoting activity of MCAK (Desai et al., 1999; Newton et al., 2004; Gardner et al., 2011b). To test this hypothesis, we grew dynamic microtubules with 10 μM tubulin and 10 nM GFP-HSET. In these conditions, HSET walked processively towards the minus end, where it tip-tracked growing minus ends (Figure 4.3A). Microtubule growth and shrinkage rates at both the plus and minus ends were not significantly different in the presence or absence of HSET (Figure 4.3B, Figure S3C). HSET did not significantly affect plus-end catastrophe, but strongly and specifically suppressed minus-end catastrophe (Figure 4.3C). In contrast, MCAK significantly increased catastrophe at both plus and minus ends (Figure 4.3F) without affecting the growth rate at either end (Figure 4.3E), consistent with previous reports at the plus end alone (Montenegro Gouveia et al., 2010; Gardner et al., 2011b). When HSET and MCAK were combined, we observed significant suppression of catastrophe specifically at the minus end (Figure 4.3F). These findings directly correlate the effects of each of the motors on the GTP-tubulin off-rate with their specific and antagonistic modulation of microtubule catastrophe.

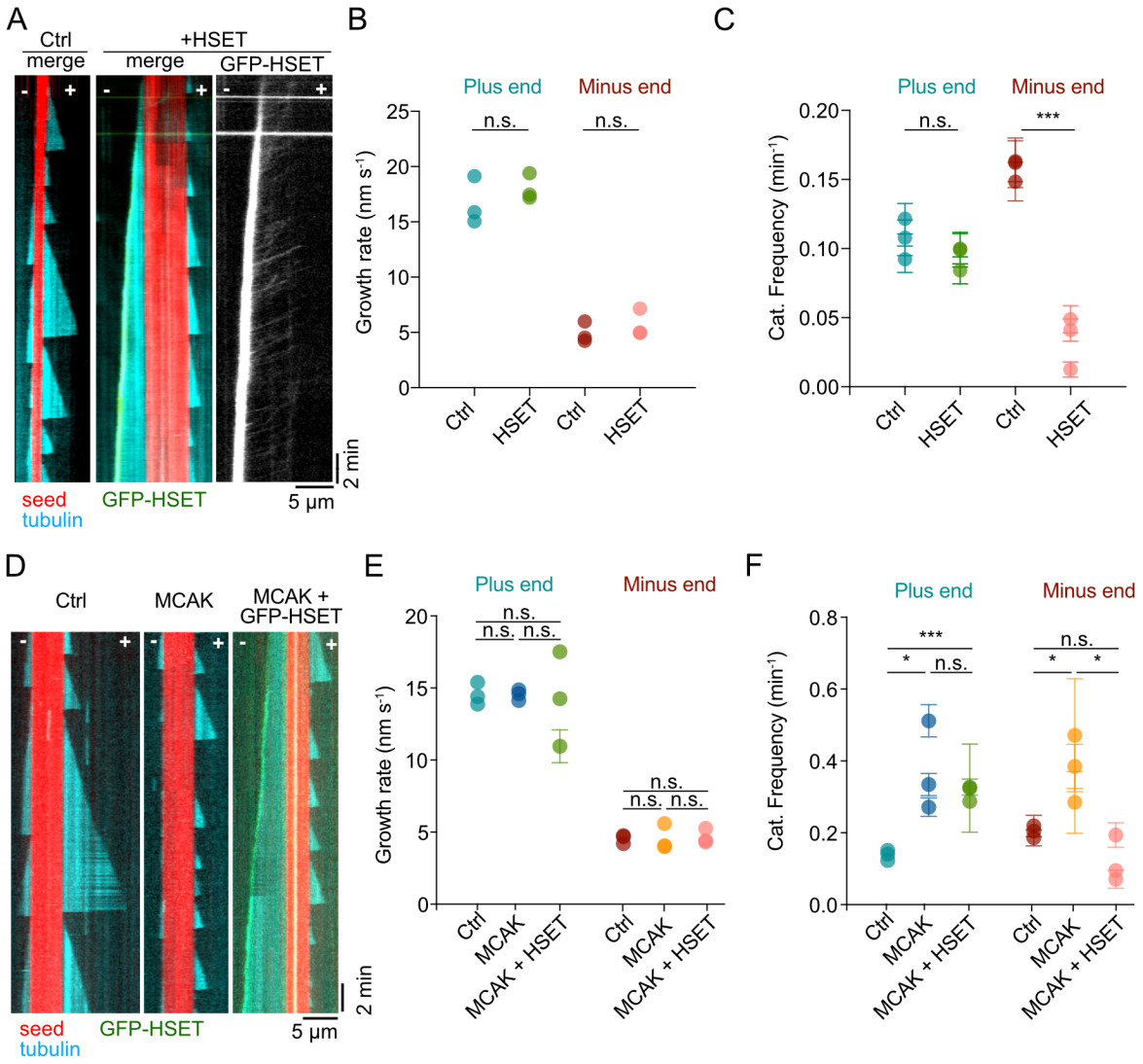

Figure 4.3. HSET suppresses minus end catastrophe and protects minus ends against MCAK. (A) Representative kymographs from movies comparing dynamics of microtubules grown in 10 µM tubulin with and without 10 nM GFP-HSET. (B) Average growth rates of plus and minus ends with and without HSET. N = 3 independent repeats per condition. Plus end ctrl N = 176, 258, 123; Plus end HSET N = 235, 276, 157. Minus end ctrl N= 93, 97, 24; Minus end HSET N =88, 120, 59. Error bars are SEM. (C) Catastrophe frequency of plus and minus ends. Plus end ctrl N = 155, 232, 121; Plus end HSET N=224, 242, 153. Minus end ctrl N=85, 92, 23; Minus end HSET N =67, 37,13. Error bars represent counting error. (D) Representative kymographs of microtubules grown in 10 µM tubulin, 10 µM tubulin with 10 nM MCAK, and 10 µM tubulin with 10 nM of both MCAK and GFP-HSET. (E) Average growth rates of dynamic plus and minus ends in a ctrl, with MCAK, and with both MCAK + HSET. Plus end Ctrl: N= 88, 200, 79; Plus end MCAK: N=132, 132, 125; Plus end MCAK + HSET: N= 235, 8, 249. Minus end Ctrl: N= 74, 118, 56; Minus end MCAK: N= 12, 9, 41. Minus end MCAK + HSET:

N= 29, 13, 34. (F) Catastrophe frequency of plus and minus ends in a ctrl, with MCAK, and with both MCAK + HSET. Plus end Ctrl: N = 66, 154, 63; Plus end MCAK: N =113, 129, 118; Plus end MCAK + HSET: N = 216, 7, 220. Minus end Ctrl: N = 11, 9, 39; Minus end MCAK: N = 11, 9, 39. Minus end MCAK + HSET: N = 24, 8, 32. Error bars represent counting error. Multiple unpaired t-tests performed for all plus and minus end conditions. N.s. p-value ≥ 0.05, *p-value ≤ 0.05, ***p-value ≤0.001, ****p-value ≤0.0001.

4.3. Discussion

A number of kinesin motors have been identified as regulators of microtubule dynamics; our results have added human kinesin-14 HSET to this list. Unlike kinesin-13 MCAK, which does not discriminate between the two ends, HSET's regulatory activity is restricted to the minus end, since its directionality strongly enhances its localization to growing minus-end tips. Both MCAK and HSET have a specific effect on microtubule catastrophe, without changing the microtubule growth or shrinkage rates (Newton et al., 2004; Montenegro Gouveia et al., 2010), consistent with the idea that they are regulating GTP-off rate, which is predicted to primarily affect catastrophe, and not growth or shrinkage. Specific regulation of minus-end catastrophe by HSET is in stark contrast with the effects of other known minus-end regulators. For example, proteins from the CAMSAP family of minus-end regulators exert simultaneous effects on several dynamics parameters: while they suppress catastrophe, they also slow minus-end growth, suggesting a distinct mechanism from that of HSET (Hendershott and Vale, 2014; Jiang et al., 2014).

Overall, our finding that MCAK and HSET target the same kinetic rate, but regulate it antagonistically, suggests a general mechanism for specific regulation of microtubule catastrophe. MCAK and HSET are both mitotically-active kinesins, and perturbations of either result in large-scale disruptions in spindle length and morphology (Ohi et al., 2007; Cai et al.,

2009; Domnitz et al., 2012). Though HSET has previously been shown to be a force balance factor in the spindle (Mountain et al., 1999; Cai et al., 2009; Hentrich and Surrey, 2010; Reinemann et al., 2018), as well as a kinesin involved in pole-focusing and spindle organization (Hepperla et al., 2014; Cai et al., 2009), its role in regulating minus-end dynamics within the spindle, and potentially counterbalancing MCAK, has not yet been studied. We hope that our study will inspire development of more refined, wholistic models encompassing the dynamics of both microtubule ends, and lead to future studies in cells uncovering how regulation of both microtubule ends is integrated to give rise to the dynamic cellular microtubule architecture.

4.4. Methods

4.4.1 Protein Purification

Tubulin was purified and labeled as previously described in Chapter 2. His6-HSET tagged with enhanced GFP was expressed in *Spodoptera frugiperda* (Sf9 cells) and purified as previously described (Norris et al., 2018) and stored in 10 mM K-HEPES, pH 7.7, 300 mM KCl, 1 mM dithiothreitol, 100 µM $MgCl_2$, 100 µM ATP, and 20% sucrose. Human MCAK-His6 was expressed in Sf9 cells and purified as previously described (Helenius et al., 2006) and stored in BRB20 (20 mM Pipes/KOH, pH 6.8, 1 mM $MgCl_2$, and 1 mM EGTA). Protein concentration was determined using absorbance at λ =280 nm or a Bradford assay (Kielkopf et al., 2020).

4.4.2 GMPCPP seed depolymerization with MCAK and HSET

GMPCPP seed depolymerization assays were performed similarly to the experiments described in Chapter 3. TMR-labeled seeds were prepared and bound to the chamber coverglass.

Polarity marking was used in control, HSET, and MCAK conditions: 0.5 μM 7% Alexa Fluor 647 tubulin with 1 mM GMPCPP was flown into the chamber and let polymerize for 15 min before the experiment. After 15 min, this mixture was washed out and replaced with imaging buffer containing BRB80, 10 nM GFP-HSET, 10 nM MCAK, or both motors in a reaction mix with anti-fade lacking guanosine nucleotides but supplemented with 1 mM ATP. Soluble tubulin was not present in the reaction mix unless indicated. To test the effect of tubulin activation, the HSET condition was repeated in the absence of polarity marking, but in the presence of 100 nM 7% Alexa Fluor 647 tubulin. Images were taken every 3 s for 15 min on the EM-CCD camera. When polarity marks were absent (i.e., in the presence of GFP-HSET), HSET minus-end directionality and localization were used to differentiate the microtubule ends. Outliers were removed using the ROUT method (robust regression and outlier removal; GraphPad Prism), with Q = 0.1%.

4.4.3 Dilution experiments

Microfluidic devices were prepared as described in Chapter 3, and experiments and analysis were performed similarly, with the following differences. Dilution experiments containing HSET had 100 nM GFP-HSET present in both the growth and washout phases, supplemented with 100 nM unlabeled tubulin during the washout, and 1mM ATP in all solutions. Experiments comparing the effect of HSET were done at 6.7 FPS (640- and 488-nm channels) using the EM-CCD camera (160-nm pixel). Fluorescence intensity of GFP-HSET was determined by drawing a linescan over the kymograph of the microtubule tip following washout and taking the mean intensity measurement. Background was subtracted by taking the mean intensity of a small rectangular area (3-pixel width × length of linescan) in the solution area

adjacent to each microtubule tip, so that each individual event had its own background subtraction to account for uneven illumination in the TIRF field of view. Corresponding delay times were plotted as a function of GFP-HSET tip intensity during washout.

4.4.4 Dynamics assays

Dynamics assays were performed as previously described in Chapter 2 with the following alterations. Reactions containing HSET and/or MCAK were additionally supplemented with 1 mM ATP. MCAK was stored and diluted in BRB20 and control experiments contained an equivalent volume of BRB20 to MCAK conditions. GFP-HSET was diluted in BRB80, and control conditions contained an equivalent volume of HSET storage buffer (10 mM K-HEPES, pH 7.7, 300 mM KCl, 1 mM dithiothreitol, 100 µM $MgCl_2$, 100 µM ATP, and 20% sucrose). Dynamics experiments with motors used 10 µM tubulin, 7% labeled with Alexa Fluor 647 dye. For the HSET-alone dynamics series, the representative kymographs come from movies imaged at 0.2 FPS for 30 min, but careful measurements of growth rate, shrinkage rate, and catastrophe frequency for this series come from movies taken at 1 FPS for 30 min.

CHAPTER 5

Characterization of the interaction of HSET with tubulin and EB1

5.1. Introduction

Many previous studies have implicated HSET/KIFC1 as a factor involved in microtubule organization during mitosis, particularly in focusing spindle poles in cells with an atypical number of centrosomes (Kwon et al., 2008; She and Yang, 2017; Kleylein-Sohn et al., 2012; Chavali et al., 2016; Pannu et al., 2015). However, there are many unknown aspects regarding the molecular mechanisms of HSET in its physiological role during mitosis. HSET contains two distinct microtubule binding domains: one in the C-terminal motor, and another in the N-terminal tail (Figure 1.4) (Norris et al., 2018). HSET as a single motor is not processive along microtubules; however, when it assembles into multi-motor clusters, it can walk processively towards minus ends (Norris et al., 2018). While a single-molecule perspective may define processivity as the ability to take several consecutive steps in one direction, here, we refer to processivity as a more robust parameter in which a motor shows directed motility on a longer scale (hundreds of nanometers to microns in length), easily detectable by light microscopy. Our recent work has shown that these multi-motor HSET clusters scaffold onto soluble tubulin (Norris et al., 2018). The composition of HSET-tubulin clusters is quite heterogeneous, but on average, a single cluster contains approximately 3-4 motors on 12 tubulin dimers (Norris et al., 2018). At least two motors are needed in a cluster to enable processive walking behavior (Norris et al., 2018). Interestingly, processivity of HSET can be reconstituted with different synthetic scaffolds replacing tubulin, such as a quantum dot (Norris et al., 2018). When full-length HSET motors are stably bound to quantum dots in a 3:1 ratio, they show minus-end directed

processivity similar to their more physiological tubulin-scaffolded counterparts (Norris et al., 2018). HSET can also be toggled to exhibit different modes of microtubule organization. As an individual motor, HSET can bundle microtubules- when these microtubules are parallel, the motor is locked; however, when the microtubules are antiparallel, HSET may slide them apart, as it walks towards the two respective minus ends (Mountain et al., 1999; Hepperla et al., 2014; Hentrich and Surrey, 2010; Reinemann et al., 2018; Norris et al., 2018). When HSET is arranged onto soluble tubulin, bound through its secondary microtubule binding domain (MTBD) in the tail (Figure 1.4), it can self-organize microtubules into more complex three-dimensional microtubule organizations, like microtubule asters (Norris et al., 2018). While this recent work has uncovered some crucial aspects characterizing the composition and function of HSET-tubulin clusters, many questions about the nature of these clusters remain. It is not known whether the tubulin in these clusters comes from pre-existing oligomers of soluble tubulin, or whether HSET is able to actively cluster several dimers together into a scaffold. It is also not known whether this scaffolding tubulin is exchangeable and exhibits turnover whilst being utilized by multiple HSET motors.

Another feature of the tail region of HSET is the EB-binding SxIP motif, of which there has been some preliminary studies, but again, many interesting questions remain. Braun et al. (2013) showed that this putative SxIP motif of HSET does indeed bind EB1, and either mutation of this site in HSET or deletion of the C-terminal tail of EB1 abolishes the interaction (Braun et al., 2013). In the specific *in vitro* conditions in this work, HSET was non-processive on microtubules, despite the presence of soluble tubulin, possibly due to large differences in buffer composition, likely altering the ionic strength of the solution and potentially disrupting electrostatic interactions. In these conditions, however, EB1 was also reported to recruit HSET to

growing plus-end tips through the specific interaction of the two proteins. It was not investigated whether once localized to plus ends, HSET was capable of regulating dynamics. We were interested in expanding these experiments to examine the interaction of HSET and EB1 in conditions where HSET is able to be processive, to see the interplay of HSET and EB1 binding and redistribution along the microtubule, as well as the potential effects on dynamics from strongly re-localizing either protein.

5.2. Results

5.2.1. HSET assembles onto pre-existing soluble tubulin oligomers

In order to differentiate between two main possibilities of HSET-tubulin cluster formation: (a) through assembly on pre-existing tubulin oligomers, or (b) active clustering of individual tubulin dimers, we used an *in vitro* reconstitution approach with HSET on stabilized GMPCPP microtubules and purified tubulin labeled with two different fluorescent dyes: Alexa Fluor-488 or Alexa Fluor-647. We flowed in a reaction mix containing HSET and equimolar amounts of Alexa Fluor-488 tubulin and Alexa Fluor-647 tubulin directly onto stabilized rhodamine-labeled GMPCPP microtubule seeds attached to a coverslip and imaged using TIRF microscopy. We hypothesized that distinguishing single-color versus two-color tubulin tracks and quantifying the proportions of each would elucidate whether HSET (a) predominantly binds pre-existing tubulin oligomers from a given tubulin solution (mostly single-color tubulin-tracks) or (b) actively and indiscriminately clusters individual dimers from multiple tubulin solutions (significant proportion of two-color tubulin tracks). Figure 5.1A shows representative examples of how the tubulin tracks are categorized as either single-color or two-color. A total of 2,473 tubulin tracks were analyzed from five experimental repeats, and approximately 98% of these

tracks were categorized as single-color, and 2% were two-color tracks (Figure 5.1C). There were about three times as many 488-labeled tracks as 647-labeled tracks, but this was due to a difference in the percentage labeling (488-tubulin was 100% labeled, whereas 647-tubulin was 46% labeled) (Figure 5.1B). In this experimental set-up, HSET and tubulin were combined on ice, and immediately added to the flow cell for imaging. We also tested different incubation times and temperatures (i.e., 5 minutes versus 30 minutes incubation time; and incubation on ice (0°C) versus at room temperature (25°C) and did not observe significant differences in the proportion of two-color tracks (data not shown). From this, we conclude that the predominant mechanism of HSET's assembly onto soluble tubulin scaffolding is through recognition and binding of pre-existing tubulin oligomers, and that there does not appear to be any observable rapid turnover of tubulin within these clusters in this assay.

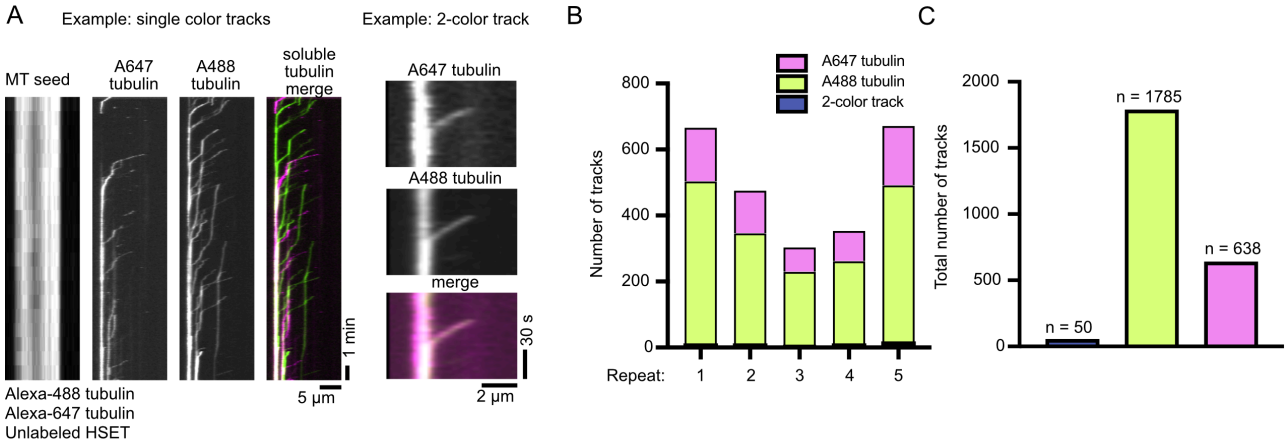

Figure 5.1 HSET-tubulin clusters are predominantly composed of pre-existing tubulin oligomers from a single tubulin source. (A) Representative kymographs showing single-color tubulin tracks, or 2-color tubulin tracks. Minus ends are oriented to the left, and plus ends to the right. 10nM HSET was incubated with 50nM of 647-tubulin (46% labeled) and 50nM of 488-tubulin (100% labeled). (B) Categorization of tracks from 5 individual experimental repeats as single color (either 647- or 488- labeled tubulin) or as 2-color track. Total counts of each track per repeat are shown. (C) Combined data showing the total counts of tracks from each of the three categories across all experimental repeats.

5.2.2. HSET localizes EB1 to dynamic minus-ends, where HSET has the dominant regulatory effect on dynamics

We were interested in repeating experiments combining EB1 and HSET in a dynamic assay, similar to those done in Braun et al. (2013), but in conditions where HSET also has motile properties. This would allow us to assess the localization of EB1 and HSET not just when EB is actively recognizing plus ends, but when HSET is also actively walking towards and localizing to minus ends. Consistent with previous results, we see that EB1 in these conditions slightly increases growth rate at both ends as well as catastrophe frequency (Figure 5.2). On its own, HSET processively walks to minus ends and strongly suppresses minus-end catastrophe without affecting plus-end dynamics (Figure 5.2). When EB1 and HSET are combined in these conditions, we observe EB1 co-localizing to the tracks of tubulin present in the HSET-tubulin clusters, indicating that HSET-tubulin clusters are also transporting EB1 to minus ends, where EB1 also shows a strong localization signal (Figure 5.2). Combined with the previous studies, this result indicates that in conditions where HSET is non-motile, EB1 may easily recruit HSET to plus-end tips; however, when HSET is motile, it can reciprocally recruit EB1 to minus ends. Interestingly, the analysis of the dynamics across these experimental conditions shows that individually, EB1 and HSET exert somewhat antagonistic effects on minus-end dynamics in terms of catastrophe; however, when the two proteins are combined, HSET dominates the dynamic regulation of minus ends, by significantly suppressing catastrophe similar to the effect of HSET alone.

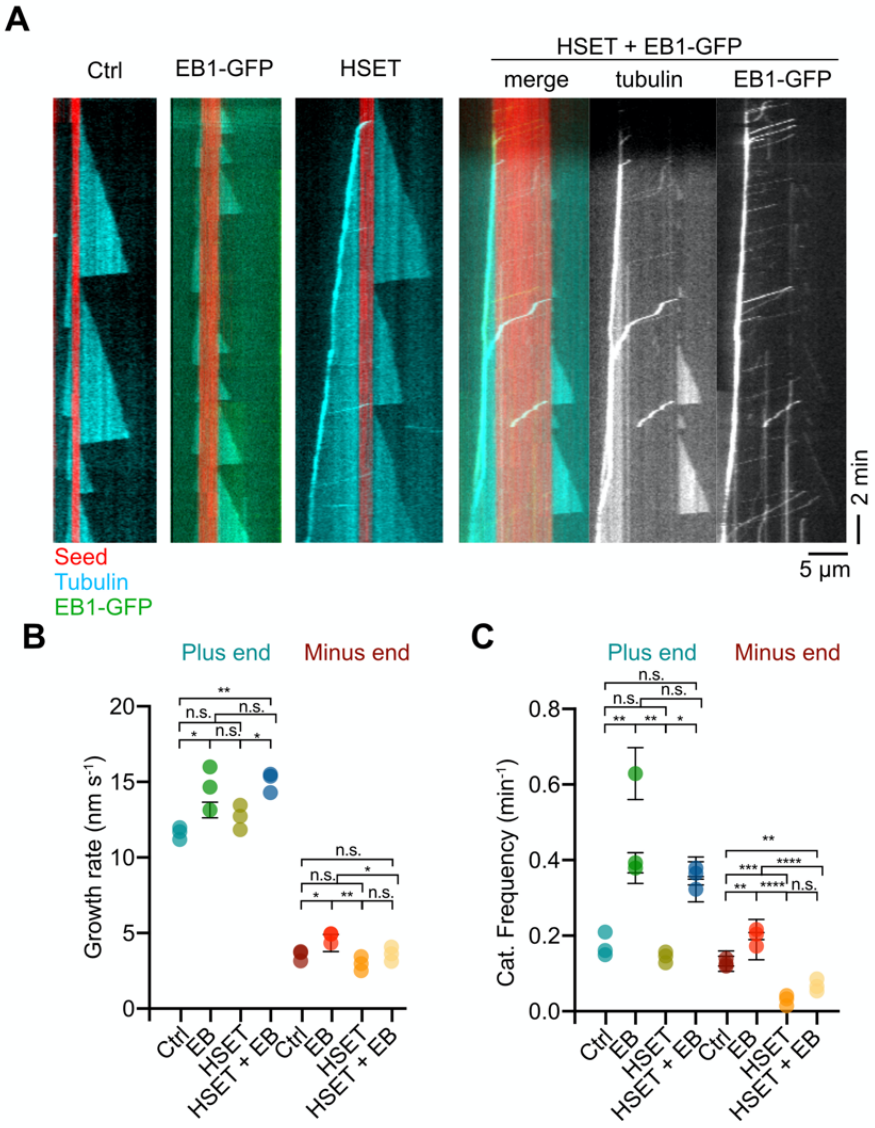

Figure 5.2. HSET recruits EB to dynamic minus ends, where HSET still has the dominant regulatory effect. (A) Representative kymographs from movies comparing localization and dynamics with HSET and EB1-GFP individually or combined. 12 µM tubulin, 200 nM EB1, and 10 nM HSET were used. Three experimental repeats were done for each condition. Minus ends are oriented to the left, and plus ends to the right. (B) Average growth rates of plus and minus ends from each condition. Plus end ctrl N = 82, 197, 122; plus end EB N = 84, 233, 96; plus end HSET N = 69, 157, 129; plus end both N = 100, 177, 155. Minus end ctrl N = 48, 90, 53; minus end EB N = 25, 124, 69; minus end HSET N = 16, 82, 43; minus end both N = 43, 72, 65. Error bars are S.E.M. One-way Anova was performed for statistical analysis for plus and minus end groups separately. (C) Frequency of catastrophe from each condition. Plus end ctrl N = 72, 171, 104; plus end EB N = 84, 216, 86; plus end HSET N = 55, 134, 109; plus end both N = 93, 165, 141. Minus end ctrl N = 38, 72, 48; minus end EB N = 23, 109, 64; minus end HSET N = 5, 51,

22; minus end both N = 29, 55, 41. Error bars represent counting error. One-way Anova was performed for statistical analysis for plus and minus end groups separately. N.s. p-value ≥ 0.05, *p-value ≤ 0.05, ***p-value ≤0.001, ****p-value ≤0.0001.

5.2.3. In fast microtubule growth conditions, EB1 localizes HSET to plus ends, where EB1 has the predominant regulatory effect

In the previous dynamic conditions, both microtubule ends were growing relatively slowly compared to physiological microtubule growth rates, in which EB1 tip localization is robust. EB1 recognizes the nucleotide state of the GTP cap at the end of growing microtubules, so, the larger the GTP cap is, the more binding sites are available for EB1 (Zanic et al., 2009; Maurer et al., 2012; Seetapun et al., 2012; Zhang et al., 2015; Bieling et al., 2007). The most straightforward way to increase the size of the GTP cap, and therefore the region of EB1 localization, is to increase the microtubule growth rate (Bieling et al., 2007). We were interested in creating dynamic conditions in which growth rates were higher and therefore EB1 localization at plus ends was more robust than in the previous assays, to see whether we could better observe EB1 recruiting HSET to plus ends, as has been previously reported (Braun et al., 2013). To achieve high growth rates, but short non-overlapping microtubule extensions that we could easily track and analyze in a given field of view, we added the well-characterized microtubule polymerase XMAP215 (Gard and Kirschner, 1987; Brouhard et al., 2008). XMAP215 increases growth rate and catastrophe frequency at microtubule plus ends, and synergizes with the similar regulatory effects of EB1 to result in microtubule dynamics with fast-growing short extensions with larger GTP-cap regions (Zanic et al., 2013). When we combine EB1 and XMAP215 in this dynamic assay, in the absence of HSET, we indeed see this dynamic profile consistent with previous studies (Zanic et al., 2013). When HSET is added, we observe localization of GFP-

HSET to growing plus-end tips, similar to the localization profile of EB1 (Figure 5.3). HSET is still motile in these conditions, and we still see minus-end directed motility of HSET in these conditions. Quantification of the dynamics revealed that HSET did not appear to have a stabilizing effect at the plus ends, where it was localized by EB1. Rather the dominant effect on dynamics was exerted by EB1 in synergy with XMAP215 (Figure 5.3). As a control, we repeated these experiments with an EB1ΔC construct, in which the region of EB1 that recognizes the SxIP motif in HSET is missing, thereby abolishing the specific interaction between HSET and EB1. When XMAP215, HSET and EB1ΔC were combined, HSET no longer showed plus-end localization, indicating that this localization was indeed a result of a specific interaction with EB1, as previously reported (Figure 5.4). Altogether, these results indicate that HSET and EB1 can reciprocally recruit each other to the plus or minus ends, where the recruiter protein will retain the dominant regulatory effect on dynamics, with no clear impact of the recruited protein, despite being highly concentrated near dynamic microtubule tips.

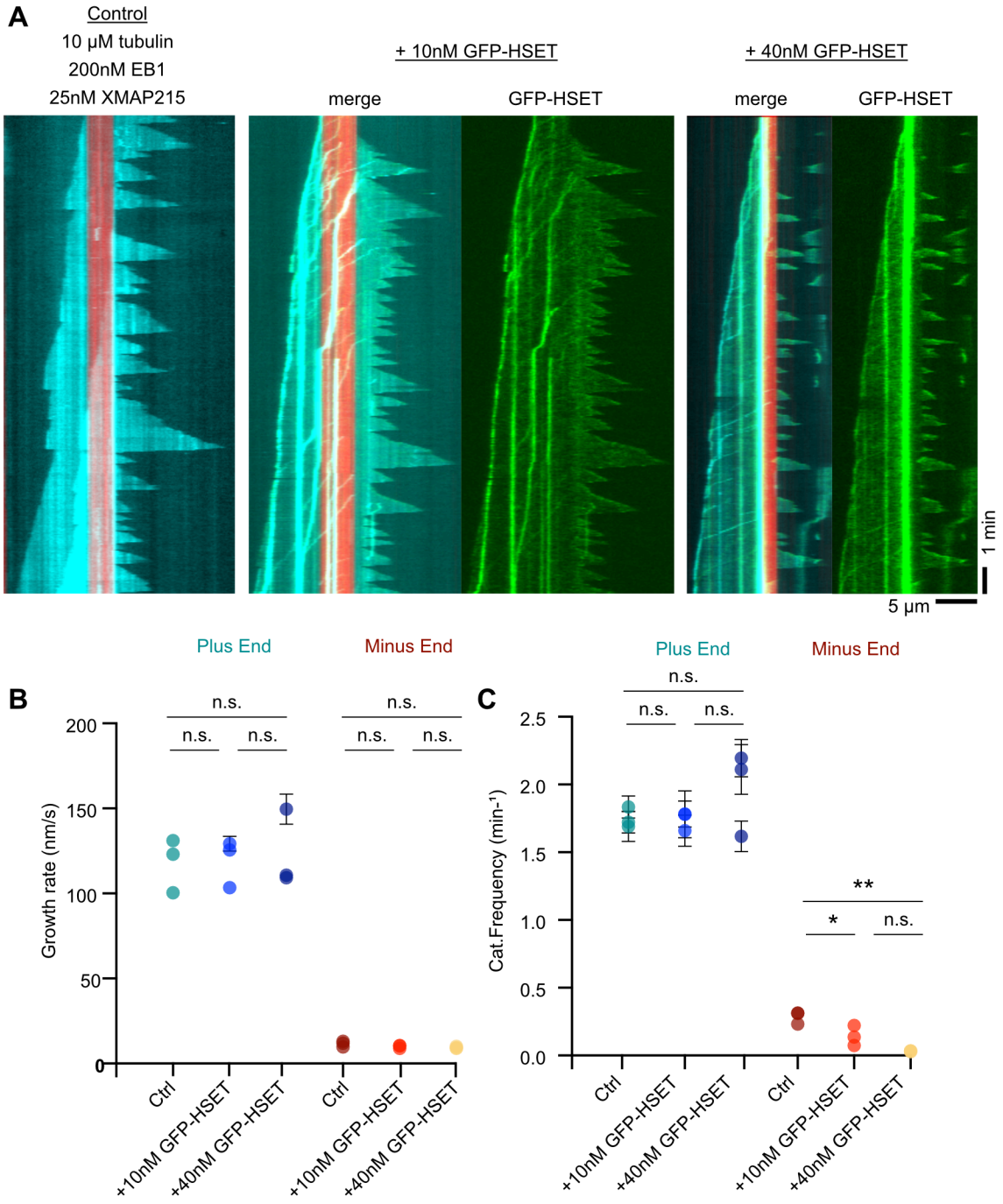

Figure 5.3. EB localizes HSET to plus ends, where it does not significantly impact dynamics. (A) Representative kymographs from movies comparing localization and dynamics with HSET and EB1-GFP individually or combined. 10 µM tubulin, 200 nM EB1, and 25 nM XMAP215 were used, with either 0, 10nM, or 40nM GFP-HSET, as indicated. Three

experimental repeats were done for each condition. Minus ends are oriented to the left, and plus ends to the right. (B) Average growth rates of plus and minus ends from each condition. Plus end ctrl N = 234, 471, 509; plus end +10nM HSET N = 108, 211, 348; plus end +40nM HSET N = 134, 260, 216. Minus end ctrl N = 166, 289, 219; minus end +10nM HSET N = 26, 169, 93; minus end +40nM HSET N = 23, 55, 49. Error bars are S.E.M. One-way Anova was performed for statistical analysis for plus and minus end groups separately with multiple comparisons. (C) Frequency of catastrophe from each condition. Plus end ctrl N = 227, 462, 497; plus end +10nM HSET N = 105, 206, 338; plus end +40nM HSET N = 131, 257, 209. Minus end ctrl N = 142, 253, 184; minus end +10nM HSET N = 15, 138, 68; minus end +40nM HSET N = 7, 18, 15. Error bars represent counting error. One-way Anova was performed for statistical analysis for plus and minus end groups separately with multiple comparisons. N.s. p-value ≥ 0.05, *p-value ≤ 0.05, **p-value≤0.01.

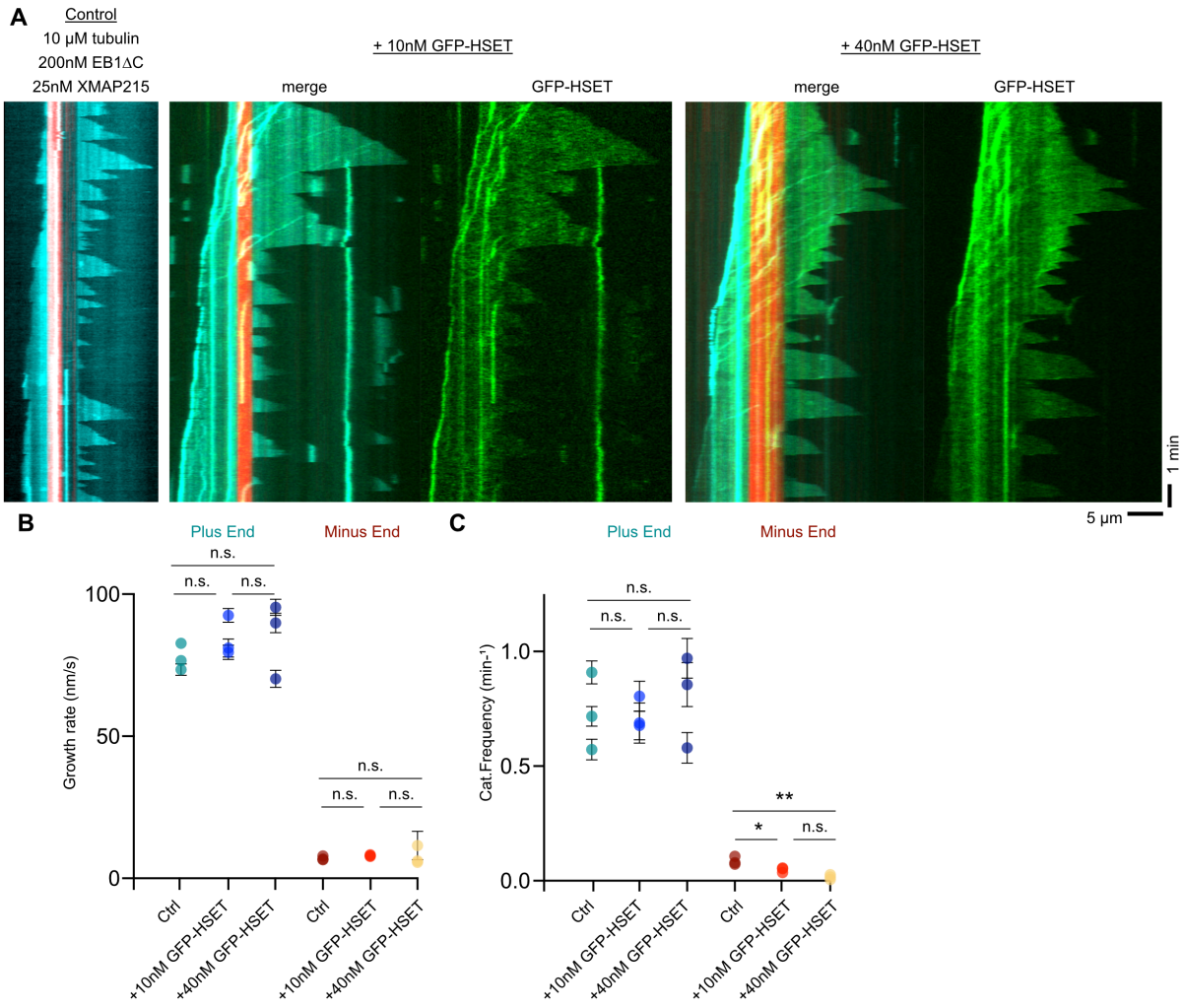

Figure 5.4. EB1ΔC does not localize HSET to plus ends. (A) Representative kymographs from movies comparing localization and dynamics with HSET and EB1-GFP individually or

combined. 10 μM tubulin, 200 nM EB1ΔC, and 25 nM XMAP215 were used, with either 0, 10 nM, or 40 nM GFP-HSET, as indicated. Three experimental repeats were done for each condition. (B) Average growth rates of plus and minus ends from each condition. Plus end ctrl N = 353, 308, 176; plus end +10nM HSET N = 67, 160, 130; plus end +40nM HSET N = 137, 86, 82. Minus end ctrl N = 110, 96, 60; minus end +10nM HSET N = 30, 37, 60; minus end +40nM HSET N = 32, 20, 11. Error bars are S.E.M. One-way Anova was performed for statistical analysis for plus and minus end groups separately. (C) Frequency of catastrophe from each condition. Plus end ctrl N = 329, 276, 162; plus end +10nM HSET N = 61, 147, 118; plus end +40nM HSET N = 123, 79, 74. Minus end ctrl N = 71, 52, 35; minus end +10nM HSET N = 14, 14, 26; minus end +40nM HSET N = 2, 4, 3. Error bars represent counting error. One-way Anova was performed for statistical analysis for plus and minus end groups separately. N.s. p-value ≥ 0.05, *p-value ≤ 0.05, **p-value ≤0.01.

5.3 Discussion

Our findings with HSET provide further insight into its molecular mechanisms, especially regarding its cluster formation with tubulin, but many questions remain. Our results with HSET assembly onto soluble tubulin labeled with two different fluorescent dyes suggest that HSET preferentially binds to an existing oligomeric species of tubulin from a given tubulin stock, and that the tubulin in these clusters does not appear to exhibit rapid turnover as well. Norris et al. showed that the HSET-tubulin cluster formation was still able to occur in conditions that do not support active microtubule polymerization (such as colchicine or GDP), suggesting that these tubulin oligomers do not form through a polymerization process (Norris et al., 2018). This tendency of HSET to bind to pre-existing oligomers in solution rather than individual dimers of soluble tubulin may add an additional level of regulation of the action of HSET through the relative availability of these oligomers.

Tubulin oligomers may arise as by-products of microtubule depolymerization, as well as structural precursors to microtubule nucleation (Mandelkow et al., 1991; Ayukawa et al., 2021)). Tubulin oligomers are heterogeneous in nature, as are HSET-tubulin clusters themselves

(Ayukawa et al., 2021; Norris et al., 2018). Our work indicates that HSET is recognizing a very particular and very small fraction of the soluble tubulin population, which was undetectable by such methods as analytical ultracentrifugation (Norris et al., 2018). However, we do not know the mechanism by which HSET recognizes and binds to tubulin oligomers, and what the structural geometry of HSET-tubulin clusters resembles. This will be an interesting future direction to explore to further characterize the mechanism of HSET.

That HSET binds soluble tubulin may also be a mechanism for the cell to regulate the availability of HSET-tubulin clusters- evidence for this potential mechanism comes from the observation that mitotic cells whose microtubules were depolymerized by treatment with the microtubule destabilizing drug nocodazole exhibited HSET-driven aster formation, due to the increased levels of soluble tubulin (Norris et al., 2018). Therefore, the availability of soluble tubulin may help dictate whether HSET plays a role in bundling microtubules as individual motors or forming asters and potentially regulating minus-end dynamics when it forms into multi-motor clusters. This is one of many examples of the concept of the tubulin economy, in which the levels of soluble tubulin within the cell regulate a number of processes, including protein localization, autoregulation of tubulin translation, and with HSET, microtubule architectures (Ohi et al., 2021).

While it is speculated that HSET's positively charged microtubule binding domain in the tail is generally the same region that can bind either polymeric or soluble tubulin, it is unclear whether HSET employs precisely the same binding mechanism for both modes of tubulin. It will be interesting for future studies to disentangle any potential differences in the HSET tail region binding soluble versus polymer tubulin that may be involved in regulating the toggle between HSET's individual and multi-motor functions.

This may also be especially useful in thinking about the geometry of binding of HSET-tubulin clusters that are tip-tracking on growing minus-end tips. In our many experiments involving HSET at dynamic (or even non-dynamic) minus-end tips, we can see high fluorescence intensities of both HSET and tubulin at the growing minus-end tip, which often tend to increase in intensity over time (Figure 4.3A, for example). This suggests that the HSET-tubulin clusters do not disassemble once they reach the distal minus-end tip and move along with the tip as it continues to grow. We do not know how many HSET-tubulin clusters may on average be located at the minus end during a dynamics assay, or what the minimal number of clusters needed to suppress catastrophe is. In the case where other microtubule-associated proteins are present, HSET tends to dominate the dynamic regulation of minus ends, such as in the presence of MCAK or EB1, which both promote catastrophe (Figure 4.3, Figure 5.2). It is not clear to what degree HSET is able to sterically hinder MCAK or EB1, and if this is the primary mechanism by which HSET stabilizes minus ends despite the presence of these catastrophe-promoting MAPs. Alternatively, if MCAK or EB1 is able to concurrently bind to the microtubule tips and are not sterically hindered by HSET-tubulin clusters, then HSET is still potent enough to counter the effects of these proteins and maintain the stabilization of minus ends.

While there is no evidence that MCAK and HSET are capable of direct interaction, EB1 and HSET have been shown to directly bind to each other, adding another layer of complexity to their combined effects on microtubule dynamics (Braun et al., 2013). In our results showing that HSET recruits EB1 to minus ends, EB1 is seen in the processive motor tracks crossing along the length of the microtubule, similar to that of tubulin. This raises some interesting questions as to what the configuration of these multi-motor complexes are: Are there clusters containing HSET and EB1 that lack tubulin, or is tubulin needed as a clustering scaffold? If not, does EB1 replace

tubulin as a clustering scaffold, and how so? If both tubulin and EB are present in the clusters, then what is the geometry - can one HSET tail simultaneously bind tubulin and EB1? Further, when these clusters are tip-tracking at the minus end, is EB1 able to independently bind the minus-end tip, or is it sterically hindered from doing so, by its configuration in the cluster with HSET? Future studies will be needed to differentiate between these possibilities.

Our results additionally showed the reciprocal recruitment of HSET and EB1 to microtubule tips, and the fine balance of this recruitment. In conditions where microtubule growth was slow, HSET was able to be highly active and recruit EB to minus-end tips, where HSET retained the dominating stabilizing influence on dynamics. However, in conditions where microtubule growth was faster, EB showed clearer recruitment of HSET to plus-end tips, where there was no indication of stabilization by HSET. The mechanism of HSET's stabilization of minus ends is unknown, in terms of which structural feature is necessary and sufficient for this role. Broadly, is it the motor domain, the tail domain, or some feature of the tubulin scaffold? Though HSET was localized by EB to growing plus-end tips, it is not clear whether HSET was in fact also directly binding the microtubule tip, or whether it was sterically hindered by EB1's binding to the tip. These experiments raise some questions as to whether HSET would theoretically be capable of regulating plus-end dynamics, if it were localized there. This could be tested experimentally by inversing the motor and tail domains, or by producing a chimeric kinesin with the tail of HSET and the motor of a canonical plus-end directed motor, such as Eg5, but these studies would depend crucially on better understanding HSET's inherent mechanisms at the minus end so that experiments could be well-informed in their design. Future studies could utilize these ideas to help elucidate the structural mechanism of HSET in its regulation of microtubule dynamics.

Finally, the ability of HSET and EB1 to directly interact begs the question of overall physiological relevance of such an interaction. In mitosis, EB1 localizes to spindle poles (among other locations) (Almada et al., 2017; Chan et al., 2005), thus could binding to HSET provide a mechanism of its spindle pole localization? If EB1 and HSET's reciprocal recruitment to the microtubule tips is not due to the need for regulation of dynamics, why might it be advantageous for HSET to be deposited at plus ends, and EB1 at minus ends? For EB1, it is possible that it may recruit other binding partner MAPs to the spindle poles, where there are a number of regulators involved in the nucleation, organization, and flux of the spindle. For HSET, perhaps recruitment to the plus end of the microtubule helps to redistribute it along the spindle, to maximize its role in microtubule organization, where it may be needed to bundle and slide microtubules, or even transport short microtubule fragments. While more global effects of HSET on spindles have been shown, it has not yet been directly shown that HSET specifically localizes to minus ends in the spindle, where it may regulate their dynamics. HSET is localized throughout the entire spindle, and is not necessarily concentrated at the spindle poles, so it has been difficult to distinguish between HSET's global effects on spindle morphology versus the specific effects on the dynamics of individual microtubules. One of the major obstacles to overcome in order to test this would be to differentiate individual microtubule minus ends in the spindle to begin with. This may take some clever imaging approaches, such as photobleaching, photoconvertible tubulin, or fluorescent speckle microscopy, in order to decrease the background signal of the dense network of microtubules to be able to measure dynamics of minus ends. Another *in vitro* approach could be the use of purified centrosomes to nucleate microtubule asters in the presence or absence of purified HSET, potentially even with cell extracts to better reconstitute a mitotic microtubule architecture and microtubule regulation.

In conclusion, our results provide additional insight into the mechanism by which HSET binds to tubulin oligomers, as well as interacts with the tip-binding protein EB1. These results bring about new questions and open the door for many future avenues of investigation regarding the mechanism of HSET-tubulin clusters and how they regulate microtubule minus ends dynamics.

5.4. Methods

5.4.1 Protein Purification

Tubulin was purified and labeled as previously described in Chapter 2. EB1, EB1ΔC, and EB1–GFP was expressed in *Escherichia coli* and purified as previously described (Zanic et al., 2009) and stored in 10 mM Bis-Tris, 10 mM Tris-HCl, 100 mM KCl, 1mM DTT, 5% glycerol, pH 6.6. His6-HSET and His6-HSET tagged with enhanced GFP was expressed in *Spodoptera frugiperda* (Sf9 cells) and purified as previously described (Norris et al., 2018), and stored in 10 mM K-HEPES, pH 7.7, 300 mM KCl, 1 mM dithiothreitol, 100 µM $MgCl_2$, 100 µM ATP, and 20% sucrose. XMAP215 was expressed in Sf9 cells using the Bac-to-Bac system (Invitrogen) and purified using a HisTrap followed by gel filtration (adapted from Brouhard et al., 2008), and stored in 10 mM Bis-Tris, 10 mM Tris-HCl, 100 mM KCl, 1 mM DTT, 10% glycerol, pH 6.6. Protein concentration was determined using absorbance at λ =280 nm or a Bradford assay (Kielkopf et al., 2020).

5.4.2 HSET-tubulin clusters

These experiments were set up in the same away as the basic dynamics assay described in Chapter 2 with the following changes. The antifade solution contained 40 mM D-glucose, 40

μg/ml glucose oxidase, 16 μg/ml catalase, 0.5 mg/ml casein, 10 mM dithiothreitol, and 50 mM KCl, and 1 mM ATP in BRB80. Unlabeled HSET was diluted in a BRB80-casein mixture consisting of BRB80 supplemented with 0.25 mg/ml casein and kept on ice. 647-tubulin and 488-tubulin were diluted in BRB80 and kept on ice. The final reaction mix was made by combining antifade, BRB80, HSET, 647-tubulin and 488-tubulin on ice, and immediately added to the flow cell with the GMPCPP seeds, and imaging was commenced immediately as well. Movies were imaged at 0.3 FPS for 20 min in the 561, 488, and 561 channels. Kymographs were made of each microtubule based on the rhodamine seed channel, and tracks were individually marked and counted for 561-tubulin and 647 tubulin and compared to the merge kymographs to differentiate between the single-color and two-color merged tracks. Only processive minus-end directed tracks were counted; static tracks were not included.

5.4.3 HSET and EB1-GFP Dynamics assays

Dynamics assays were performed as previously described in Chapter 2, except that reaction mixes were additionally supplemented with 1mM ATP. Movies were imaged at 0.2 FPS for 30 min. Analysis was also performed as previously described.

5.4.4 HSET, XMAP, and EB1/ EB1ΔC Dynamics Assays

Dynamics assays were performed as previously described in Chapter 2 with the following changes. The antifade solution contained 40 mM D-glucose, 40 μg/ml glucose oxidase, 16 μg/ml catalase, 0.5 mg/ml casein, 10 mM dithiothreitol, and 50 mM KCl, 1 mM GTP, and 1 mM ATP in BRB80 supplemented with 0.1% methylcellulose. Movies were imaged at 0.3 FPS for 20 min. Analysis was performed as previously described.

Chapter 6

Conclusions and Future Directions

Although the majority of the work done to better understand microtubules and their regulation by associated proteins has focused on the plus end, the minus end is an equally worthwhile subject of investigation. Even after decades of research into fundamental questions, like defining the mechanism of catastrophe, we still do not have clear answers to them. Better understanding the molecular mechanisms of the minus end may be the key that leads to finally answering some of these long-lasting unknowns.

6.1 Comparing microtubule plus and minus ends

The nature of the minus end, in all of its similarities and differences to the plus end, makes for a paradox. How is it that the two microtubule ends, which technically consist of identical material, are functionally different? The sole apparent difference between the two ends is the orientation of the α/β-tubulin dimer, which presumably would be forming identical head-to-tail bonds at either end, but herein lies a potentially false assumption. Although the polar non-covalent bond formation occurs between two tubulin dimers, the orientation of the dimers being polymerized must in fact be extremely important. We observe different kinetic rates of tubulin incorporation at the plus and minus ends, which would be dictated by differences in underlying bond formation energies. A growing minus end has a 'crown' of α-tubulin as the exposed dock for incoming tubulin dimers, while the plus end conversely consists of a 'crown' of β-tubulin. This difference in polarity could result in subtly different milieus, that impact how energetically

favorable it is for incoming tubulin dimers to associate or disassociate. This especially makes sense in light of the fact that soluble tubulin dimers exhibit an asymmetrical curved conformation (Gigant et al., 2000; Ravelli et al., 2004; Buey et al., 2006; Rice et al., 2008; Nawrotek et al., 2011; Brouhard and Rice, 2014). It could be imagined that at minus ends, it is more difficult for a bent dimer to reconfigure into a straighter conformation upon incorporation, but once it is complete, it becomes less favorable to dissociate. Due to the complex nature of calculating bond energies at microtubule tips, we rely on computational models to estimate the longitudinal and lateral bond energies between dimers and calculate the dynamic and structural impacts of changing sets of finely tuned parameters. Supporting this idea of different microtubule tip milieus, Molodtsov et al. (2005) suggest that based on their computational models, the difference in stability of tubulin incorporation may be explained by the asymmetry of the tubulin dimer and its conformational change. Because the conformational changes to the dimer are more dramatic in the β-tubulin subunit (containing the E-site), the orientation of the dimers at the plus end would then lead to the equilibrium angle between an incorporated tip dimer and an incoming dimer would be largely determined by the incorporated dimer with the β-tubulin side facing outwards, leading to a smaller stabilizing effect during addition (Molodtsov et al., 2005). In contrast, the equilibrium angle between the two associating dimers would be determined by the incoming dimer at the minus end, resulting in more stabilizing effect (Molodtsov et al., 2005). Importantly, computational models describing bond energies and tip structures make assumptions based on existing data, which there is very little of regarding the minus end. Our studies of the minus end may better inform future computational models describing the molecular mechanisms at the microtubule tip.

Another important question is what are the structural differences between the plus and minus ends? Not only do they have different micro-environments at the microtubule tips, but the dimers at the tip could have significantly different morphologies that underlie the differences in molecular rates. Nearly all recent cryo-EM or cryo-ET studies of microtubule tip structure focus on the shape of the plus-end tip, and largely ignore that of the minus end. One recent study included cryo-ET traces of both plus-end and minus-end tips of GMPCPP microtubules (Atherton et al., 2018). The authors did not find statistically significant differences in the distance from the extended protofilaments to the microtubule wall when comparing the two ends; however, the representative traces from the minus-end tip protofilaments appear much longer than that of the plus ends, suggesting perhaps, that minus ends may be more tapered than plus ends, although this was not measured in these data. It will be crucial for future studies to replicate these results and further show differences between plus- and minus-end tip structures with dynamic microtubule extensions. This suggestion that the minus end may be more tapered than the plus end seems to contradict our observations of minus ends, in that they have slow tubulin kinetics and small but stable GTP-caps. We would expect more dynamic ends to be more tapered, rather than the opposite. This is one of several intriguing remaining questions regarding the nature of minus ends.

6.2 GTP hydrolysis at the two ends

Another facet of the unknown differences in structure between the two ends is the composition of the GTP-cap at the two ends, and the mechanism of GTP-hydrolysis. Models built to describe this process have historically been developed based on plus-end observations, and do not typically account for the behavior of the minus end. One simplified model to explain

the mode of hydrolysis and how it relates to catastrophe frequency is the coupled-random hydrolysis model, in which tubulin dimers stochastically undergo hydrolysis, but only after they are no longer at the terminal position at the tip, at least one tubulin layer beneath (Bowne-Anderson et al., 2013). This is based on the idea that at the plus end, the E-site of the β-tubulin must be covered by another dimer and cannot hydrolyze when it is at the terminal 'crown' position. For the minus end, the E-site is buried beneath the 'crown' position of the α-side of the tubulin dimer- is this coverage sufficient to allow hydrolysis, or is this terminal dimer also unable to hydrolyze? Because we know so little about how the proposed 'rules' of GTP hydrolysis may be universal for the two ends, or perhaps only plus-end specific, the answers to these basic questions are not known.

In our work, we found that the approximate rate of hydrolysis appeared to be the same for both ends, and rather the GTP-cap size for both ends was predominately determined by the growth rate. This was estimated by measuring the intensity fluorescence profile of EB1 at both ends, as well as the delay times to catastrophe during tubulin dilution experiments. While EB1 is presumed to be the standard reliable method for measuring the GTP-cap size at the ends of microtubules, there are some caveats. First, it is not entirely known what EB1 is specifically recognizing (and what it is not). A previous study using nucleotide analogues suggested that it recognizes the transitional GDP-Pi state of tubulin, rather than GTP-tubulin itself (Maurer et al., 2014). Because the exact consistency of the GTP/GDP-Pi cap is not known, it is hard to determine what EB1 preferentially binds to, especially when EB1 is the very tool often used to measure the nucleotide state. Another complication of EB1 is that it affects microtubule dynamics by increasing growth rate and increasing catastrophe frequency at growing microtubule ends; some have suggested that a component of the mechanism for this effect is by

altering the hydrolysis rate itself (Maurer et al 2014). In addition to recognizing different nucleotide states, EB1 has been recently proposed to recognize the structural state of the tip as well, by showing preference for more structurally disrupted, tapered microtubule tips, rather than blunt ones (Reid et al., 2019).

Another recently developed approach to studying GTP-hydrolysis and EB protein binding comes from the advancement of purifying recombinant tubulin with mutations that affect the rate of hydrolysis (Roostalu et al., 2020). In this work, recombinant tubulin was successfully purified, and several mutated iterations that were predicted to impede the rate of hydrolysis to varying degrees were compared. The authors observed that indeed, the microtubules were more stabilized overall, and the stretches of EB3 comets at the tips were longer, consistent with slowed hydrolysis (Roostalu et al., 2020). Although the impact on minus ends was not addressed in this work, the mutant tubulin-grown minus ends appeared to be affected similarly to the plus ends, in terms of stabilization. Most intriguingly, there are examples of these mutant microtubules that show both ends look almost indistinguishable in terms of growth rate and EB3 signal (Roostalu et al., 2020). This breakthrough recombinant tubulin technique may allow for many novel experiments to be done to significantly advance our understanding of the similarities and differences between the two microtubule ends.

6.3 Structural recognition of the two ends

A key to elucidating some of the structural differences between the two microtubule ends may be the localization of various MAPs. There are MAPs that specifically recognize the plus end (XMAP215), those that specifically recognize the minus end (HSET, CAMSAP), and finally, those that recognize both microtubule ends (EB1, MCAK) (Brouhard et al., 2008; Jiang

et al., 2014; Hendershott and Vale, 2014; Desai et al., 1999; Strothman et al., 2019). This implies that while there are shared recognizable features at the two ends, there are also key differences allowing certain MAPs that distinguish between the two ends. EB1 binds the stabilizing GTP-tubulin cap region at the end of the microtubule by recognizing the nucleotide state of the tubulin. MCAK, in contrast, likely does not recognize the nucleotide state at the ends of microtubules, but rather it has been proposed to recognize some feature such as the curvature or flexibility of the terminal tubulin dimers (Patel et al., 2016). If it were recognizing a very specific pocket of the outermost tip of a terminal tubulin dimer, then it would likely be able to discriminate between the two microtubule ends, since a different side of the dimer is exposed at either end, but this does not seem to be the case.

In our studies, we found that HSET processively walked towards the minus end and tip-tracked minus-end tips. Interestingly, we saw that even when HSET was not able to form multi-motor clusters, from the lack of tubulin in solution, it would diffuse along a stabilized, non-dynamic microtubule and accumulate over time at minus-end tips specifically. Therefore, it is not just that it is localizing at the microtubule tip that to which it is being translocated, but rather there is some specific recognition of the minus end by HSET. We do not know whether it may be the MTBD in the motor or tail region that is recognizing the minus end, and what feature of the minus end it is that HSET may be recognizing. XMAP215 is an example of a plus-end localizing protein, which binds to microtubules through several TOG-domains. It is thought that XMAP is best able to position itself at plus ends, rather than minus ends, through the orientation of its different TOG domains, such that the N-terminal TOG domains bind the plus-end-specific orientation of curved tubulin at the microtubule tip, and the C-terminal TOG domains bind the microtubule lattice (Akhmanova and Steinmetz, 2015; Ayaz et al., 2012, 2014). Overall, the

study of microtubule-associated proteins and their interactions with tubulin and microtubules can greatly contribute to our understanding of the structural nature of the two ends, by disentangling the similarities and differences of recognition of the two ends by other proteins.

6.4 Minus ends in cells

Although the characterization of minus ends as slow-growing and more stable than their plus-end counterpart has been observed in numerous *in vitro* studies over many decades, the minus-end dynamics observed in cells has been very different. Many reports of minus-end dynamics in cells report that the minus ends are either stable or undergo shrinkage (Vorobjev et al., 1999; Rodionov et al., 1999; Yvon and Wadsworth, 1997; Dammermann et al., 2003; Rogers et al., 2005). Often this gives rise to microtubule 'treadmilling' behavior, where the plus end polymerizes while the minus end depolymerizes, but the net length of the polymer stays relatively constant- or at least has enough length to maintain its existence. Though minus ends have fundamentally slower tubulin kinetics and inherent stability, there must be other factors that result in a drastically different dynamic profile in cells, when they can be measured. Often, minus ends are capped by γ-tubulin, and presumably non-dynamic, but there are also many instances of uncapped, so-called "free" minus ends in cells (reviewed in Chapter 1). For many decades the canonical observations of un-anchored minus end dynamics in cells were that the minus ends were either in a paused or depolymerizing state, and that minus-end polymerization in cells does not occur (Akhmanova and Steinmetz, 2015). The pause state of these minus ends is likely due to their capping, probably by γ-tubulin, even when they are not anchored at organelles, and the depolymerization may be induced by other cellular conditions and regulatory factors. However, there is evidence to show active polymerization of minus ends in cells (Feng et al.,

2019; Goodwin and Vale, 2010). The study by Goodwin and Vale was done in *D. melanogaster* S2 cells, which lack a central MTOC, and it was observed that in the absence of the capping factor Patronin (a homolog of CAMSAP), minus ends exhibited the full range of dynamic behaviors observed *in vitro* (Goodwin and Vale, 2010). However, it was not observed in the wild-type condition, indicating that while these minus ends are competent to be dynamic, they may typically be prevented from dynamics by other factors (Goodwin and Vale, 2010). The study by Feng et al. (2019) not only observed active minus-end growth in neuronal dendrites marked by EB signal, but it also showed that this minus-end growth is important for proper microtubule organization in the dendrites, which contain a mixed-polarity microtubule orientation (Feng et al., 2019). This study that carefully observes and tracks cellular minus ends debunks the sweeping assertions that minus ends are incapable of growth in cells and show that despite decades of observations of microtubule dynamics in cells, there are still fundamental observations to be made. If these microtubule minus ends are clearly growing in this cellular milieu, then why has it not been observed for decades, and is only being reported now? This study addresses this point as well, and points to several previous studies in which the figures showed what appears to be minus-end dynamics, although in every one of these examples, the phenomenon of minus-end growth was overlooked. This leads to the alarming idea that the prevailing notion that cellular minus ends are not dynamic and therefore not a topic of interest has led to studies in which this assumption has prevented actual data of dynamic cellular minus ends from being analyzed and reported. This example illustrates the necessity of letting observations speak for themselves, and not letting potential insights go unnoticed from biases about what is or is not possible in the cell. Although historically, the study of minus ends in cells has been largely hindered by technical difficulties to adequately visualize them, there have been

increasing advancements in both light microscopy as well as genetic manipulation, that may be crucial to making further novel insights into minus ends in cells. Our knowledge about the vital roles of minus ends in cells and the growing network of known minus-end regulators indicates that this is an understudied area that clearly warrants further investigation.

6.5 HSET

In this work, we have characterized several key components of HSET's regulatory function at minus ends; however, many more questions remain. While we have demonstrated that HSET specifically suppresses minus-end catastrophe by effectively decreasing the GTP-tubulin off-rate at the minus-end tip, we do not yet know further mechanistic detail into how precisely HSET accomplishes this regulatory effect. It is likely that this occurs through one of the two microtubule-binding domains in the protein: either in the tail or motor region. Additionally, we could consider that the tubulin cluster scaffold that enables the processive translocation of the motor to the minus-end tip could play a role in the stabilizing effect by increasing the local concentration of soluble tubulin proximal to the growing tip. However, we have several pieces of evidence to suggest that this may not be a predominant mechanism of stabilization. First, we observed in the analysis of HSET-tubulin cluster assembly using two stocks of differentially labeled fluorescent tubulin, that the processive tracks of tubulin were largely single-color, and did not appear to change color or turn over soluble tubulin, at least during the timescale of the processive run-lengths. At the stabilized minus-end tip, where many tubulin tracks converge and accumulate over time, it is unclear whether this changes such that the tubulin held by HSET can now turn over. In any case, we do not have any evidence so far to suggest that HSET-tubulin clusters experience turnover of tubulin, suggesting that the tubulin at the tips may not be

available for incorporation during growth. Secondly, when we analyzed the minus-end dynamics in the presence of HSET, we saw a decrease in catastrophe frequency, but not an increase in growth rate. If HSET worked to stabilize minus ends by increasing the local concentration of tubulin at the minus-end tip, we would expect to see a corresponding increase in the minus-end growth rate. Finally, even when we did perform a tubulin titration, we did not see a robust effect of tubulin concentration on minus-end catastrophe frequency, especially compared to the robust effect on the plus end. Taken altogether, these data suggest that the incorporation of the HSET-clustered tubulin at the minus-end tip is not a likely mechanism for its stabilizing effect. The remaining mechanistic possibilities include binding of the motor or tail domains to the minus-end tip. For example, it has been proposed that the kinesin-5 motor Eg5 promotes polymerization of microtubules through a "zippering" model in which the motor head binding promotes tubulin attachment and the curved-to-straight transition upon incorporation at the tip (Chen et al., 2019). Although Eg5 has different regulatory effects on microtubule plus-end dynamics, it could be imagined that one possibility for HSET is that the motor domain binds to the terminal tubulin dimers in such a way as to decrease their off-rate and suppress catastrophe. On the other hand, the tail domain could be involved in the mechanism, although the geometry of this potential mechanism is challenging to imagine, since the tail would likely need to be simultaneously binding the tubulin cluster as well as the minus-end tip, but in such a way that also allows tip tracking. Alternatively, HSET could be regulating minus-end dynamics through a completely different mechanism that is not suggested here. It will be important for future studies to perform structure-function analysis of HSET, and possibly some detailed structural biology techniques to differentiate between these possibilities.

6.6 Comparing minus-end regulators HSET and CAMSAP

The list of known minus-end regulators lags far behind that for the plus end, but studies in the past decade have characterized an increasing number of minus-end proteins, the most well-known of which is the CAMSAP/Nezha/Patronin family of proteins. Because more detailed mechanistic studies have been done to better understand the function of CAMSAP, it provides an opportunity to compare CAMSAP to other less studied minus-end regulators, such as HSET. The different localization patterns of HSET and CAMSAP proteins at microtubule minus ends supports the idea of different mechanisms of stabilization by the two proteins. CAMSAP2 decorates the growing minus-end lattice, resulting in extended stretches of CAMSAP marking where CAMSAP bound during growth (Hendershott and Vale, 2014; Jiang et al., 2014). These stretches of stabilized CAMSAP-decorated minus ends can even serve as a type of 'seed' if the microtubule is otherwise destabilized. For example, when a microtubule is severed, the plus end that depolymerizes to the CAMSAP-decorated 'seed' may regrow from that highly stabilized microtubule portion (Hendershott and Vale, 2014; Jiang et al., 2014). In contrast, HSET localizes to the most distal portion of the minus-end tip during minus-end growth as it tip-tracks. Whereas the localization of CAMSAP on extended minus-end grown lattice portions suggests that its mechanism comes through reinforcing the lattice structure over microns of length (Jiang et al., 2014), HSET appears to concentrate only at the most dynamic part of the minus-end tip, where it regulates the GTP-tubulin off-rate, but does not show any clear evidence of impacting the microtubule lattice. Although they act through different stabilizing mechanisms, both CAMSAP and HSET are capable of protecting minus ends from the destabilizing effects of other MAPs, such as MCAK. The implications of physiological relevance for these two minus-end stabilizers are interesting as well. CAMSAP family proteins are active during interphase and have been

shown to have significant roles in microtubule organization, such as the establishment of cell polarity in endothelial cells and minus-end stabilization in mixed-polarity dendrites in neuronal cells (Martin et al., 2018; Yau et al., 2014; Feng et al., 2019; Cao et al., 2020; Noordstra et al., 2016; Tanaka et al., 2012; Toya et al., 2016). HSET, on the other hand, is primarily active in mitosis in many cell types, and along with its role in stabilizing minus-end dynamics, it has a significant role in microtubule organization (Mountain et al., 1999; Cai et al., 2010; Kwon et al., 2008; Muralidharan and Baas, 2019; Ems-McClung et al., 2020). HSET toggles between modes of bundling antiparallel arrays of microtubules as an individual motor protein and forming three-dimensional aster-like microtubule arrays when HSET is clustered into multi-motor teams (Norris et al., 2018). The subtle differences in mechanistic underpinnings of these two minus-end stabilizers gives rise to dramatic differences in their respective physiological roles.

6.7 HSET and other MAPs

In addition to not knowing the mode of binding and regulation of minus ends by HSET, we further do not know how HSET is able to regulate minus ends in the presence of other regulatory MAPs, such as MCAK or EB1. Our data shows that on stabilized GMPCPP seeds as well as dynamic microtubules, HSET has the dominant regulatory effect on minus ends when MCAK is also present. It would be interesting to better understand the mechanism of this antagonism, as has been done with the similarly antagonistic relationship between CAMSAP and MCAK (Atherton et al., 2017). For CAMSAPs, it has been shown that the preferential binding site of its CKK domain is at the interprotofilament interface between dimers, and at the transition zone between the curved and straight lattice regions proximal to this tip; this localization sterically hinders MCAK from binding the minus end tips, and therefore CAMSAP is able to stabilize

minus ends even in the presence of MCAK (Atherton et al., 2017). It is very possible that HSET localized at minus-end tips, especially in multi-motor tubulin cluster form, works in a similar fashion to sterically hinder MCAK from reaching the minus-end tip where it exerts its depolymerase activity. Alternatively, if MCAK is in fact able to reach the minus-end tip, it is possible that HSET has a stronger effect on stabilizing the tips, such that MCAK is not effective. Alternatively, HSET could be changing something about the structure or topography of the minus-end tips such that MCAK cannot properly recognize or bind to the tip, or undergo the catalytic cycle necessary to dissociate dimers from the microtubule end. We also found that HSET was able to counteract the destabilizing effects of EB1 at minus-end tips as well, even when it was highly concentrated there by HSET itself. Conversely, HSET localized to plus ends through direct EB1 binding did not show any stabilizing effects. The possible mechanisms and physiological context for these results is discussed at length in Chapter 5. Overall, these results bring up many interesting questions and future directions for better understanding the molecular mechanisms of HSET alone, as well as in the context of other microtubule regulators.

6.8 The physiological role of HSET

While HSET has been typically studied as a mitotic protein, because of its nuclear localization during interphase, and its identification as a key factor aiding cell division in abnormal cancer cells, recent studies have found that HSET/KIFC1, as well as its family member KIFC3 have roles in neurons, a terminally differentiated cell type (Muralidharan and Baas, 2019; Cao et al., 2020). So far, these studies have shown that HSET maintains a high level of expression in neurons throughout development into adulthood, unlike most other kinesins, as dynein is the primary mediator of microtubule positioning (Muralidharan and Baas, 2019). In

this study, HSET was shown to not just have a redundant role to dynein, but rather HSET was shown to have key roles in sliding microtubules into alignment and crosslinking them in the context of the neuronal growth cone (Muralidharan and Baas, 2019). This work goes on to imply that HSET may have a role in poorly understood neuronal processes such as growth cone stalling and axonal retraction, which may also have broad relevance to neurodegenerative disease. Another recent work examined the role of KIFC3 in dendrites and found that KIFC3 and CAMSAP were binding partners that localize to minus ends in dendrites, where they function to immobilize the microtubules into place (Cao et al., 2020). These recent studies open up a number of fascinating future directions, such as whether there is a potential role for KIFC1 in dendrites as well, or whether KIFC1 or KIFC3 exert any effects on cellular minus-end dynamics, especially since dendrites are one cellular milieu where active minus-end growth has been observed. Finally, it will be interesting to understand the potential similarities and differences among the roles and mechanisms of HSET in the mitotic spindle, versus in neurons.

In conclusion, the “dark side” of the microtubule, the microtubule minus end, potentially represents an untapped resource in the microtubule field that may help to answer long unanswered questions into the structures of the microtubule tips, the mechanism of catastrophe, and cellular microtubule organization in general. Though this work establishes some fundamental characterizations into minus ends, and their regulation by the kinesin-14 HSET, there are many fascinating avenues of exploration that remain.

Appendix

A.1 Kinesin-11 VAB-8 binds microtubules and does not exhibit processive motility

A.1.1 Introduction

The nervous system encompasses a complex system of communication among a vast network of individual cells in order to execute certain tasks and functions. Neurons in this system may communicate with each other in several ways, through the use of synapses, which help dictate specificity. In order to communicate properly, neurons must be able to distinguish amongst various partners to signal to the proper target. Chemical synapses are the predominant type, in which chemical signaling components are released by one neuron across a synaptic cleft which are subsequently recognized by receptors and ion channels of another neuron (Alberts et al., 2008). Another form of signaling occurs through electrical synapses, also called gap junctions (Alberts et al., 2008). While chemical synaptic specificity has been studied extensively, what factors dictate electrical synapse specificity are not well understood. Gap junctions physically connect adjacent cells by forming a channel across their respective membranes, allowing the flow of ions and small molecules across the two cells, such that electrical signaling can be transduced near-instantaneously among connected cells (Alberts et al., 2008).

A.1.1.1 VAB-8 affects C. elegans gap junction placement in VA neurons

One clear example of selective electrical synapse formation occurs in the motor neurons of *C. elegans,* which drive the movement of the worm. The Ventral A (VA) and Ventral B (VB) motor neurons are connected to AVA and AVB interneurons. In the wildtype (WT) worm, AVA interneurons connect to the processes of VA neurons through both chemical and electrical

synapses, and AVB interneurons connect to the VB neurons via electrical synapses alone. UNC-4 is a transcription factor that regulates the gap junction specificity of this circuit and is expressed in VA motor neurons, and in an *unc-4* mutant, miswiring is observed, in which VA neurons form ectopic gap junctions with AVB interneurons. In a screen for transcripts in this *unc-4* mutant, a trafficking defect was also observed, and the only molecular motor that was differentially expressed was the noncanonical kinesin-11 VAB-8. Normally, VAB-8 expression is blocked by UNC-4 but is ectopically expressed in VA motor neurons in *unc-4*. We were interested in further characterizing the role of VAB-8 in disrupting gap junction placement and gap junction trafficking in the *C. elegans* motor neuron circuit. Specifically, we sought to express and purify VAB-8, and characterize its ability to (i) bind to microtubules, (ii) exhibit motility, and (iii) affect microtubule dynamics *in vitro*.

A.1.2.2 VAB-8 is predicted to be a non-catalytic motor

The *C. elegans vab-8* gene encodes several different protein transcripts, referred to as VAB-8L and VAB-8S (Wolf et al., 1998), and can also be referred to as klp-5 (Siddiqui, 2002). In this work, we only refer to the properties and study of VAB-8L, referred to throughout as simply VAB-8. VAB-8 has a predicted N-terminus kinesin motor sequence, but one that is highly divergent from canonical sequences (Wolf et al., 1998). The kinesin-11 family contains other motors with highly divergent motor domains, and the putative motor domain of VAB-8L is as divergent from these other members (smy1p and cos2) as it is from conventional motor domains (Wolf et al., 1998). *D. melanogaster* Cos2 binds microtubules, but lacks ATPase activity (Wolf et al., 1998; Sisson et al., 1997). Nonetheless, VAB-8 is categorized under the kinesin-11 super family, which also contains KIF26A, KIF26B, and SMY1 (Miki et al., 2005). Altogether, the

members of the kinesin-11 family have low consensus motif conservation compared to other kinesin families (Miki et al., 2001).

Although VAB-8 differs from the other kinesin-11 family members, it may share some broad similarities. KIF26A is one of the more well-studied members of this family, and has been shown to contain a motor domain that binds to microtubules but lacks ATPase activity (Niwa, 2015), similar to the predicted motor functionality of VAB-8. Further, KIF26A does not show microtubule gliding activity *in vitro* (Niwa, 2015), but it does bundle and stabilize microtubules when overexpressed in Cos7 cells with unstable microtubules (Niwa, 2015). Any occurrence of autoinhibition of KIF26A is unknown (Niwa, 2015). KIF26A is involved in regulation of cell signaling of enteric neurons (Zhou et al., 2009) and has a role in stabilizing neuronal microtubules, but it is not known how it specifically affects microtubule dynamics (Niwa, 2015). Kinesin-11 Cos2 also binds microtubules but lacks ATPase activity, and is involved in signaling pathways (Wolf et al., 1998; Sisson et al., 1997).

Assessment of ATPase activity of KIF26A *in vitro* was done with bulk sedimentation assays. In this assay, the purified motor domain of KIF26A was incubated with stabilized microtubules and AMPPNP (a non-hydrolysable form of ATP), and this was centrifuged to separate the microtubule-bound and unbound fractions, in the pellet and supernatant respectively. The pellet containing the motor and microtubules was isolated, and the solution was buffer exchanged for one containing ATP. KIF26A motor was still associated with microtubules in the pellet, unlike conventional kinesin KIF5A, which dissociated with MTs in the presence of ATP, as part of its ATPase cycle (Zhou et al., 2009). This suggests that KIF26A does not exhibit ATPase activity similar to KIF5A.

VAB-8 contains some, but not all, residues required for formation of an ATP-binding pocket, which indicates the likelihood of VAB-8 lacking ATPase activity (Wolf et al., 1998). However, it does contain a critical conserved arginine residue in a cluster of basic amino acids important for binding human kinesin heavy chain to microtubules (Wolf et al., 1998). Finally, the predicted secondary structure of the VAB-8 N-terminus also closely matches that of human kinesin heavy chain motor domain (Wolf et al., 1998; Kull et al., 1996). To date, very little work has been done *in vitro* to characterize VAB-8. VAB-8 and UNC-51 have been reported to bind *in vitro* (Lai and Garriga, 2004), and VAB-8 has been recently reported to bind to microtubules and show diffusive motion along the microtubule (Balseiro-Gómez et al., 2021).

A.1.2 Results

To characterize VAB-8-GFP *in vitro*, we expressed and purified VAB-8-GFP in Sf9 cells (Figure A.1.1A). We were first interested in seeing whether the protein bound to microtubules and exhibited any directed motility, which would indicate conventional ATPase activity. To do this, we performed a single molecule stepping assay in which low concentrations of VAB-8-GFP were added to flow cells containing rhodamine-labeled Taxol-stabilized microtubules (Figure A.1.1B). We observed preferential localization of VAB-8-GFP to microtubules, which was especially clear in the maximum intensity projection of the VAB-8-GFP signal over time (Figure A.1.1C). Consistent with the observations of Balseiro-Gómez et al. (2021) who performed a similar assay with VAB-8 overexpressed in cell lysates, we observed many puncta of purified VAB-8-GFP protein associating transiently with the microtubule lattice, as well as puncta diffusing along the lattice for several seconds. (Figure A.1.1D). Although the results of VAB-8

binding to the microtubule lattice and diffusing are consistent, it is important to note that there may be subtle differences in the behavior of VAB-8 due to the presence of other cellular factors.

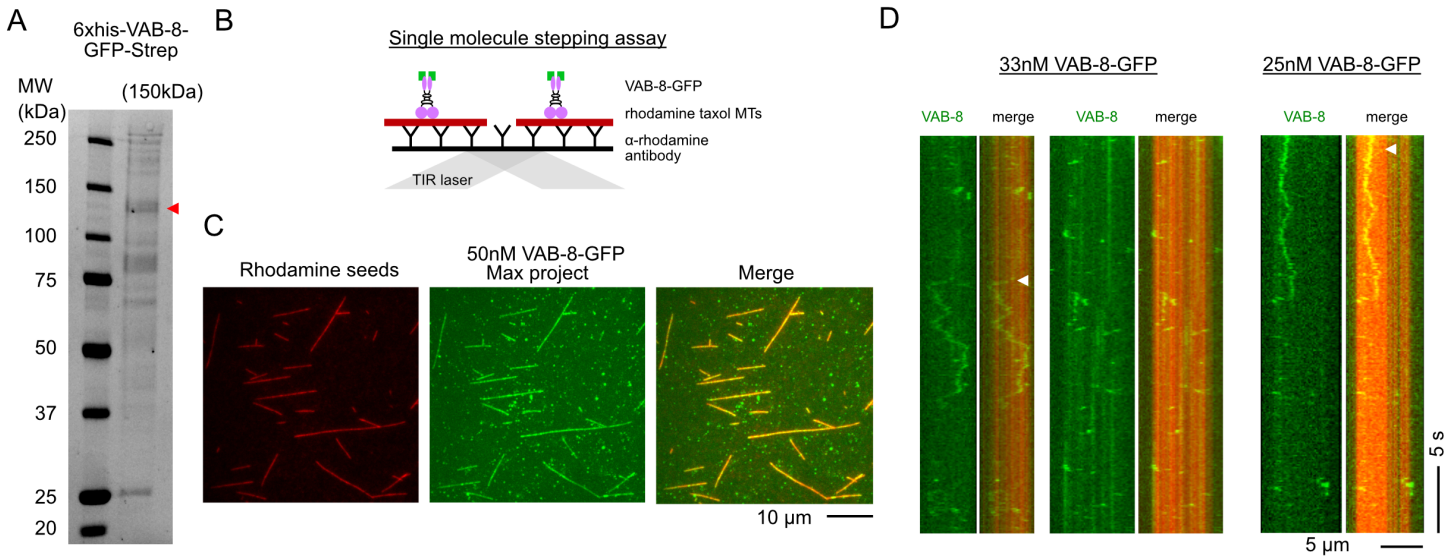

Figure A.1.1. VAB-8 binds microtubules and shows diffusive motility. (A) Stain-free SDS-PAGE gel of purified VAB-8-GFP protein. Molecular weight (MW) markers are indicated on the left. Red arrow indicates VAB-8-GFP band. (B) Schematic of the single-molecule stepping assay, in which rhodamine-labeled Taxol-stabilized microtubules are bound to the coverslip and low concentrations of VAB-8-GFP are added to visualize localization and movement of the motor. (C) Representative field of view from single molecule stepping assays. The maximum intensity project for the VAB-8-GFP channel is shown along with the image of the seed position taken before the movie. Merge shows colocalization of VAB-8-GFP with the seeds. (C) Representative kymographs showing the VAB-8-GFP signal alone and merged with the rhodamine-microtubule seed. Several examples from two protein concentrations are shown. White arrows indicate longer runs of VAB-8-GFP.

Next, we tested the motility of VAB-8 by performing a gliding assay in which GFP-VAB-8 was attached to the coverslip via binding to an anti-GFP antibody, and rhodamine-labeled Taxol-stabilized microtubules were flown in and incubated with ATP (Figure A.1.2A). As a negative control, storage buffer was used in lieu of protein, and for a positive control, the super-processive

kinesin-8 Kip3-GFP was used, as it is well-characterized to exhibit robust directed motility. As we expected, we observed only minimal and transient binding of microtubules over the course of the time-lapse in the absence of kinesins, as evidenced by the low counts of microtubules on the surface at the end of the movie (Figure A.1.2C). When Kip3-GFP was present, we observed robust microtubule landing, and clear evidence of microtubule gliding, at an average velocity of 20.8 ± 0.59 nm s^{-1}, SE, n = 189 (Figure A.1.2 B-D). In the presence of VAB-8, microtubules also efficiently landed to the surface, but did not show any directed motility over time, as evidenced by an average velocity of 0.29 ± 0.02 nm s^{-1}, SE, n = 205 (Figure A.1.2 B-D). Altogether our data indicates that consistent with previous predictions that VAB-8 is capable of binding to microtubules, and that it does not exhibit directed motility on microtubules, but rather some diffusive motion.

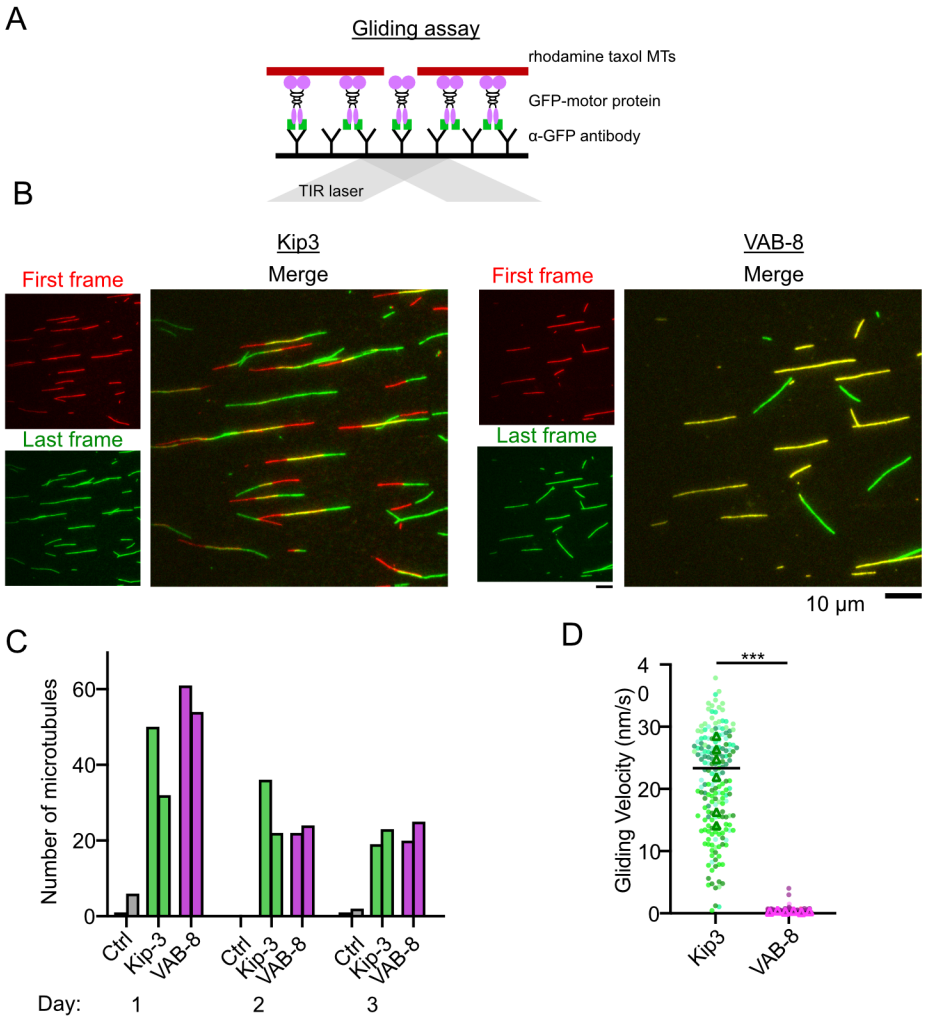

Figure A.1.2. VAB-8 binds microtubules and does not show directed motility. (A) Schematic of gliding assay set-up. GFP-labeled motor proteins are attached to the coverslip via an α-GFP antibody. Rhodamine-labeled Taxol-stabilized microtubules are added. In the control, empty VAB-8 storage buffer was added to the coverslip instead of protein. (B) Representative images from the Kip3 and VAB-8 gliding assay. 700nM of Kip3 and 1μM VAB-8 was used First frame of the movie is shown in red, and the last frame in green. Merge shows the difference in microtubule position. Scale bars are 10 μm. (C) Number of microtubules on the coverslip surface in the last frame of each movie. Two movies of each condition (Ctrl, Kip3, and VAB-8) were taken on each of three days. (D) Gliding velocities of microtubules incubated with Kip3 or VAB-8. Individual measurements are shown for each day, as well as the mean velocity for each of the six repeats. Line indicates the mean. Welch's t-test was performed between the two conditions, ***$p \leq 0.001$.

Finally, we were interested in determining whether VAB-8 had an effect on microtubule dynamics. One mechanism by which VAB-8 is able to disrupt the transport and placement of gap junctions could be through affecting microtubule dynamics in order to alter the microtubule architecture such that the transport of gap junctions by other kinesins was disrupted, and the gap junctions could not reach their proper locations. To investigate this, we performed a dynamics assay comparing a control condition containing 10 μM tubulin and VAB-8-GFP storage buffer to one containing 125 nM VAB-8-GFP. We measured the four dynamics parameters for each of these conditions across three repeats and found no statistically significant difference between any conditions measured at either the plus or minus end in the absence or presence of VAB-8.

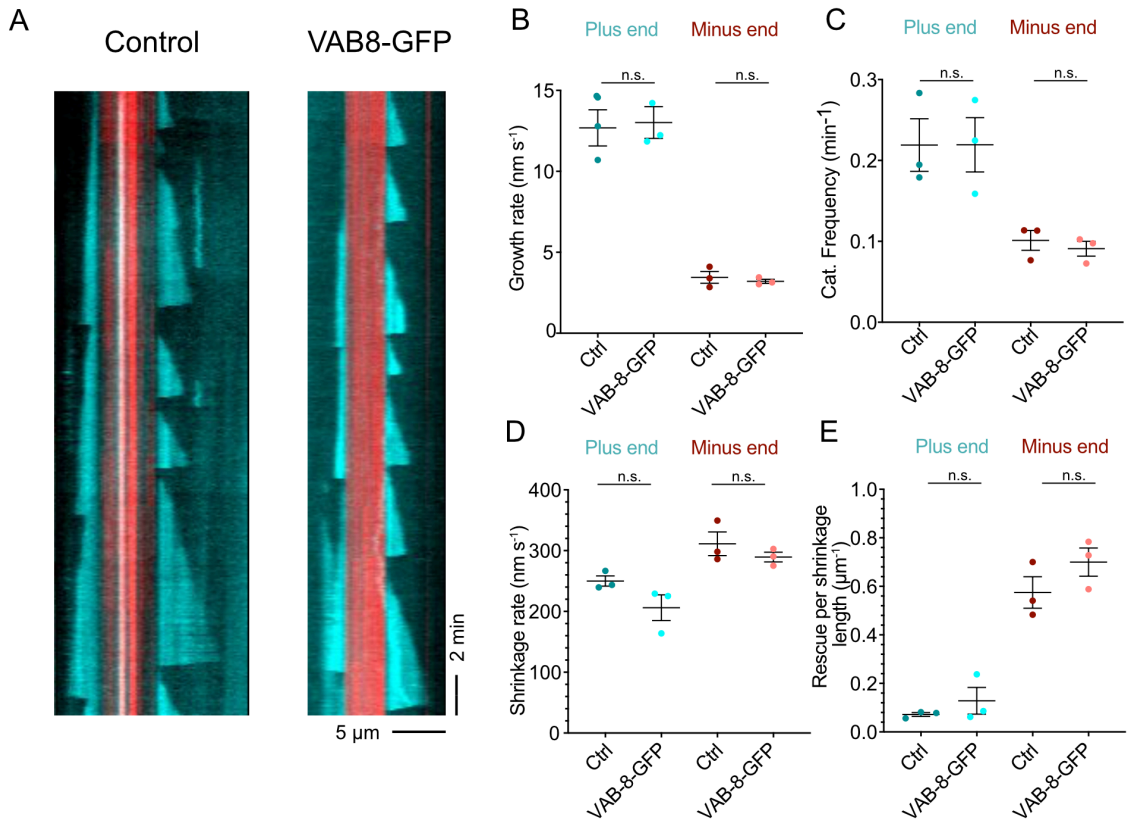

Figure A.1.2 VAB-8 does not significantly impact microtubule dynamics *in vitro*. (A) Representative kymographs from both the control and VAB-8 conditions. Minus ends are oriented to the left, and plus ends to the right. In the control, 5 µl of VAB-8 storage buffer was included in the reaction, commensurate to the volume of VAB-8-GFP protein added to the VAB-8 condition. 125 nM of VAB-8 was used. (B) Average growth rates of plus and minus ends with and without VAB-8. N = 3 independent repeats per condition. Plus end ctrl N= 619, 132, 480; Plus end VAB-8 N = 140, 213, 674. Minus end ctrl N= 289, 42, 339; Minus end VAB-8 N =133, 109, 211. Error bars are SEM. (C) Catastrophe frequency of plus and minus ends. Plus end ctrl N = 544, 123, 399; Plus end VAB-8 N=101, 192, 576. Minus end ctrl N=228, 29, 270; Minus end VAB-8 N =93, 87, 156. Error bars represent counting error. (D) Average shrinkage rate of plus and minus ends with and without VAB-8. Plus end ctrl N = 488, 104, 351; Plus end VAB-8 N = 88, 152, 509. Minus end ctrl N= 101, 8, 148; Minus end VAB-8 N =39, 32, 69. Error bars are SEM. (E) Number of rescues per shrinkage length of plus and minus ends. Plus end ctrl N = 77, 17, 104; Plus end VAB-8 N=71, 22, 118. Minus end ctrl N=110, 14, 140; Minus end VAB-8 N = 67, 50, 83. Error bars represent counting error. Multiple unpaired t-tests performed for all plus and minus end conditions. N.s. p-value ≥ 0.05.

A.1.3 Conclusions

The work in this section establishes some fundamental *in vitro* characterization of VAB-8. Consistent with the functional predictions based on the sequence of the motor, and characterizations of other kinesin-11 family members, our results demonstrate that VAB-8 is capable of binding to microtubules, and that it does not exhibit processive motility. Though these results do not directly test the ATPase activity of VAB-8, these results do support the conclusion that VAB-8 is non-catalytic and unable to hydrolyze ATP. Future work should directly measure the ATPase activity of VAB-8 to be able to more confidently conclude this. In addition to testing whether or not in fact VAB-8 is incapable of hydrolyzing ATP, it should also be definitively established whether VAB-8 binds ATP, and what the kinetics of its nucleotide biding are, perhaps in comparison to a more conventional kinesin with a catalytic motor domain. If it were able to bind different nucleotide states of ATP, would this impact the affinity of VAB-8 for binding to microtubules? At the molecular level, there is still quite a bit of characterization that could be done for VAB-8 in the future.

One mechanism by which VAB-8 could be contributing to a trafficking defect is through disrupting the microtubule network in the neuron. We wondered whether VAB-8 would autonomously regulate the microtubule dynamics *in vitro*, but we did not measure any significant difference across the four dynamic parameters at both plus and minus ends, using 125 nM VAB-8, which is over 10x higher than the concentrations of other regulatory motors (MCAK and HSET) used in Chapter 4. VAB-8 may not be able to regulate microtubule dynamics on its own; however, there may be other binding partners or cellular factors which would enhance the binding of VAB-8 to microtubules, and perhaps even target VAB-8 to the microtubule tips, where the dynamics are occurring. Indeed, Balseiro-Gomez et al. (2021) suggest a potential

functional interaction between VAB-8 and the minus-end regulatory protein Patronin (a homolog of CAMSAP). It will be critical for future studies to further explore this potential interaction, especially, *in vitro*.

Finally, another mechanism by which VAB-8 could be disrupting the trafficking of gap junctions is by blocking kinesin transport. Other proteins, such as tau, are reported to bind to microtubules, and functionally block the motility of certain kinesins (Dixit et al., 2008; Siahaan et al., 2019; Monroy et al., 2020). Since VAB-8 appears to bind microtubules, but not move processively, perhaps it is able to slow down or block to movement of other kinesins responsible for transporting gap junction material along the cell. Since VAB-8 was the only motor identified to be differentially expressed in the *unc-4* mutant, the trafficking defect is not likely due to the low expression of the transport kinesins. To measure this effect experimentally, the motility of candidate transport kinesins (such as those in the kinesin-1 or kinesin-3 family) could be compared on uncoated microtubules, versus microtubules coated with VAB-8, versus those coated in tau, as a positive control.

Summary

The network of proteins impacting the trafficking of gap junctions in the *unc-4* VA neuron is complex. Using *in vitro* approaches, we can characterize the fundamental properties of this unconventional kinesin which helps us in better defining the mechanisms by which it functions in cells. Our preliminary work in this section establishes some fundamental characteristics of VAB-8, which are crucial to lay some groundwork for other future studies.

A.1.4 Methods

A.1.4.1 Protein preparation

The 6xhis-VAB-8-GFP-Strep construct was cloned using PCR-based infusion cloning into a pFastBac-HTa vector containing an N-terminal 6xHis tag. Cloning products were verified using DNA sequencing. His-VAB-8-GFP was expressed in baculovirus-infected Sf9 insect cells using the Bac-to-Bac system according to the manufacturer's instructions (Invitrogen), similar to the method described in Lawrence et al. (2018). After the first amplification, baculovirus-infected insect cells (BIIC) stocks were prepared as previously described (Wasilko and Lee, 2006; Wasilko et al., 2009). Briefly, Sf9 insect cells were infected at a density of 1×10^6 viable cells/ml with BIIC stocks at a ratio of 10^{-4} BIIC: total culture volume. Cells were harvested 5 days after infection. Cell pellets were lysed by one freeze–thaw cycle and Dounce homogenizing in lysis buffer containing protease inhibitors; genomic DNA was subsequently sheared by passing the lysate through an 18-gauge needle. Lysis buffer consisted of 50mM HEPES (pH 7.4), 300mM NaCl, 1.5 mM $MgCl_2$, 5% glycerol, 1mM DTT, 0.5mM ATP, 1mM PMSF. Crude lysates were clarified by centrifugation for 30 min at 4°C and 35,000 rpm in a Beckman L90K Optima and 50.2 Ti rotor. Clarified lysates were applied to a HisTrapHP column (GE Lifesciences) according to the manufacturer's protocol. His-VAB-8-GFP was eluted with the following elution buffers: 50mM HEPES, 400mM NaCl, 0.1mM $MgCl_2$, 1mM DTT, 1mM PMSF, 0.5mM ATP, supplemented with either 10mM, 50mM, or 500mM imidazole depending on the elution stage. Purified VAB-8-GFP was desalted into storage buffer (10mM HEPES, 200mM KCl, 0.1mM $MgCl_2$, 0.1mM ATP, 1mM DTT, 1mM PMSF, 20% sucrose) using a PD10 column (GE Healthcare), and concentrated using an Amicon centrifugal filter, then snap frozen

in liquid nitrogen. Kip3-GFP was a gift from the Howard lab. Tubulin was prepared and purified as previously described in Chapter 2.

A.1.4.2 Taxol-stabilized seeds

Taxol-stabilized microtubules were prepared based on an adapted protocol (Elie-Caille et al., 2007). First, a microtubule polymerization mix was prepared containing 4mM $MgCl_2$, 1mM GTP, and 5% DMSO (dimethyl sulfoxide) in BRB80 to a final volume of 5µl. This mixture was vortexed briefly, and 1.25 µl of the mix was added to 5µl of 40µM tubulin, 15% labeled with rhodamine. This mixture was incubated for 1 hour at 37°C before adding 400 µl of warm BRB80 containing 10 µM Taxol (in DMSO). This was spun for 5 min at 30PSI in a Beckman airfuge. The pelleted Taxol seeds were resuspended in 100 µl of Taxol-BRB80 and kept for 1 week of experiments. Taxol-stabilized microtubules were diluted 10-20x before use in Taxol-BRB80. All subsequent reactions containing Taxol-stabilized microtubules also contained 10 µM Taxol.

A.1.4.3 Gliding assay

Coverslips and flow cells were prepared in the same way as described in Chapter 2. Channels were washed with BRB80, then 1:50 dilution of α-GFP antibody (Invitrogen) was incubated for 5 min. Subsequent washes were done with a wash buffer consisting of 1 mM ATP, 0.5 mg/ml casein, and 1mM $MgCl_2$ in BRB80. 5 µl of either VAB-8 storage buffer, 700 nM Kip-3-GFP, or 1 µM VAB-8-GFP were incubated for 3 min in the flow cell, and washed out with wash buffer. 1% Pluronic F127 was next incubated for 1 min. Finally, Taxol-stabilized rhodamine-labeled seeds were added, in a dilution of 10-20x, and washed out with antifade mix containing 40 mM D-glucose, 40 µg/ml glucose oxidase, 16 µg/ml catalase, 0.5 mg/ml casein, 10

mM dithiothreitol, and 50 mM KCl, 10μM Taxol, and 1 mM ATP in BRB80. One image of the GFP signal on the surface was taken before imaging the time lapse of the microtubules in the 561 channel at 0.2 FPS for 5 min. Two movies were taken in different fields of view in each in each reaction.

A.1.4.4 Gliding assay analysis

Microtubules were manually counted from the last frame of each movie. Only microtubules longer than 3 pixels were included. Gliding velocities were calculated from the kymographs of the Kip3 and VAB-8 movies. Points were placed at the beginning and end of a microtubule's position over time, and the rate of change was calculated.

A.1.4.5 Single molecule stepping assay

Coverslips and flow cells were prepared the same way as described previously in Chapter 2, the same way as for a dynamic assay. Rhodamine-labeled microtubules, however, were Taxol-stabilized instead of GMPCPP-stabilized. The final reaction mix consisted of antifade (same as described for the gliding assays), and various concentrations of VAB-8-GFP in BRB80. One image of the rhodamine seeds was taken in the 561 channel before each movie. Movies were imaged at 10 FPS with 100ms exposure and 100% 488-laser power for 30 seconds. Five movies were taken in different fields of view for each reaction. Kymographs were drawn over each microtubule to look at the localization of VAB-8-GFP along the lattice over time.

A.1.4.6 Dynamics assay

The dynamics assay was done the same as described previously in Chapter 2, with the following changes. The antifade mix contained 40 mM D-glucose, 40 µg/ml glucose oxidase, 16 µg/ml catalase, 0.5 mg/ml casein, 10 mM dithiothreitol, and 50 mM KCl, 1mM GTP, and 1 mM ATP in BRB80. In the control condition, 5 µl of VAB-8 storage buffer was added. In the VAB-8 condition, 5 µl of VAB-8-GFP was added to a final concentration of 125 nM. Movies were taken at 0.2 FPS for 30 min. Dynamics analysis of growth rate and catastrophe frequency was performed the same as described previously. Shrinkage rate was calculated similarly to the growth rate, by taking the difference in position of the microtubule end at catastrophe until the end of the shrinkage event- either at the seed or at a rescue point. Only shrinkage events longer than 5 pixels in distance (800nM) were calculated. Total numbers of rescues were counted for each movie and were divided by the summed shrinkage lengths from each shrinkage event during the entire movie to give a number of rescues over the total shrinkage length, rather than as a function of time. I used my custom MATLAB script to calculate all dynamics parameters from the manually placed coordinates of microtubule growth and shrinkage events seen on the kymographs.

A.2 Minus end stability after laser severing is dependent on soluble tubulin

A.2.1 Introduction

Not long after the dynamic parameters of the plus and minus ends were first characterized and directly compared to show that minus ends were indeed both slower growing and more stable (Walker et al., 1988), another unique observation regarding minus ends was made. In this study, microtubules *in vitro* were cut in two by UV microbeam. Contrary to their predictions that both ends of the unstable microtubule lattice would immediately shrink after being cut, the authors observed that while the newly formed plus ends did in fact shrink after the cut was made, the minus ends remained stable (Walker et al., 1989).

Another study repeated these experiments, and tested more conditions, by comparing severing by UV microbeam irradiation and mechanical severing by a glass microneedle, as well as varying the tubulin concentrations and buffer conditions (Tran et al., 1997). Consistent with the previous study, it was observed that the vast majority of newly created minus ends after severing with wither the UV microbeam or the glass microneedle remained stable, while nearly every plus end depolymerized (Tran et al., 1997). In the presence of GMPCPP, all newly formed plus and minus ends after severing remained stable (Tran et al., 1997). When the authors doubled the concentration of tubulin from 16 μM to 32 μM in solution, a slightly higher percentage of plus ends remained stable (0.7% to 9%), but there was a more dramatic increase of the percentage of stable minus ends (78% to 97%) (Tran et al., 1997). Other more recent studies that use laser cutting of microtubules *in vitro* also observe that minus ends tend to remain stable while plus ends do not, although the reason behind this phenomenon is still not fully understood

(Jiang et al., 2014; Vemu et al., 2018). We were interested in repeating this assay and trying novel conditions to better understand the mechanism of minus end stability in this context.

A.2.2 Results

A.2.2.1 Minus end stability after laser severing is dependent on tubulin in solution

One proposed explanation for the stability of minus ends following laser severing is the existence of a metastable intermediate kinetic state between growth and shrinkage that differs at the two ends (Tran et al., 1997). In this model, minus ends may lose their GTP cap, and exist in this metastable cap-less state, before being able to regain their cap and resume growth, rather than immediately undergoing catastrophe. Plus ends, on the other hand, would rarely exist in this metastable state, and rather, if their cap is lost, they are much more likely to quickly pass through the metastable state and start shrinking (Tran et al., 1997). We were interested in testing whether minus-end stability was dependent on the amount of soluble tubulin in solution, which would indicate whether minus ends are inherently structurally stable and not dependent on the availability of soluble tubulin, or rather, they are indeed able to recap quickly after severing.

To test this, we compared the post-severing behavior of microtubule ends in the presence of 10 μM tubulin, versus 0 μM soluble tubulin. For the condition in which tubulin was present, dynamic microtubule extensions were grown similarly to previous experiments, the chamber was kept at steady state conditions, and they were severed with a 405 nm laser controlled with a mini-scanner, to specify which pixels in the field of view to ablate. A 1-pixel-wide line was drawn perpendicular to each microtubule where the ablation would occur, and the microtubule was imaged before and after the ablation. Methylcellulose was used in the buffer solution to prevent the drifting of the unattached microtubule end containing the newly formed minus end.

Consistent with the previous studies, in the presence of 10μM tubulin, nearly all plus ends depolymerized, while the majority of minus ends remained stable (Figure A.2.1A-B). In order to test the stability of microtubules ablated in the absence of tubulin, we grew dynamic microtubules with 10 μM tubulin, and capped these microtubules with GMPCPP-tubulin, and removed soluble tubulin from solution. Interestingly, we found that both plus and minus ends tended to undergo shrinkage after ablation in these conditions (Figure A.2.1A-B). This stark contrast between the stability of minus ends in the presence versus absence of tubulin indicates that the tubulin is essential for the stability of newly formed minus ends.

We also measured the time to catastrophe in the 0 μM tubulin condition and did not see any clear differences between the two ends; rather, there was more variability between repeats than between the two ends (Figure A.2.1C). We also measured the depolymerization rate of the two ends following ablation and found that minus ends exhibited a significantly higher shrinkage rate than plus ends (Figure A.2.1D). Previous studies have also reported higher shrinkage rates of minus ends compared to plus ends, but these were typically done in standard dynamics conditions, in the presence of soluble tubulin (Walker et al., 1988; O'Brien et al., 1990; Trinczek et al., 1993). It is not thought that shrinkage rate is dependent on the tubulin concentration in solution, but this has not been thoroughly investigated.

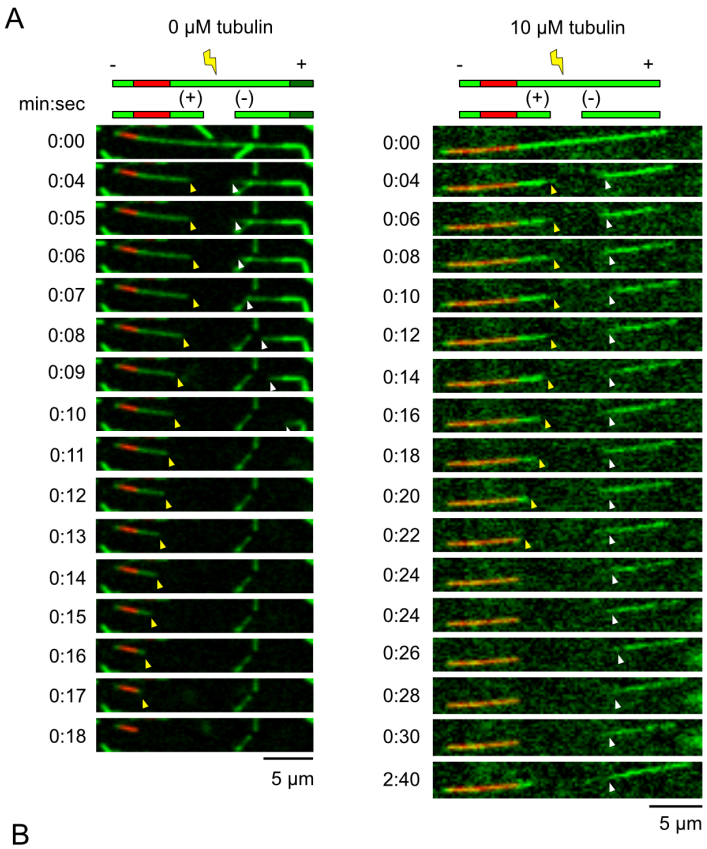
A
0 μM tubulin
10 μM tubulin
min:sec
(+)
(-)
0:00
0:04
0:05
0:06
0:07
0:08
0:09
0:10
0:11
0:12
0:13
0:14
0:15
0:16
0:17
0:18
0:00
0:04
0:06
0:08
0:10
0:12
0:14
0:16
0:18
0:20
0:22
0:24
0:24
0:26
0:28
0:30
2:40
5 μm
5 μm

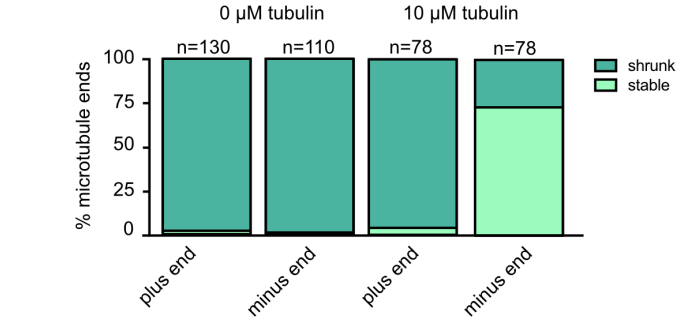
B
0 μM tubulin
10 μM tubulin
n=130
n=110
n=78
n=78
% microtubule ends
100
75
50
25
0
shrunk
stable
plus end
minus end
plus end
minus end

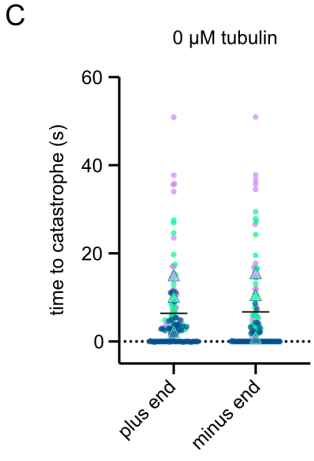
C
0 μM tubulin
time to catastrophe (s)
60
40
20
0
plus end
minus end

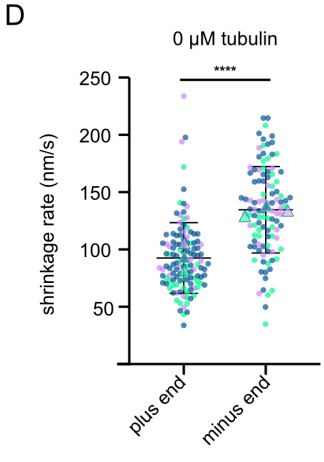
D
0 μM tubulin
****
shrinkage rate (nm/s)
250
200
150
100
50
plus end
minus end

Figure A.2.1 Post-ablation minus-end stability is dependent on soluble tubulin. (A) Representative time lapse images from microtubule ablation in the presence or absence of soluble tubulin. Timestamp indicates time from beginning of the movie, and ablation occurs between the 0:00s and 0:04s time. Orientation of the plus and minus ends are indicated. Newly formed plus ends are tracked with a yellow arrowhead, and newly formed minus ends are tracked with a white arrowhead. (B) Percentage of plus and minus ends in each tubulin condition that were classified as either shrunk or stable, post ablation. Unknown end behavior was not included in this calculation (See methods). (C) Time to catastrophe for each microtubule end in the 0 μM tubulin condition. Each repeat is color coded purple, teal, or dark blue. Mean from each repeat is indicated by the triangle points. (D) Shrinkage rate for each microtubule end in the 0 μM tubulin condition. Each repeat is color coded purple, teal, or dark blue. Mean from each repeat is indicated by the triangle points. Welch's t-test was performed on the pooled plus and minus end data points. P-value **** ≤0.0001.

A.2.3 Conclusions

Our results provide some additional mechanistic insight to this puzzling observation of post-ablation minus-end stability. Previous studies performed laser severing of microtubules in the presence of tubulin; severing microtubules in the absence of soluble provides us with a novel result. While we observed that the majority of minus ends in the presence of tubulin remained stable and did not undergo shrinkage, they were equally as unstable as plus ends in the absence of tubulin. This suggests that tubulin is a key mechanistic component to their stability. This result would be consistent with the model proposed by Tran et al. (1997), in which minus ends had an intermediate kinetic state that enabled them to more easily bypass immediately undergoing shrinkage, and instead remain stable. Our result is also consistent with our previous data in Chapter 3 indicating that minus ends have a small but stable cap. In tubulin dilution experiments, minus ends had relatively short delay times compared to the plus ends in the same conditions, which was proportional to their slow growth prior to dilution. Following tubulin dilution, minus ends were not stable, and underwent catastrophe, due to the loss of the GTP-cap and the absence of tubulin that would allow them to maintain growth. Of course, the end structure of the microtubule tip in the tubulin dilution presumably has a GTP-cap prior to

dilution, while the newly formed plus and minus ends after ablation consist of GDP-tubulin in the lattice conformation. It is expected that the GDP-tubulin in the lattice is in an unstable state, and immediately shrinks at the plus end; but it is puzzling how the minus end does not immediately behave the same way. The tubulin on-rate at the minus end is slower than at the plus end, so it is not clear how the minus end may be rapidly re-capped by GTP-tubulin faster than the plus end, in order to prevent shrinkage. Either there is a component of the metastable kinetic state that enables minus-end stability in the absence of a GTP-cap, or perhaps the minimum cap size needed for stability is much lower for the minus end than the plus end. Both of these ideas are possible, considering that dynamic minus ends are stabilized by small caps that are not easily removable (Strothman et al., 2019).

Another interesting observation is our measurement of the shrinkage rate between the two ends. Although these measurements were made in the absence of tubulin, they are consistent with other reports comparing the shrinkage rates of the two ends, which show that, typically, minus ends have faster shrinkage rates (Walker et al., 1988; O'Brien et al., 1990; Arpag et al., 2020). This is another puzzling phenomenon, as it would imply that the lattice in the minus-end orientation is more unstable than in the plus-end direction, although minus ends are more stable than plus ends in other contexts. The shrinkage phase of microtubules has not been studied in depth to the degree of other dynamic phases, such as growth and catastrophe, so it remains possible that there are aspects to the process of shrinkage that we do not fully understand. For example, are there differences in shrinkage rates between microtubules grown in different conditions, such as with different concentrations of soluble tubulin? Perhaps shrinkage rates are affected by microtubule lattice defects, such as mismatched protofilament numbers and holes, as well as GTP-tubulin-islands that arise from lattice repair (Aumeier et al., 2016; Schaedel et al.,

2015; Vemu et al., 2018; Tropini et al., 2012; de Forges et al., 2016). Overall, these results indicate that minus-end stability is dependent on the presence of tubulin in solution, which provides further insight into the mechanisms of minus-end stability.

A.2.4 Methods

A.2.4.1 Reaction mix preparation

Flow cells were prepared as described previously in Chapter 2. Rhodamine-labeled GMPCPP seeds were attached to the coverslip with anti-rhodamine antibody. For the 10 μM tubulin condition, dynamic microtubule extensions were grown off the seeds for 15 minutes using a reaction mix containing 10μM tubulin, 10% labeled with Alexa Fluor-488, 40 mM D-glucose, 40 μg/ml glucose oxidase, 16 μg/ml catalase, 0.08 mg/ml casein, 10 mM dithiothreitol, and 50 mM KCl, 1mM GTP, and 0.1% methylcellulose in BRB80. The channel was sealed with valap (1:1:1 ratio of lanolin, paraffin wax, and Vaseline) to prevent dehydration. For the 0 μM tubulin condition, dynamic microtubules were grown identically to the 10 μM condition, except that after 15 minutes of growth, they were capped with GMPCPP-tubulin (6 μM tubulin, 20% labeled with Alexa Fluor-488, 0.5mM GMPCPP) for 5 minutes, before washing out with the same antifade mix with methylcellulose, but without soluble tubulin. The channel was also sealed with valap before imaging.

A.2.4.2 Imaging conditions

Imaging was done using a Nikon spinning disk confocal microscope in the Nikon Center of Excellence using a 60x objective. Laser ablation was performed using 100 mW 405 nm laser controlled by a Bruker mini-scanner. The ablation region of interest was selected to be 1 pixel

wide, approximately 10 pixels long, perpendicular to the microtubule of interest. Ablation was performed on long plus end extensions. The laser dwell time was set at 100 μs at 100% power, looping through each pixel of the selected ablation region for 1 second in total. One frame was taken in the 561 channel to capture the seeds, then images in the 488-channel were acquired for 4s at 0.5 FPS, the ablation took place, then the rest of the movie was imaged- for the 0 μM condition, imaging was done at 1FPS for 5 min, unless both microtubule ends depolymerized, in which case the move was ended before 5 min. For the 10 μM tubulin condition, imaging was done at 0.5 FPS for 60 sec, then 0.1 FPS for 5 min.

A.2.4.3 Image analysis

Movies were background subtracted using rolling ball average, 25 pixel radius. The seed image was merged with the rest of the time lapse. Movies were cropped to analyze the individual ablated microtubule. The newly formed end closest to the seed was considered to be the plus end, and the other newly formed end on the now unanchored microtubule extension was considered to be the minus end. Behavior after severing was classified as **shrunk** (where the end immediately depolymerized after severing), **stable** (where the end either paused and/or began regrowth after severing), or **unknown**. The unknown events included events such as: 1) a plus end depolymerizing through a newly formed unanchored minus end, 2) it was unclear whether a successful cut was made with the laser (i.e., the whole extension moved in unison, as if it was only bleached and not cut), or 3) the unanchored end floated away. Only events where it was clear that the laser had indeed formed two new ends, and the ends could be clearly tracked and classified (even if only one end was analyzable) were included in the data set. Three repeats were performed for each condition on different days. These data were pooled into the final data. Time

to catastrophe and shrinkage rates were calculated by kymograph analysis. Time to catastrophe was calculated from measuring the time from the first frame post-ablation to the point of catastrophe. Microtubules that started shrinking immediately post-ablation were counted as a 0 timepoint. Shrinkage rates were measured from the slope of the shrinkage on the kymograph.

References

Ahmad, F.J., W. Yu, F.J. McNally, and P.W. Baas. 2000. An essential role for katanin in severing microtubules in the neuron. *J. Cell Biol.* 145:305–315. doi:10.1083/jcb.145.2.305.

Akhmanova, A., and C.C. Hoogenraad. 2015. Microtubule Minus-End-Targeting Proteins. *Curr. Biol.* 25:R162–R171. doi:10.1016/j.cub.2014.12.027.

Akhmanova, A., and M.O. Steinmetz. 2015. Control of microtubule organization and dynamics: Two ends in the limelight. *Nat. Rev. Mol. Cell Biol.* 16:711–726. doi:10.1038/nrm4084.

Alberts, B., A. Johnson, J. Lewis, M. Raff, K. Roberts, and P. Walter. 2008. Molecular BAlberts, B., A. Johnson, J. Lewis, M. Raff, K. Roberts, and P. Walter. 2008. Molecular Biology of the Cell. 5th Editio. New York.iology of the Cell. 5th Editio. New York.

Alfaro-Aco, R., A. Thawani, and S. Petry. 2017. Structural analysis of the role of TPX2 in branching microtubule nucleation. *J. Cell Biol.* 216:983–997. doi:10.1083/jcb.201607060.

Almada, E., F.M. Tonucci, F. Hidalgo, A. Ferretti, S. Ibarra, A. Pariani, R. Vena, C. Favre, J. Girardini, A. Kierbel, and M.C. Larocca. 2017. Akap350 Recruits Eb1 to the Spindle Poles, Ensuring Proper Spindle Orientation and Lumen Formation in 3d Epithelial Cell Cultures. *Sci. Rep.* 7:1–15. doi:10.1038/s41598-017-14241-y.

Alushin, G.M., G.C. Lander, E.H. Kellogg, R. Zhang, D. Baker, and E. Nogales. 2014. High-Resolution microtubule structures reveal the structural transitions in αβ-tubulin upon GTP hydrolysis. *Cell*. 157:1117–1129. doi:10.1016/j.cell.2014.03.053.

Arpag, G., E.J. Lawrence, V.J. Farmer, S.L. Hall, and M. Zanic. 2020. Collective effects of XMAP215, EB1, CLASP2, and MCAK lead to robust microtubule treadmilling. *Proc. Natl.*

Acad. Sci. U. S. A. 117:12847–12855. doi:10.1073/pnas.2003191117.

Atherton, J., K. Jiang, M.M. Stangier, Y. Luo, S. Hua, K. Houben, J.J.E. van Hooff, A.-P. Joseph, G. Scarabelli, B.J. Grant, A.J. Roberts, M. Topf, M.O. Steinmetz, M. Baldus, C.A. Moores, and A. Akhmanova. 2017. A structural model for microtubule minus-end recognition and protection by CAMSAP proteins. *Nat. Struct. Mol. Biol.* 24:931–943. doi:10.1038/nsmb.3483.

Atherton, J., M. Stouffer, F. Francis, and C.A. Moores. 2018. Microtubule architecture in vitro and in cells revealed by cryo-electron tomography. *Acta Crystallogr. Sect. D Struct. Biol.* 74:572–584. doi:10.1107/S2059798318001948.

Aumeier, C., L. Schaedel, J. Gaillard, K. John, L. Blanchoin, and M. Théry. 2016. Self-repair promotes microtubule rescue. *Nat. Cell Biol.* 18:1054–1064. doi:10.1038/ncb3406.

Ayaz, P., S. Munyoki, E.A. Geyer, F.A. Piedra, E.S. Vu, R. Bromberg, Z. Otwinowski, N. V. Grishin, C.A. Brautigam, and L.M. Rice. 2014. A tethered delivery mechanism explains the catalytic action of a microtubule polymerase. *Elife*. 3:1–19. doi:10.7554/eLife.03069.

Ayaz, P., X. Ye, P. Huddleston, C.A. Brautigam, and L.M. Rice. 2012. A TOG:αβ-tubulin complex structure reveals conformation-based mechanisms for a microtubule polymerase. *Science (80-.).* 337:857–860. doi:10.1126/science.1221698.

Ayukawa, R., S. Iwata, H. Imai, S. Kamimura, M. Hayashi, K.X. Ngo, I. Minoura, S. Uchimura, T. Makino, M. Shirouzu, H. Shigematsu, K. Sekimoto, B. Gigant, and E. Muto. 2021. GTP-dependent formation of straight tubulin oligomers leads to microtubule nucleation. *J. Cell Biol.* 220. doi:10.1083/JCB.202007033.

Balseiro-Gómez, S., Y. Yue, L. Shao, S. Çetinkaya, C. Kuzoian, K.J. Verhey, and S. Yogev. 2021. Neurexin and Frizzled signaling intercept axonal-transport at microtubule minus-ends

to control synapse formation. *bioRxiv*. 2021.03.22.436477. doi:10.1101/2021.03.22.436477.

Ben-Ze'ev, A., S.R. Farmer, and S. Penman. 1979. Mechanisms of regulating tubulin synthesis in cultured mammalian cells. *Cell*. 17:319–325. doi:10.1016/0092-8674(79)90157-0.

Benoit, M.P.M.H., A.B. Asenjo, and H. Sosa. 2018. Cryo-EM reveals the structural basis of microtubule depolymerization by kinesin-13s. *Nat. Commun.* 9:1662. doi:10.1038/s41467-018-04044-8.

Bergen, L.G., and G.G. Borisy. 1980. Head-to-tail polymerization of microtubules in vitro. Electron microscope analysis of seeded assembly. *J. Cell Biol.* 84:141–150. doi:10.1083/jcb.84.1.141.

Best, R.L., N.E. LaPointe, J. Liang, K. Ruan, M.F. Shade, L. Wilson, and S.C. Feinstein. 2019. Tau isoform-specific stabilization of intermediate states during microtubule assembly and disassembly. *J. Biol. Chem.* 294:12265–12280. doi:10.1074/jbc.RA119.009124.

Bieling, P., L. Laan, H. Schek, E.L. Munteanu, L. Sandblad, M. Dogterom, D. Brunner, and T. Surrey. 2007. Reconstitution of a microtubule plus-end tracking system in vitro. *Nature*. 450:1100–1105. doi:10.1038/nature06386.

Bodakuntla, S., A.S. Jijumon, C. Villablanca, C. Gonzalez-Billault, and C. Janke. 2019. Microtubule-Associated Proteins: Structuring the Cytoskeleton. *Trends Cell Biol.* 29:804–819. doi:10.1016/j.tcb.2019.07.004.

Borisy, G.G., and E.W. Taylor. 1967a. The mechanism of action of colchicine. Colchicine binding to sea urchin eggs and the mitotic apparatus. *J. Cell Biol.* 34:535–548. doi:10.1083/jcb.34.2.535.

Borisy, G.G., and E.W. Taylor. 1967b. The mechanism of action of colchicine. Binding of colchincine-3H to cellular protein. *J. Cell Biol.* 34:525–533. doi:10.1083/jcb.34.2.525.

Bowne-Anderson, H., M. Zanic, M. Kauer, and J. Howard. 2013. Microtubule dynamic instability: A new model with coupled GTP hydrolysis and multistep catastrophe. *BioEssays*. 35:452–461. doi:10.1002/bies.201200131.

Braun, M., Z. Lansky, S. Bajer, G. Fink, A.A. Kasprzak, and S. Diez. 2013. The human kinesin-14 HSET tracks the tips of growing microtubules in vitro. *Cytoskeleton*. 70:515–521. doi:10.1002/cm.21133.

Brouhard, G.J., and L.M. Rice. 2014. The contribution of αβ-tubulin curvature to microtubule dynamics. *J. Cell Biol.* 207:323–334. doi:10.1083/jcb.201407095.

Brouhard, G.J., J.H. Stear, T.L. Noetzel, J. Al-Bassam, K. Kinoshita, S.C. Harrison, J. Howard, and A.A. Hyman. 2008. XMAP215 Is a Processive Microtubule Polymerase. *Cell*. doi:10.1016/j.cell.2007.11.043.

Buey, R.M., J. Fernando Díaz, and J.M. Andreu. 2006. The nucleotide switch of tubulin and microtubule assembly: A polymerization-driven structural change. *Biochemistry*. 45:5933–5938. doi:10.1021/bi060334m.

Cai, S., L.N. Weaver, S.C. Ems-McClung, and C.E. Walczak. 2009. Kinesin-14 Family Proteins HSET/XCTK2 Control Spindle Length by Cross-Linking and Sliding Microtubules. *Mol. Biol. Cell*. 20:1348–1359. doi:10.1091/mbc.e08-09-0971.

Cai, S., L.N. Weaver, S.C. Ems-McClung, and C.E. Walczak. 2010. Proper Organization of Microtubule Minus-Ends is Needed for Midzone Stability and Cytokinesis. *Curr. Biol.* 20:880. doi:10.1016/j.cub.2010.03.067.

Cao, Y., J. Lipka, R. Stucchi, M. Burute, X. Pan, S. Portegies, R. Tas, J. Willems, L. Will, H. MacGillavry, M. Altelaar, L.C. Kapitein, M. Harterink, and C.C. Hoogenraad. 2020. Microtubule Minus-End Binding Protein CAMSAP2 and Kinesin-14 Motor KIFC3 Control

Dendritic Microtubule Organization. *Curr. Biol.* doi:10.1016/j.cub.2019.12.056.

Caplow, M., and J. Shanks. 1996. Evidence that a single monolayer tubulin-GTP cap is both necessary and sufficient to stabilize microtubules. *Mol. Biol. Cell*. 7:663–675. doi:10.1091/mbc.7.4.663.

Carlier, M.F., and D. Pantaloni. 1981. Kinetic Analysis of Guanosine 5'-Triphosphate Hydrolysis Associated with Tubulin Polymerization. *Biochemistry*. 20:1918–1924. doi:10.1021/bi00510a030.

Case, R.B., D.W. Pierce, N. Hom-Booher, C.L. Hart, and R.D. Vale. 1997. The directional preference of kinesin motors is specified by an element outside of the motor catalytic domain. *Cell*. 90:959–966. doi:10.1016/S0092-8674(00)80360-8.

Castoldi, M., and A. V. Popov. 2003. Purification of brain tubulin through two cycles of polymerization- depolymerization in a high-molarity buffer. *Protein Expr. Purif.* 32:83–88. doi:10.1016/S1046-5928(03)00218-3.

Chaaban, S., S. Jariwala, C.T. Hsu, S. Redemann, J.M. Kollman, T. Müller-Reichert, D. Sept, K.H. Bui, and G.J. Brouhard. 2018. The Structure and Dynamics of C. elegans Tubulin Reveals the Mechanistic Basis of Microtubule Growth. *Dev. Cell*. 47:191-204.e8. doi:10.1016/j.devcel.2018.08.023.

Chan, J., G. Calder, S. Fox, and C. Lloyd. 2005. Localization of the microtubule end binding protein EB1 reveals alternative pathways of spindle development in Arabidopsis suspension cells. *Plant Cell*. 17:1737–1748. doi:10.1105/tpc.105.032615.

Chavali, P.L., G. Chandrasekaran, A.R. Barr, P. Tátrai, C. Taylor, E.K. Papachristou, C.G. Woods, S. Chavali, and F. Gergely. 2016. A CEP215-HSET complex links centrosomes with spindle poles and drives centrosome clustering in cancer. *Nat. Commun.* 7:1–16.

doi:10.1038/ncomms11005.

Chen, G.-Y., J.M. Cleary, A.B. Asenjo, Y. Chen, J.A. Mascaro, D.F.J. Arginteanu, H. Sosa, and W.O. Hancock. 2019. Kinesin-5 Promotes Microtubule Nucleation and Assembly by Stabilizing a Lattice-Competent Conformation of Tubulin. *Curr. Biol.* 29:2259-2269.e4. doi:10.1016/J.CUB.2019.05.075.

Cleveland, D.W. 1989. Autoregulated control of tubulin synthesis in animal cells. *Curr. Opin. Cell Biol.* 1:10–14. doi:10.1016/S0955-0674(89)80030-4.

Cleveland, D.W., M.A. Lopata, P. Sherline, and M.W. Kirschner. 1981. Unpolymerized tubulin modulates the level of tubulin mRNAs. *Cell*. 25:537–546. doi:10.1016/0092-8674(81)90072-6.

Dammermann, A., A. Desai, and K. Oegema. 2003. The minus end in sight. *Curr. Biol.* 13. doi:10.1016/S0960-9822(03)00530-X.

de Forges, H., A. Pilon, I. Cantaloube, A. Pallandre, A.-M. Haghiri-Gosnet, F. Perez, and C. Poüs. 2016. Localized Mechanical Stress Promotes Microtubule Rescue.

Desai, A., and T.J. Mitchison. 1997. MICROTUBULE POLYMERIZATION DYNAMICS. *Annu. Rev. Cell Dev. Biol.* 13:83–117. doi:10.1146/annurev.cellbio.13.1.83.

Desai, A., S. Verma, T.J. Mitchison, and C.E. Walczak. 1999. Kin I kinesins are microtubule-destabilizing enzymes. *Cell*. 96:69–78. doi:10.1016/S0092-8674(00)80960-5.

Dixit, R., J.L. Ross, Y.E. Goldman, and E.L.F. Holzbaur. 2008. Differential Regulation of Dynein and Kinesin Motor Proteins by Tau. *Science (80-.).* 319:1086–1089. doi:10.1126/science.1152993.

Domnitz, S.B., M. Wagenbach, J. Decarreau, and L. Wordeman. 2012. MCAK activity at microtubule tips regulates spindle microtubule length to promote robust kinetochore

attachment. *J. Cell Biol.* 197:231–237. doi:10.1083/jcb.201108147.

Drechsel, D.N., A.A. Hyman, M.H. Cobb, and M.W. Kirschner. 1992. Modulation of the dynamic instability of tubulin assembly by the microtubule-associated protein tau. *Mol. Biol. Cell*. 3:1141–1154. doi:10.1091/mbc.3.10.1141.

Drechsel, D.N., and M.W. Kirschner. 1994. The minimum GTP cap required to stabilize microtubules. *Curr. Biol.* 4:1053–1061. doi:10.1016/S0960-9822(00)00243-8.

Duellberg, C., N.I. Cade, D. Holmes, and T. Surrey. 2016a. The size of the EB cap determines instantaneous microtubule stability. *Elife*. 5:e13470. doi:10.7554/eLife.13470.

Duellberg, C., N.I. Cade, and T. Surrey. 2016b. Microtubule aging probed by microfluidics-assisted tubulin washout. *Mol. Biol. Cell*. 27:3563–3573. doi:10.1091/mbc.e16-07-0548.

Efimov, A., A. Kharitonov, N. Efimova, J. Loncarek, P.M. Miller, N. Andreyeva, P. Gleeson, N. Galjart, A.R.R. Maia, I.X. McLeod, J.R. Yates, H. Maiato, A. Khodjakov, A. Akhmanova, and I. Kaverina. 2007. Asymmetric CLASP-Dependent Nucleation of Noncentrosomal Microtubules at the trans-Golgi Network. *Dev. Cell*. 12:917–930. doi:10.1016/j.devcel.2007.04.002.

Elie-Caille, C., F. Severin, J. Helenius, J. Howard, D.J. Muller, and A.A. Hyman. 2007. Straight GDP-Tubulin Protofilaments Form in the Presence of Taxol. *Curr. Biol.* 17:1765–1770. doi:10.1016/j.cub.2007.08.063.

Ems-McClung, S.C., M. Emch, S. Zhang, S. Mahnoor, L.N. Weaver, and C.E. Walczak. 2020. RanGTP induces an effector gradient of XCTK2 and importin α/β for spindle microtubule cross-linking. *J. Cell Biol.* 219. doi:10.1083/jcb.201906045.

Endow, S.A., and H. Higuchi. 2000. A mutant of the motor protein kinesin that moves in both directions on microtubules. *Nature*. 406:913–916. doi:10.1038/35022617.

Fan, J., A.D. Griffiths, A. Lockhart, R.A. Cross, and L.A. Amos. 1996. Microtubule Minus Ends can be Labelled with a Phage Display Antibody Specific to Alpha-Tubulin. *J. Mol. Biol.* 259:325–330. doi:10.1006/JMBI.1996.0322.

Farmer, V., G. Arpağ, S. Hall, and M. Zanic. 2020. XMAP215 promotes microtubule catastrophe by disrupting the growing microtubule end. *bioRxiv*. 2020.12.29.424748. doi:10.1101/2020.12.29.424748.

Feng, C., P. Thyagarajan, M. Shorey, D.Y. Seebold, A.T. Weiner, R.M. Albertson, K.S. Rao, A. Sagasti, D.J. Goetschius, and M.M. Rolls. 2019. Patronin-mediated minus end growth is required for dendritic microtubule polarity. *J. Cell Biol.* jcb.201810155. doi:10.1083/jcb.201810155.

Fink, G., L. Hajdo, K.J. Skowronek, C. Reuther, A.A. Kasprzak, and S. Diez. 2009. The mitotic kinesin-14 Ncd drives directional microtubule-microtubule sliding. *Nat. Cell Biol.* 11:717–723. doi:10.1038/ncb1877.

Fu, X., Y. Zhu, B. Zheng, Y. Zou, C. Wang, P. Wu, J. Wang, H. Chen, P. Du, B. Liang, and L. Fang. 2018. KIFC1, a novel potential prognostic factor and therapeutic target in hepatocellular carcinoma. *Int. J. Oncol.* 52:1912–1922. doi:10.3892/ijo.2018.4348.

Gard, D.L., and M.W. Kirschner. 1987. A microtubule-associated protein from Xenopus eggs that specifically promotes assembly at the plus-end. *J. Cell Biol.* 105:2203–2215. doi:10.1083/jcb.105.5.2203.

Gardner, M.K., B.D. Charlebois, I.M. Jánosi, J. Howard, A.J. Hunt, and D.J. Odde. 2011a. Rapid microtubule self-assembly kinetics. *Cell*. 146:582–592. doi:10.1016/j.cell.2011.06.053.

Gardner, M.K., M. Zanic, C. Gell, V. Bormuth, and J. Howard. 2011b. Depolymerizing kinesins Kip3 and MCAK shape cellular microtubule architecture by differential control of

catastrophe. *Cell*. 147:1092–1103. doi:10.1016/j.cell.2011.10.037.

Gell, C., V. Bormuth, G.J. Brouhard, D.N. Cohen, S. Diez, C.T. Friel, J. Helenius, B. Nitzsche, H. Petzold, J. Ribbe, E. Schäffer, J.H. Stear, A. Trushko, V. Varga, P.O. Widlund, M. Zanic, and J. Howard. 2010. Microtubule dynamics reconstituted in vitro and imaged by single-molecule fluorescence microscopy. *In* Methods in Cell Biology. 221–245.

Gell, C., C.T. Friel, B. Borgonovo, D.N. Drechsel, A.A. Hyman, and J. Howard. 2011. Purification of tubulin from porcine brain. *Methods Mol. Biol.* 777:15–28. doi:10.1007/978-1-61779-252-6_2.

Gigant, B., P.A. Curmi, C. Martin-Barbey, E. Charbaut, S. Lachkar, and L. Lebeau. 2000. The 4 Å X-Ray Structure of a Tubulin:Stathmin-like Domain Complex. *Cell*. 102:809–816.

Goodwin, S.S., and R.D. Vale. 2010. Patronin Regulates the Microtubule Network by Protecting Microtubule Minus Ends. *Cell*. 143:263–274. doi:10.1016/j.cell.2010.09.022.

Hazan, J., N. Fonknechten, D. Mavel, C. Paternotte, D. Samson, F. Artiguenave, C.S. Davoine, C. Cruaud, A. Dürr, P. Wincker, P. Brottier, L. Cattolico, V. Barbe, J.M. Burgunder, J.F. Prud'homme, A. Brice, B. Fontaine, R. Heilig, and J. Weissenbach. 1999. Spastin, a new AAA protein, is altered in the most frequent form of autosomal dominant spastic paraplegia. *Nat. Genet.* 23:296–303. doi:10.1038/15472.

Helenius, J., G. Brouhard, Y. Kalaidzidis, S. Diez, and J. Howard. 2006. The depolymerizing kinesin MCAK uses lattice diffusion to rapidly target microtubule ends. *Nature*. 441:115–119. doi:10.1038/nature04736.

Hendershott, M.C., and R.D. Vale. 2014. Regulation of microtubule minus-end dynamics by CAMSAPs and Patronin. *Proc. Natl. Acad. Sci.* 111:5860–5865. doi:10.1073/pnas.1404133111.

Henningsen, U., and M. Schliwa. 1997. Reversal in the direction of movement of a molecular motor. *Nature*. 389:93–96. doi:10.1038/38022.

Hentrich, C., and T. Surrey. 2010. Microtubule organization by the antagonistic mitotic motors kinesin-5 and kinesin-14. *J. Cell Biol.* 189:465–480. doi:10.1083/jcb.200910125.

Hepperla, A.J., P.T. Willey, C.E. Coombes, B.M. Schuster, M. Gerami-Nejad, M. McClellan, S. Mukherjee, J. Fox, M. Winey, D.J. Odde, E. O'Toole, and M.K. Gardner. 2014. Minus-end-directed kinesin-14 motors align antiparallel microtubules to control metaphase spindle length. *Dev. Cell*. 31:61–72. doi:10.1016/j.devcel.2014.07.023.

Hirokawa, N., S. Niwa, and Y. Tanaka. 2010. Molecular Motors in Neurons: Transport Mechanisms and Roles in Brain Function, Development, and Disease. *Neuron*. 68:610–638. doi:10.1016/J.NEURON.2010.09.039.

Horio, T., and H. Hotani. 1986. Visualization of the dynamic instability of individual microtubules by dark-field microscopy. *Nature*. 321:605–607. doi:10.1038/321605a0.

Hunter, A.W., M. Caplow, D.L. Coy, W.O. Hancock, S. Diez, L. Wordeman, and J. Howard. 2003. The kinesin-related protein MCAK is a microtubule depolymerase that forms an ATP-hydrolyzing complex at microtubule ends. *Mol. Cell*. 11:445–57.

Hyman, A., D. Drechsel, D. Kellogg, S. Salser, K. Sawin, P. Steffen, L. Wordeman, and T. Mitchison. 1991. Preparation of modified tubulins. *Methods Enzymol.* 196:478–485. doi:10.1016/0076-6879(91)96041-O.

Hyman, A.A., S. Salser, D.N. Drechsel, N. Unwin, and T.J. Mitchison. 1992. Role of GTP hydrolysis in microtubule dynamics: information from a slowly hydrolyzable analogue, GMPCPP. *Mol. Biol. Cell*. 3:1155–67. doi:10.1091/mbc.E12-03-0186.

Inoué, S., and H. Sato. 1967. Cell Motility by Labile Association of Molecules: The nature of

mitotic spindle fibers and their role in chromosome movement. *J. Gen. Physiol.* 50:259–292.

Jiang, K., S. Hua, R. Mohan, I. Grigoriev, K.W. Yau, Q. Liu, E.A. Katrukha, A.F.M. Altelaar, A.J.R. Heck, C.C. Hoogenraad, and A. Akhmanova. 2014. Microtubule Minus-End Stabilization by Polymerization-Driven CAMSAP Deposition. *Dev. Cell*. 28:295–309. doi:10.1016/j.devcel.2014.01.001.

Jiang, K., L. Rezabkova, S. Hua, Q. Liu, G. Capitani, A.F.M. Altelaar, A.J.R. Heck, R.A. Kammerer, M.O. Steinmetz, and A. Akhmanova. 2017. Microtubule minus-end regulation at spindle poles by an ASPM–katanin complex. *Nat. Cell Biol.* 19:480.

Kapitein, L.C., and C.C. Hoogenraad. 2015. Building the Neuronal Microtubule Cytoskeleton. *Neuron*. 87:492–506. doi:10.1016/j.neuron.2015.05.046.

Keating, T.J., J.G. Peloquin, V.I. Rodionov, D. Momcilovic, and G.G. Borisy. 1997. Microtubule release from the centrosome. *Proc. Natl. Acad. Sci. U. S. A.* 94:5078–5083. doi:10.1073/pnas.94.10.5078.

Kielkopf, C.L., W. Bauer, and I.L. Urbatsch. 2020. Bradford assay for determining protein concentration. *Cold Spring Harb. Protoc.* 2020:136–138. doi:10.1101/pdb.prot102269.

King, M.R., and S. Petry. 2020. Phase separation of TPX2 enhances and spatially coordinates microtubule nucleation. *Nat. Commun.* 11. doi:10.1038/s41467-019-14087-0.

Kleylein-Sohn, J., B. Pöllinger, M. Ohmer, F. Hofmann, E.A. Nigg, B.A. Hemmings, and M. Wartmann. 2012. Acentrosomal spindle organization renders cancer cells dependent on the kinesin HSET. *J. Cell Sci.* 125:5391–5402. doi:10.1242/jcs.107474.

Kollman, J.M., A. Merdes, L. Mourey, and D.A. Agard. 2011. Microtubule nucleation by γ-tubulin complexes. *Nat. Rev. Mol. Cell Biol.* 12:709–721. doi:10.1038/nrm3209.

Kollman, J.M., J.K. Polka, A. Zelter, T.N. Davis, and D.A. Agard. 2010. Microtubule nucleating γ 3-TuSC assembles structures with 13-fold microtubule-like symmetry. *Nature*. 466:879–882. doi:10.1038/nature09207.

Korten, T., S. Chaudhuri, E. Tavkin, M. Braun, and S. Diez. 2016. Kinesin-1 Expressed in Insect Cells Improves Microtubule in Vitro Gliding Performance, Long-Term Stability and Guiding Efficiency in Nanostructures. *IEEE Trans. Nanobioscience*. 15:62–69. doi:10.1109/TNB.2016.2520832.

Kostecka, L.G., A. Olseen, K.C. Kang, G. Torga, K.J. Pienta, and S.R. Amend. 2021. High KIFC1 expression is associated with poor prognosis in prostate cancer. *Med. Oncol.* 38. doi:10.1007/s12032-021-01494-x.

Kull, F.J., E.P. Sablin, R. Lau, R.J. Fletterick, and R.D. Vale. 1996. Crystal structure of the kinesin motor domain reveals a structural similarity to myosin. *Nature*. 380:550–555. doi:10.1038/380550a0.

Kurland, C., and J. Gallant. 1996. Errors of heterologous protein expression. *Curr. Opin. Biotechnol.* 7:489–493. doi:10.1016/S0958-1669(96)80050-4.

Kwok, B.H., and T.M. Kapoor. 2007. Microtubule flux: drivers wanted. *Curr. Opin. Cell Biol.* 19:36–42. doi:10.1016/j.ceb.2006.12.003.

Kwon, M., S.A. Godinho, N.S. Chandhok, N.J. Ganem, A. Azioune, M. Thery, and D. Pellman. 2008. Mechanisms to suppress multipolar divisions in cancer cells with extra centrosomes. *Genes Dev.* 22:2189–2203. doi:10.1101/gad.1700908.

Lai, T., and G. Garriga. 2004. The conserved kinase UNC-51 acts with VAB-8 and UNC-14 to regulate axon outgrowth in C. elegans. *Development*. 131:5991–6000. doi:10.1242/dev.01457.

Lawrence, E.J., G. Arpağ, S.R. Norris, and M. Zanic. 2018. Human CLASP2 specifically regulates microtubule catastrophe and rescue. *Mol. Biol. Cell*. mbc.E18-01-0016. doi:10.1091/mbc.e18-01-0016.

Li, J., H. Diao, X. Guan, and X. Tian. 2020. Kinesin family member C1 (KIFC1) regulated by centrosome protein e (CENPE) promotes proliferation, migration, and epithelial-mesenchymal transition of ovarian cancer. *Med. Sci. Monit.* 27. doi:10.12659/MSM.927869.

Liu, Y., P. Zhan, Z. Zhou, Z. Xing, S. Zhu, C. Ma, Q. Li, Q. Zhu, Y. Miao, J. Zhang, T. Lv, and Y. Song. 2016. The overexpression of KIFC1 was associated with the proliferation and prognosis of non-small cell lung cancer. *J. Thorac. Dis.* 8:2911–2923. doi:10.21037/jtd.2016.10.67.

Magiera, M.M., and C. Janke. 2014. Post-translational modifications of tubulin. *Curr. Biol.* 24. doi:10.1016/j.cub.2014.03.032.

Mandelkow, E.M., E. Mandelkow, and R.A. Milligan. 1991. Microtubule dynamics and microtubule caps: A time-resolved cryo-electron microscopy study. *J. Cell Biol.* 114:977–991. doi:10.1083/jcb.114.5.977.

Mandelkow, E.M., R. Schultheiss, R. Rapp, and M. Müller. 1986. On the surface lattice of microtubules: Helix starts, protofilament number, seam, and handedness. *J. Cell Biol.* 102:1067–1073. doi:10.1083/jcb.102.3.1067.

Mann, B.J., and P. Wadsworth. 2019. Kinesin-5 Regulation and Function in Mitosis. *Trends Cell Biol.* 29. doi:10.1016/j.tcb.2018.08.004.

Martin, M., and A. Akhmanova. 2018. Coming into Focus: Mechanisms of Microtubule Minus-End Organization. *Trends Cell Biol.* 28:574–588. doi:10.1016/j.tcb.2018.02.011.

Martin, M., A. Veloso, J. Wu, E.A. Katrukha, and A. Akhmanova. 2018. Control of endothelial cell polarity and sprouting angiogenesis by noncentrosomal microtubules. *Elife*. 7. doi:10.7554/eLife.33864.

Maurer, S.P., N.I. Cade, G. Bohner, N. Gustafsson, E. Boutant, and T. Surrey. 2014. EB1 accelerates two conformational transitions important for microtubule maturation and dynamics. *Curr. Biol.* 24:372–384. doi:10.1016/j.cub.2013.12.042.

Maurer, S.P., F.J. Fourniol, G. Bohner, C.A. Moores, and T. Surrey. 2012. EBs recognize a nucleotide-dependent structural cap at growing microtubule ends. *Cell*. 149:371–382. doi:10.1016/j.cell.2012.02.049.

McNally, F.J., and R.D. Vale. 1993. Identification of katanin, an ATPase that severs and disassembles stable microtubules. *Cell*. 75:419–429. doi:10.1016/0092-8674(93)90377-3.

Meiring, J.C.M., B.I. Shneyer, and A. Akhmanova. 2020. Generation and regulation of microtubule network asymmetry to drive cell polarity. *Curr. Opin. Cell Biol.* 62:86–95. doi:10.1016/J.CEB.2019.10.004.

Miki, H., Y. Okada, and N. Hirokawa. 2005. Analysis of the kinesin superfamily: insights into structure and function. *Trends Cell Biol.* 15:467–76. doi:10.1016/j.tcb.2005.07.006.

Miki, H., M. Setou, K. Kaneshiro, and N. Hirokawa. 2001. All kinesin superfamily protein, KIF, genes in mouse and human. *Proc. Natl. Acad. Sci. U. S. A.* 98:7004–11. doi:10.1073/pnas.111145398.

Mitchison, T., and M. Kirschner. 1984. Dynamic instability of microtubule growth. *Nature*. 312:237–242. doi:10.1038/312237a0.

Molodtsov, M.I., E.A. Ermakova, E.E. Shnol, E.L. Grishchuk, J.R. McIntosh, and F.I. Ataullakhanov. 2005. A molecular-mechanical model of the microtubule. *Biophys. J.*

88:3167–3179. doi:10.1529/biophysj.104.051789.

Monroy, B.Y., T.C. Tan, J.M. Oclaman, J.S. Han, S. Simó, S. Niwa, D.W. Nowakowski, R.J. McKenney, and K.M. Ori-McKenney. 2020. A Combinatorial MAP Code Dictates Polarized Microtubule Transport. *Dev. Cell*. 53:60-72.e4. doi:10.1016/j.devcel.2020.01.029.

Montenegro Gouveia, S., K. Leslie, L.C. Kapitein, R.M. Buey, I. Grigoriev, M. Wagenbach, I. Smal, E. Meijering, C.C. Hoogenraad, L. Wordeman, M.O. Steinmetz, and A. Akhmanova. 2010. In Vitro Reconstitution of the Functional Interplay between MCAK and EB3 at Microtubule Plus Ends. *Curr. Biol.* 20:1717–1722. doi:10.1016/J.CUB.2010.08.020.

Moores, C.A., M. Yu, J. Guo, C. Beraud, R. Sakowicz, and R.A. Milligan. 2002. A mechanism for microtubule depolymerization by KinI kinesins. *Mol. Cell*. 9:903–909. doi:10.1016/S1097-2765(02)00503-8.

Moritz, M., M.B. Braunfeld, V. Guénebaut, J. Heuser, and D.A. Agard. 2000. Structure of the γ-tubulin ring complex: A template for microtubule nucleation. *Nat. Cell Biol.* 2:365–370. doi:10.1038/35014058.

Moritz, M., M.B. Braunfeld, J.W. Sedat, B. Alberts, and D.A. Agard. 1995. Microtubule nucleation by γ-tubulin-containing rings in the centrosome. *Nature*. 378:638–640. doi:10.1038/378638a0.

Mountain, V., C. Simerly, L. Howard, A. Ando, G. Schatten, and D.A. Compton. 1999. The kinesin-related protein, HSET, opposes the activity of Eg5 and cross-links microtubules in the mammalian mitotic spindle. *J. Cell Biol.* 147:351–365. doi:10.1083/jcb.147.2.351.

Mukherjee, S., J.D. Diaz Valencia, S. Stewman, J. Metz, S. Monnier, U. Rath, A.B. Asenjo, R.A. Charafeddine, H.J. Sosa, J.L. Ross, A. Ma, and D.J. Sharp. 2012. Human fidgetin is a microtubule severing enzyme and minus-end depolymerase that regulates mitosis. *Cell*

Cycle. 11:2359–2366. doi:10.4161/cc.20849.

Muralidharan, H., and P.W. Baas. 2019. Mitotic Motor KIFC1 Is an Organizer of Microtubules in the Axon. *J. Neurosci.* 39:3792–3811. doi:10.1523/JNEUROSCI.3099-18.2019.

Myers, S.M., and I. Collins. 2016. Recent findings and future directions for interpolar mitotic kinesin inhibitors in cancer therapy. *Future Med. Chem.* 8:463–89. doi:10.4155/fmc.16.5.

Nakamura, M., D.W. Ehrhardt, and T. Hashimoto. 2010. Microtubule and katanin-dependent dynamics of microtubule nucleation complexes in the acentrosomal Arabidopsis cortical array. *Nat. Cell Biol.* 12:1064–1070. doi:10.1038/ncb2110.

Nawrotek, A., M. Knossow, and B. Gigant. 2011. The determinants that Govern microtubule assembly from the atomic structure of GTP-tubulin. *J. Mol. Biol.* 412:35–42. doi:10.1016/j.jmb.2011.07.029.

Newton, C.N., M. Wagenbach, Y. Ovechkina, L. Wordeman, and L. Wilson. 2004. MCAK, a Kin I kinesin, increases the catastrophe frequency of steady-state HeLa cell microtubules in an ATP-dependent manner in vitro. *FEBS Lett.* 572:80–84. doi:10.1016/j.febslet.2004.06.093.

Niwa, S. 2015. Kinesin superfamily proteins and the regulation of microtubule dynamics in morphogenesis. *Anat. Sci. Int.* 90:1–6. doi:10.1007/s12565-014-0259-5.

Nogales, E., M. Whittaker, R.A. Milligan, and K.H. Downing. 1999. High-resolution model of the microtubule. *Cell*. 96:79–88.

Nogales, E., S.G. Wolf, and K.H. Downing. 1998. Structure of the alpha beta tubulin dimer by electron crystallography. *Nature*. 391:199–203. doi:10.1038/34465.

Noordstra, I., Q. Liu, W. Nijenhuis, S. Hua, K. Jiang, M. Baars, S. Remmelzwaal, M. Martin, L.C. Kapitein, and A. Akhmanova. 2016. Control of apico–basal epithelial polarity by the

microtubule minus-end-binding protein CAMSAP3 and spectraplakin ACF7. *J. Cell Sci.* 129:4278–4288. doi:10.1242/jcs.194878.

Norris, S.R., S. Jung, P. Singh, C.E. Strothman, A.L. Erwin, M.D. Ohi, M. Zanic, and R. Ohi. 2018. Microtubule minus-end aster organization is driven by processive HSET-tubulin clusters. *Nat. Commun.* 9:2659. doi:10.1038/s41467-018-04991-2.

O'Brien, E.T., E.D. Salmon, R.A. Walker, and H.P. Erickson. 1990. Effects of magnesium on the dynamic instability of individual microtubules. *Biochemistry*. 29:6648–56.

O'Toole, E.T., K.L. McDonald, J. Mäntler, J.R. McIntosh, A.A. Hyman, and T. Müdler-Reichert. 2003. Morphologically distinct microtubule ends in the mitotic centrosome of Caenorhabditis elegans. *J. Cell Biol.* 163:451–456. doi:10.1083/jcb.200304035.

Odde, D.J., L. Cassimeris, and H.M. Buettner. 1995. Kinetics of microtubule catastrophe assessed by probabilistic analysis. *Biophys. J.* 69:796–802. doi:10.1016/S0006-3495(95)79953-2.

Odde, D.J., L. Ma, A.H. Briggs, A. DeMarco, and M.W. Kirschner. 1999. Microtubule bending and breaking in living fibroblast cells. *J. Cell Sci.* 112:3283–3288.

Ohi, R., K. Burbank, Q. Liu, and T.J. Mitchison. 2007. Nonredundant Functions of Kinesin-13s during Meiotic Spindle Assembly. *Curr. Biol.* 17:953–959. doi:10.1016/j.cub.2007.04.057.

Ohi, R., C. Strothman, and M. Zanic. 2021. Impact of the 'tubulin economy' on the formation and function of the microtubule cytoskeleton. *Curr. Opin. Cell Biol.* 68:81–89. doi:10.1016/j.ceb.2020.09.005.

Oosawa, F. 1970. Size distribution of protein polymers. *J. Theor. Biol.* 27:69–86. doi:10.1016/0022-5193(70)90129-3.

Pannu, V., P.C.G. Rida, A. Ogden, R.C. Turaga, S. Donthamsetty, N.J. Bowen, K. Rudd, M. V.

Gupta, M.D. Reid, G. Cantuaria, C.E. Walczak, and R. Aneja. 2015. HSET overexpression fuels tumor progression via centrosome clustering-independent mechanisms in breast cancer patients. *Oncotarget*. 6:6076–91. doi:10.18632/oncotarget.3475.

Parvin, A., S.L. Hao, F.Q. Tan, and W.X. Yang. 2020. Inhibition of kinesin motor protein KIFC1 by AZ82 induces multipolar mitosis and apoptosis in prostate cancer cell. *Gene*. 760. doi:10.1016/j.gene.2020.144989.

Patel, J.T., H.R. Belsham, A.J. Rathbone, B. Wickstead, C. Gell, and C.T. Friel. 2016. The family-specific α4-helix of the kinesin-13, MCAK, is critical to microtubule end recognition. *Open Biol.* 6:160223. doi:10.1098/rsob.160223.

Petry, S., and R.D. Vale. 2015. Microtubule nucleation at the centrosome and beyond. *Nat. Cell Biol.* 17:1089–1093. doi:10.1038/ncb3220.

Ravelli, R.B.G., B. Gigant, P.A. Curmi, I. Jourdain, S. Lachkar, A. Sobel, and M. Knossow. 2004. Insight into tubulin regulation from a complex with colchicine and a stathmin-like domain. *Nature*. 428:198–202. doi:10.1038/nature02393.

Redemann, S., J. Baumgart, N. Lindow, M. Shelley, E. Nazockdast, A. Kratz, S. Prohaska, J. Brugués, S. Fürthauer, and T. Müller-Reichert. 2017. C. elegans chromosomes connect to centrosomes by anchoring into the spindle network. *Nat. Commun.* 8:15288. doi:10.1038/ncomms15288.

Reid, T.A., C. Coombes, S. Mukherjee, R.R. Goldblum, K. White, S. Parmar, M. McClellan, M. Zanic, N. Courtemanche, and M.K. Gardner. 2019. Structural state recognition facilitates tip tracking of EB1 at growing microtubule ends. *Elife*. 8. doi:10.7554/eLife.48117.

Reinemann, D.N., S.R. Norris, R. Ohi, and M.J. Lang. 2018. Processive Kinesin-14 HSET Exhibits Directional Flexibility Depending on Motor Traffic. *Curr. Biol.* 28:2356-2362.e5.

doi:10.1016/j.cub.2018.06.055.

Rice, L.M., E.A. Montabana, and D.A. Agard. 2008. The lattice as allosteric effector: Structural studies of αβ- and γ-tubulin clarify the role of GTP in microtubule assembly. *Proc. Natl. Acad. Sci. U. S. A.* 105:5378–5383. doi:10.1073/pnas.0801155105.

Rickman, J., C. Duellberg, N.I. Cade, L.D. Griffin, and T. Surrey. 2017. Steady-state EB cap size fluctuations are determined by stochastic microtubule growth and maturation. *Proc. Natl. Acad. Sci.* 114:3427–3432. doi:10.1073/pnas.1620274114.

Rios, R.M. 2014. The centrosome-Golgi apparatus nexus. *Philos. Trans. R. Soc. B Biol. Sci.* 369:20130462–20130462. doi:10.1098/rstb.2013.0462.

Rodionov, V., E. Nadezhdina, G. Borisy, and L.G. Tilney. 1999. Centrosomal control of microtubule dynamics. *Cell Biol.* 96:115–120.

Rogers, G.C., S.L. Rogers, and D.J. Sharp. 2005. Spindle microtubules in flux. *J. Cell Sci.* 118:1105–1116. doi:10.1242/jcs.02284.

Roostalu, J., C. Thomas, N.I. Cade, S. Kunzelmann, I.A. Taylor, and T. Surrey. 2020. The speed of GTP hydrolysis determines GTP cap size and controls microtubule stability. *Elife*. 9:1–22. doi:10.7554/eLife.51992.

Sablin, E.P., R.B. Case, S.C. Dai, C.L. Hart, A. Ruby, R.D. Vale, and R.J. Fletterick. 1998. Direction determination in the minus-end-directed kinesin motor ncd. *Nature*. 395:813–816. doi:10.1038/27463.

Schaedel, L., K. John, J. Gaillard, M. V. Nachury, L. Blanchoin, and M. Théry. 2015. Microtubules self-repair in response to mechanical stress. *Nat. Mater.* 14:1156–1163. doi:10.1038/nmat4396.

Schindelin, J., I. Arganda-Carreras, E. Frise, V. Kaynig, M. Longair, T. Pietzsch, S. Preibisch, C.

Rueden, S. Saalfeld, B. Schmid, J.-Y. Tinevez, D.J. White, V. Hartenstein, K. Eliceiri, P. Tomancak, and A. Cardona. 2012. Fiji: an open-source platform for biological-image analysis. *Nat. Methods*. 9:676.

Schmidt, F.R. 2004. Recombinant expression systems in the pharmaceutical industry. *Appl. Microbiol. Biotechnol.* 65:363–372. doi:10.1007/s00253-004-1656-9.

Seetapun, D., B.T. Castle, A.J. McIntyre, P.T. Tran, and D.J. Odde. 2012. Estimating the microtubule GTP cap size in vivo. *Curr. Biol.* 22:1681–1687. doi:10.1016/j.cub.2012.06.068.

Sekino, Y., N. Oue, Y. Koike, Y. Shigematsu, N. Sakamoto, K. Sentani, J. Teishima, M. Shiota, A. Matsubara, and W. Yasui. 2019. KIFC1 Inhibitor CW069 Induces Apoptosis and Reverses Resistance to Docetaxel in Prostate Cancer. *J. Clin. Med.* 8:225. doi:10.3390/jcm8020225.

She, Z.-Y., and W.-X. Yang. 2017. Molecular mechanisms of kinesin-14 motors in spindle assembly and chromosome segregation. *J. Cell Sci.* 130:2097–2110. doi:10.1242/jcs.200261.

Siahaan, V., J. Krattenmacher, A.A. Hyman, S. Diez, A. Hernández-Vega, Z. Lansky, and M. Braun. 2019. Kinetically distinct phases of tau on microtubules regulate kinesin motors and severing enzymes. *Nat. Cell Biol.* 21:1086–1092. doi:10.1038/s41556-019-0374-6.

Siddiqui, S.S. 2002. Metazoan motor models: kinesin superfamily in C. elegans. *Traffic*. 3:20–8.

Sisson, J.C., K.S. Ho, K. Suyama, and M.P. Scott. 1997. Costal2, a Novel Kinesin-Related Protein in the Hedgehog Signaling Pathway. *Cell*. 90:235–245. doi:10.1016/S0092-8674(00)80332-3.

Song, Y., and S.T. Brady. 2015. Post-translational modifications of tubulin: Pathways to

functional diversity of microtubules. *Trends Cell Biol.* 25. doi:10.1016/j.tcb.2014.10.004.

Sproul, L.R., D.J. Anderson, A.T. Mackey, W.S. Saunders, and S.P. Gilbert. 2005. Cik1 targets the minus-end Kinesin depolymerase Kar3 to microtubule plus ends. *Curr. Biol.* 15:1420–1427. doi:10.1016/j.cub.2005.06.066.

Strothman, C., V. Farmer, G. Arpağ, N. Rodgers, M. Podolski, S. Norris, R. Ohi, and M. Zanic. 2019. Microtubule minus-end stability is dictated by the tubulin off-rate. *J. Cell Biol.* 218:2841–2853. doi:10.1083/jcb.201905019.

Tan, R., A.J. Lam, T. Tan, J. Han, D.W. Nowakowski, M. Vershinin, S. Simó, K.M. Ori-McKenney, and R.J. McKenney. 2019. Microtubules gate tau condensation to spatially regulate microtubule functions. *Nat. Cell Biol.* 21:1078–1085. doi:10.1038/s41556-019-0375-5.

Tanaka, N., W. Meng, S. Nagae, and M. Takeichi. 2012. Nezha/CAMSAP3 and CAMSAP2 cooperate in epithelial-specific organization of noncentrosomal microtubules. *Proc. Natl. Acad. Sci.* 109:20029–20034. doi:10.1073/pnas.1218017109.

Tao, J., C. Feng, and M.M. Rolls. 2016. The microtubule-severing protein fidgetin acts after dendrite injury to promote their degeneration. *J. Cell Sci.* 129:3274–3281. doi:10.1242/jcs.188540.

Thawani, A., M.J. Rale, N. Coudray, G. Bhabha, H.A. Stone, J.W. Shaevitz, and S. Petry. 2020. The transition state and regulation of γ-TuRC-mediated microtubule nucleation revealed by single molecule microscopy. *Elife*. 9:1–34. doi:10.7554/eLife.54253.

Ti, S.C., M.C. Pamula, S.C. Howes, C. Duellberg, N.I. Cade, R.E. Kleiner, S. Forth, T. Surrey, E. Nogales, and T.M. Kapoor. 2016. Mutations in Human Tubulin Proximal to the Kinesin-Binding Site Alter Dynamic Instability at Microtubule Plus- and Minus-Ends. *Dev. Cell*.

37:72–84. doi:10.1016/j.devcel.2016.03.003.

Toya, M., S. Kobayashi, M. Kawasaki, G. Shioi, M. Kaneko, T. Ishiuchi, K. Misaki, W. Meng, and M. Takeichi. 2016. CAMSAP3 orients the apical-to-basal polarity of microtubule arrays in epithelial cells. *Proc. Natl. Acad. Sci. U. S. A.* 113:332–337. doi:10.1073/pnas.1520638113.

Tran, P.T., R.A. Walker, and E.D. Salmon. 1997. A Metastable Intermediate State of Microtubule Dynamic Instability That Differs Significantly between Plus and Minus Ends. *J. Cell Biol.* 138:105.

Trinczek, B., A. Marx, E.M. Mandelkow, D.B. Murphy, and E. Mandelkow. 1993. Dynamics of microtubules from erythrocyte marginal bands. *Mol. Biol. Cell*. 4:323–335. doi:10.1091/mbc.4.3.323.

Tropini, C., E.A. Roth, M. Zanic, M.K. Gardner, and J. Howard. 2012. Islands containing slowly hydrolyzable GTP analogs promote microtubule rescues. *PLoS One*. 7. doi:10.1371/journal.pone.0030103.

Vemu, A., E. Szczesna, E.A. Zehr, J.O. Spector, N. Grigorieff, A.M. Deaconescu, and A. Roll-Mecak. 2018. Severing enzymes amplify microtubule arrays through lattice GTP-tubulin incorporation. *Science (80-.).* 361:eaau1504. doi:10.1126/science.aau1504.

Vorobjev, I. a, V.I. Rodionov, I. V Maly, and G.G. Borisy. 1999. Contribution of plus and minus end pathways to microtubule turnover. *J. Cell Sci.* 112 (Pt 1:2277–2289.

Vorobjev, I.A., T.M. Svitkina, and G.G. Borisy. 1997. Cytoplasmic assembly of microtubules in cultured cells. *J. Cell Sci.* 110:2635–2645.

Voter, W.A., E.T. O'Brien, and H.P. Erickson. 1991. Dilution-induced disassembly of microtubules: Relation to dynamic instability and the GTP cap. *Cell Motil. Cytoskeleton*.

18:55–62. doi:10.1002/cm.970180106.

Walczak, C.E., T.J. Mitchison, and A. Desai. 1996. XKCM1: A Xenopus kinesin-related protein that regulates microtubule dynamics during mitotic spindle assembly. *Cell*. 84:37–47. doi:10.1016/S0092-8674(00)80991-5.

Walker, R.A. 1988. Dynamic instability of individual microtubules analyzed by video light microscopy: rate constants and transition frequencies. *J. Cell Biol.* 107:1437–1448. doi:10.1083/jcb.107.4.1437.

Walker, R.A., S. Inoue, and E.D. Salmon. 1989. Asymmetric behavior of severed microtubule ends after ultraviolet-microbeam irradiation of individual microtubules in vitro. *J. Cell Biol.* 108:931–937. doi:10.1083/jcb.108.3.931.

Walker, R.A., E.T. O'Brien, N.K. Pryer, M.F. Soboeiro, W.A. Voter, H.P. Erickson, and E.D. Salmon. 1988. Dynamic instability of individual microtubules analyzed by video light microscopy: rate constants and transition frequencies. *J. Cell Biol.* 107:1437–1448. doi:10.1083/jcb.107.4.1437.

Walker, R.A., N.K. Pryer, and E.D. Salmon. 1991. Dilution of individual microtubules observed in real time in vitro: Evidence that cap size is small and independent of elongation rate. *J. Cell Biol.* 114:73–81. doi:10.1083/jcb.114.1.73.

Wasilko, D., and S.E. Lee. 2006. TIPS: Titerless Infected-Cells Preservation and Scale-Up. *Bioprocess. J.* 5:29–32. doi:10.12665/j53.wasilkolee.

Wasilko, D.J., S. Edward Lee, K.J. Stutzman-Engwall, B.A. Reitz, T.L. Emmons, K.J. Mathis, M.J. Bienkowski, A.G. Tomasselli, and H. David Fischer. 2009. The titerless infected-cells preservation and scale-up (TIPS) method for large-scale production of NO-sensitive human soluble guanylate cyclase (sGC) from insect cells infected with recombinant baculovirus.

Protein Expr. Purif. 65:122–132. doi:10.1016/j.pep.2009.01.002.

Waterman-Storer, C.M., and E.D. Salmon. 1997. Actomyosin-based retrograde flow of microtubules in the lamella of migrating epithelial cells influences microtubule dynamic instability and turnover and is associated with microtubule breakage and treadmilling. *J. Cell Biol.* 139:417–434. doi:10.1083/jcb.139.2.417.

Weaver, L.N., S.C. Ems-McClung, S.-H.R. Chen, G. Yang, S.L. Shaw, and C.E. Walczak. 2015. The Ran-GTP gradient spatially regulates XCTK2 in the spindle. *Curr. Biol.* 25:1509–14. doi:10.1016/j.cub.2015.04.015.

Weisenberg, R.C., G.G. Borisy, and E.W. Taylor. 1968. The Colchicine-Binding Protein of Mammalian Brain and Its Relation to Microtubules. *Biochemistry*. 7:4466–4479. doi:10.1021/bi00852a043.

Wiese, C., and Y. Zheng. 2000. A new function for the γ-tubulin ring complex as a microtubule minus-end cap. *Nat. Cell Biol.* 2:358–364. doi:10.1038/35014051.

Wolf, F.W., M.-S. Hung, B. Wightman, J. Way, and G. Garriga. 1998. vab-8 Is a Key Regulator of Posteriorly Directed Migrations in C. elegans and Encodes a Novel Protein with Kinesin Motor Similarity. *Neuron*. 20:655–666. doi:10.1016/S0896-6273(00)81006-5.

Wordeman, L. 2010. How kinesin motor proteins drive mitotic spindle function: Lessons from molecular assays. *Semin. Cell Dev. Biol.* 21:260–268. doi:10.1016/j.semcdb.2010.01.018.

Wordeman, L., and T.J. Mitchison. 1995. Identification and partial characterization of mitotic centromere- associated kinesin, a kinesin-related protein that associates with centromeres during mitosis. *J. Cell Biol.* 128:95–105. doi:10.1083/jcb.128.1.95.

Wu, J., K. Mikule, W. Wang, N. Su, P. Petteruti, F. Gharahdaghi, E. Code, X. Zhu, K. Jacques, Z. Lai, B. Yang, M.L. Lamb, C. Chuaqui, N. Keen, and H. Chen. 2013. Discovery and

mechanistic study of a small molecule inhibitor for motor protein KIFC1. *ACS Chem. Biol.* 8:2201–2208. doi:10.1021/cb400186w.

Xiao, Y.-X., and W.-X. Yang. 2016. KIFC1: a promising chemotherapy target for cancer treatment? *Oncotarget*. 7:48656–48670. doi:10.18632/oncotarget.8799.

Yau, K.W., S.F.B. vanBeuningen, I. Cunha-Ferreira, B.M.C. Cloin, E.Y. vanBattum, L. Will, P. Schätzle, R.P. Tas, J. vanKrugten, E.A. Katrukha, K. Jiang, P.S. Wulf, M. Mikhaylova, M. Harterink, R.J. Pasterkamp, A. Akhmanova, L.C. Kapitein, and C.C. Hoogenraad. 2014. Microtubule minus-end binding protein CAMSAP2 controls axon specification and dendrite development. *Neuron*. 82:1058–1073. doi:10.1016/j.neuron.2014.04.019.

Yukawa, M., T. Yamauchi, N. Kurisawa, S. Ahmed, K. ichi Kimura, and T. Toda. 2018. Fission yeast cells overproducing HSET/KIFC1 provides a useful tool for identification and evaluation of human kinesin-14 inhibitors. *Fungal Genet. Biol.* 116:33–41. doi:10.1016/j.fgb.2018.04.006.

Yvon, A.M., and P. Wadsworth. 1997. Non-centrosomal microtubule formation and measurement of minus end microtubule dynamics in A498 cells. *J. Cell Sci.* 110 (Pt 1:2391–401.

Zanic, M. 2016. Measuring the effects of microtubule-associated proteins on microtubule dynamics in vitro. *Methods Mol. Biol.* 1413:47–61. doi:10.1007/978-1-4939-3542-0_4.

Zanic, M., J.H. Stear, A.A. Hyman, and J. Howard. 2009. EB1 recognizes the nucleotide state of tubulin in the microtubule lattice. *PLoS One*. 4:e7585. doi:10.1371/journal.pone.0007585.

Zanic, M., P.O. Widlund, A.A. Hyman, and J. Howard. 2013. Synergy between XMAP215 and EB1 increases microtubule growth rates to physiological levels. *Nat. Cell Biol.* 15:688–693. doi:10.1038/ncb2744.

Zhang, D., G.C. Rogers, D.W. Buster, and D.J. Sharp. 2007. Three microtubule severing enzymes contribute to the “Pacman- flux” machinery that moves chromosomes. *J. Cell Biol.* 177:231–242. doi:10.1083/jcb.200612011.

Zhang, R., G.M. Alushin, A. Brown, and E. Nogales. 2015. Mechanistic Origin of Microtubule Dynamic Instability and Its Modulation by EB Proteins. *Cell*. 162:849–859. doi:10.1016/j.cell.2015.07.012.

Zhang, R., B. LaFrance, and E. Nogales. 2018. Separating the effects of nucleotide and EB binding on microtubule structure. *Proc. Natl. Acad. Sci.* 115:E6191–E6200. doi:10.1073/pnas.1802637115.

Zhang, R., J. Roostalu, T. Surrey, and E. Nogales. 2017. Structural insight into TPX2-stimulated microtubule assembly. *Elife*. 6. doi:10.7554/eLife.30959.

Zhou, K., J. Zhao, L. Qi, Y. He, J. Xu, and M. Dai. 2020. Kinesin Family Member C1 (KIFC1) Accelerates Proliferation and Invasion of Endometrial Cancer Cells Through Modulating the PI3K/AKT Signaling Pathway. *Technol. Cancer Res. Treat.* 19. doi:10.1177/1533033820964217.

Zhou, R., S. Niwa, N. Homma, Y. Takei, and N. Hirokawa. 2009. KIF26A Is an Unconventional Kinesin and Regulates GDNF-Ret Signaling in Enteric Neuronal Development. *Cell*. 139:802–813. doi:10.1016/j.cell.2009.10.023.

Zhu, X., and I. Kaverina. 2013. Golgi as an MTOC: Making microtubules for its own good. *Histochem. Cell Biol.* 140:361–367. doi:10.1007/s00418-013-1119-4.